EINDHOVEN UNIVERSITY OF TECHNOLOGY

Eindhoven University of Technology

MASTER

Theory and fabrication of SnTe for Majorana devices

Hoskam, Max S.M.

Award date:
2018

Link to publication

Disclaimer
This document contains a student thesis (bachelor's or master's), as authored by a student at Eindhoven University of Technology. Student theses are made available in the TU/e repository upon obtaining the required degree. The grade received is not published on the document as presented in the repository. The required complexity or quality of research of student theses may vary by program, and the required minimum study period may vary in duration.

General rights
Copyright and moral rights for the publications made accessible in the public portal are retained by the authors and/or other copyright owners and it is a condition of accessing publications that users recognise and abide by the legal requirements associated with these rights.

• Users may download and print one copy of any publication from the public portal for the purpose of private study or research.
• You may not further distribute the material or use it for any profit-making activity or commercial gain

Theory and Fabrication of SnTe for Majorana devices

by

M.S.M. (Max) Hoskam (0841546)
Department of Applied Physics
Eindhoven University of Technology

In collaboration with
Delft University of Technology

Final presentation: August 28 2018, 15:00, Cascade 2.10
Supervisors: E.P.A.M. Bakkers, P. Leubner, R. Op het Veld, M. Wimmer, D. Varjas.

Abstract

Tin telluride (SnTe) is a topological crystalline insulator with gapless surface states protected by mirror symmetry. In this work the potential of SnTe for application in Majorana devices is investigated, which is approached from both a modelling and a materials science perspective. 2D surface states and 1D edge states are reproduced using tight binding models. Besides that, in modelled nanowire energy dispersions indications of Dirac physics appear, but Dirac cones are buried in the bulk bands for practical nanowire diameters. Moreover, modelling of superconducting SnTe thin films shows 2 and 4 Majorana fermions at each end of a superconducting π-junction for the $[111]$ and $[001]$ surface facets respectively.

For the first time ever SnTe nanowires are grown in MBE, at low temperatures and low fluxes. They can be grown so that no traces of Au are detected in EDX. Sizes vary with lengths of $300\ \mathrm{nm} - 5\ \mu\mathrm{m}$ and diameters of $15 - 100\ \mathrm{nm}$. Nanowires with $\{110\}$ and $\{112\}$ growth directions are found. The nanowire surface facets are oxidized, which could perturb the topological crystalline insulator surface states on its surface.

Contents

Abstract 2

Contents 3

1. Introduction 5

2. Theory 9

2.1 Topological (crystalline) insulators: SnTe 9

2.2 Comparison of different devices to create Majorana fermions 12

2.2.1 Superconductor-semiconductor hybrid nanowires 12

2.2.2 Topological insulator Majorana wires 15

2.2.3 Superconducting quantum spin Hall insulators 17

2.3. Molecular beam epitaxy of SnTe and $Pb_{1-x}Sn_xTe$ 18

2.3.1 General introduction to molecular beam epitaxy 18

2.3.2 Substrates and $Pb_{1-x}Sn_xTe$ film growth 19

2.3.3 Nanowire growth and material aspects of SnTe 23

2.3.4 The p-doping problem of SnTe and consequences 25

2.3.5 SnTe nanowire growth by other growth methods 27

3. Methods 31

3.1 Tight-binding approach 31

3.2 Molecular beam epitaxy setup and sample preparation 35

3.2.1 Practical considerations 35

3.2.2 Substrate processing 35

3.2.3 UHV Pumping 39

3.2.4 BandiT temperature measurements 40

3.2.5 Effusion flux calibration and substrate temperature 42

4. Results and discussion 46

4.1 Normal state SnTe tight binding simulations 46

4.1.1 Surface state dispersion 46

4.1.2 Demonstration of edge states in thin films 51

4.1.3 Simulating non-superconducting SnTe Nanowires 57

4.1.4 Modelling the Magnetic fields in SnTe 59

4.2 Modelling SnTe Majorana devices 61

4.2.1 Modelling superconductivity 61

4.2.2 Majorana fermions in SnTe nanowires 62

4.2.3 SnTe thin film superconducting junctions 63
4.3. SnTe nanowire growth results 69
4.3.1 High temperature growth 69
4.3.2 Low temperature Au-catalyzed SnTe nanowires 71
4.3.3 Growth time series.. 76
4.3.4 Sn and Te flux series.. 77
4.3.5 Thermal annealing and positive T-gradients.. 82
4.3.6 Substrate processing.. 83
5. Conclusion and outlook 85
6. Appendix 87
6.1 Surface density of states method 87
6.2 Derivation of Angular momentum matrices 89
6.3 Python code 93

1. Introduction

A quantum computer uses quantum-mechanical phenomena like superposition and entanglement to do computations. In contrast to a classical computer, which uses classical bits that can represent either the values 0 or 1, the basic unit of a quantum computer is a quantum mechanical two-level system (qubit) that can exist in superpositions of the values 0 and 1. This means that a set of n qubits can be in a superposition of up to 2^n different states, each representing a binary number. The qubit system is controlled and manipulated by applying unitary transformations to the system, which affect all states of the superposition simultaneously. Quantum gates form the basic units from which these unitary transformations are built up[1].

Following Moore's law[2], integrated chips are getting denser and denser, as the number of transistors on a chip doubles about every two years. At the same time, transistors are getting smaller and smaller, as Intel's processors scheduled for 2019 will have feature sizes below 10 nm[3], corresponding to about the combined size of 40 silicon atoms on a row. At these length scales quantum phenomena, such as quantum tunneling, can no longer be ignored. As opposed to classical computing, where quantum behaviour is unwanted, quantum computers use these quantum mechanical effects to enable complex computations.
Quantum computers have major advantages over classical computers. First of all, due to their high degree of parallelism, a number of problems which cannot feasibly be tackled on a classical computer can be solved efficiently on a quantum computer. An example is Shor's quantum algorithm[4], that allows the factorization of a number with an exponential increase of speed.

Besides that, quantum computers can be used to simulate physics in quantum simulators. Proposed by Richard Feynman, quantum simulators[5,6] use a simple control quantum system to simulate the behavior of a more complex quantum system, which is possible when their Hamiltonians are the same. Quantum simulation cannot be performed by classical computers, because they deal less efficiently with quantum-mechanical phenomena. Quantum simulators could for example eventually be used to simulate the dynamics of protein folding, which is valuable in the development of drugs.

Possible qubits proposed for quantum computing are photons, trapped atoms or ions and nuclear spins, however all of these qubits display the phenomenon of decoherence, which holds back the realization of quantum computers. Decoherence is the transformation, over time, of a quantum-mechanical superposition state into a classical statistical mixture as a result of the quantum system interacting with the 'environment'[1]. In this process the system loses its quantum mechanical behavior. The coherent or pure state and non-coherent or mixture state have different density operators. The former has 'off-diagonal' or 'coherence' terms, while for the mixture state these terms are absent. An example of decoherence can be found in Rabi oscillations, where a two-level system, such as a Rydberg atom, inside a cavity oscillates between a ground state g and an excited state e with frequency Ω. The Rabi oscillation, a quantum-mechanical phenomenon, is damped because of interaction with the environment. Fig. 1.1 shows a measurement of a Rabi oscillation[7] of a Rydberg atom in a microwave cavity undergoing decoherence.

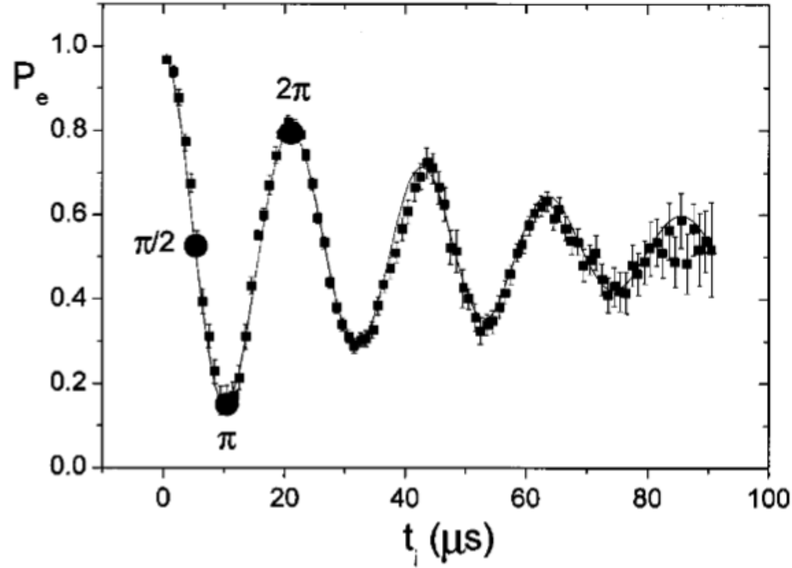

Fig. 1.1: Vacuum Rabi oscillations. The atom in state e enters an empty resonant cavity. P_E denotes the probability for detecting the atom in state e as a function of the effective interaction time t_i. The period of the oscillation is $1/2\Omega$, while the exponential decay is proportional to the decoherence time τ_φ[7].

The problem of decoherence can be tackled by quantum error correction (QEC). For example non-destructive measurements can be performed on the qubits. Hereby errors can be detected before they accumulate and corrections can be made to the system within the coherence time[8,5]. However there are also proposals for qubits that are intrinsically free of decoherence and do not need quantum error correction. These qubits are called topological qubits, which could be realized by certain quasiparticles called Majorana fermions.

The topological qubit or Majorana quasiparticle[8], which is investigated in this research, does not interact with its environment; it is topologically protected against decoherence[9]. Unlike electrons, Majorana quasiparticles are their own antiparticle and they always come in pairs. A consequence of the former property of Majorana quasiparticles is that these particles have no observable energy, charge or spin. Also they only appear in exotic materials called topological superconductors.

Quantum computing with Majorana quasiparticles or zero modes is done by braiding. The position of Majorana zero modes is exchanged which corresponds to a nontrivial transformation within the degenerate ground-state manifold, and represents a non-commutative operation which does not depend on the way and the details of its execution[10]. Because of the properties of braiding it is topologically protected, therefore minimizing decoherence and errors.

From a materials point of view the topological qubit could be realized by semiconductor/superconductor hybrid nanowire, often made from a (heavy-element and high spin-orbit) InSb nanowire on which superconducting aluminum is evaporated at some of the surface facets. The semiconductor/superconductor hybrid nanowire is brought into the topological phase by applying specific magnetic and electric fields, so that Majorana fermions are generated. This research looks into a different materials system called tin telluride (SnTe) which does not generate

Majoranas by itself, but due to its different topological properties then trivial heavy-element semiconductors could be a promising material for a topological qubit. In this research is investigated whether SnTe could be used in a similar way as InSb nanowires to generate Majorana fermions, but also whether it can be used in completely different ways such as in thin film geometries.

SnTe is a topological crystalline insulator (TCI) protected by the crystal's mirror symmetry. Its bulk is insulating, while gapless surface states exist on the surfaces that are mirror symmetric with respect to the $\{110\}$ plane. In contrast to a topological crystalline insulator, a topological insulator (TI) has gapless surface states that are protected by time-reversal symmetry. TCIs and TIs could have major advantages over these heavy-element semiconductors. Proposals for TI Majorana devices have already been reported using for example Bi_2Se_3 nanowires or HgTe thin films.

Both the theoretical aspects as the materials science aspects of the subject of SnTe Majorana devices are not yet heavily researched. Therefore this research will approach the subject from both the modelling as the materials science side. The theoretical side will focus on the modelling of SnTe dispersions in multiple geometries, with focus on thin films and nanowires, where the nanowire part is never reported in literature before. The modelling will be done using a tight binding model from literature. Additionally the normal state of SnTe also the superconducting state will be investigated which, in combination of interaction with magnetic field, is essential for Majorana devices. Finally topological invariants and conductance calculations will be treated shortly.
The experimental part of this research will focus on the growth of nanowires. This will be done using a MBE system which was not reported in literature up till now. Growing SnTe nanowires in MBE is promising in improving the quality of the SnTe nanowires by reducing their spontaneously emerging p-dopant levels due to growth at lower temperatures.

In this report the modelling and growth sections are not strictly separated, but the modelling part is central in the first sections of each Chapter, while for the last sections of each Chapter the growth parts are central. The report is built up so that in Chapter 2 the theory of topological (crystalline) insulators, Majorana devices and molecular beam epitaxy of SnTe are discussed. In Chapter 3 the experimental methods are discussed, starting with the tight-binding approach and SnTe bulk dispersion calculations to gain confidence into the model. In section 3.2 all considerations relevant to the MBE setup and substrate processing are discussed. This includes discussions on the choice of effusion sources and the means of temperature monitoring during growth etc. In Chapter 4 the results of the tight binding simulations on SnTe are discussed, where section 4.1 focusses on the normal state and section 4.2 treats the superconducting state in which Majorana fermions emerge in certain geometries of the material. Finally in section 4.3 the growth results acquired after about 40 days of growth are reported. Here growth under different growth conditions is discussed such as different temperatures and material fluxes. This is supported by SEM and TEM microscopy studies.

References Chapter 1

1. C. Gerry, P. Knight, ‘Introductory Quantum Optics’, Cambridge U.P., (2005).

2. G. Moore, ‘Cramming more components onto integrated circuits’, *Proceedings of the IEEE,* 86, Issue 1, 82-85, (1998).

3. https://www.theverge.com/circuitbreaker/2018/4/27/17291040/intel-10nm-cannon-lake-chips-delayed-2019-cpu-processor

4. P. Shor, ‘Polynomial-Time Algorithms for Prime Factorization and Discrete Logarithms on a Quantum Computer’, *SIAM J. Comput.,* 26(5), 1484-1509, (1995).

5. Feynman, R.P., ‘Simulating Physics with Computers’, *International Journal of Theoretical Physics,* vol. 21/no. 6-7, (1982), pp. 467-488.

6. A. Kandala, J. Gambetta, ‘Hardware-efficient variational quantum eigensolver for small molecules and quantum magnets’, *Nature,* 549, 242-246, (2017).

7. Raimond, Brune, Haroche, ‘Colloquium: Manipulating quantum entanglement with atoms and photons in a cavity’, *Rev. Modern Phys.,* 73, (2001).

8. E. Majorana, ‘A symmetric theory of electrons and positrons’, *Ettorre Majorana Scientific Papers*, 201-233, (2006).

8.5 J. Cramer, N. Kalb, R. Hanson, T. H. Taminiau, ‘Repeated quantum error correction on a continuously encoded qubit by real-time feedback’, *Nat. Com.* 7, 11526 (2016).

9. A. Kitaev, ‘Unpaired Majorana fermions in quantum wires’, *Physics-Uspekhi*, 44, (2001).

10. R. M. Lutchyn, E.P.A.M. Bakkers, Y. Oreg, ‘Realizing Majorana zero modes in superconductor-semiconductor heterostructures’, *Nat. Rev. Mat.*, 3, 52-68, (2018).

2. Theory

In this Chapter first in section 2.1 the special properties of topological insulators (Bi_2Se_3, HgTe) and topological crystalline insulators (SnTe, $Pb_{1-x}Sn_xSe$) are discussed. These properties can be used for new Majorana devices, which are discussed in section 2.2. Finally in section 2.3 the basic concepts molecular beam epitaxy of SnTe is discussed.

2.1 Topological (crystalline) insulators: SnTe

Topological insulators[1-2] (TIs) are crystalline or non-crystalline materials that are insulating in the bulk but have conducting surfaces. An example is the surface of a 3-dimensional TI, where the bulk has a finite value for a certain topological invariant and the vacuum's topological invariant is zero. On the interface between the bulk and the vacuum, which is the surface of the TI, gapless surface states appear. The topological invariant for a TI, which is the Z_2 topological invariant[3], can be calculated from the Hamiltonian of the system and determines whether the system is topological or not.

In an inversion-symmetric material the Z_2 topological invariant only has a non-trivial value when the dispersion of the material shows band inversion. This means that the valence and conduction bands switch parity in comparison with the topologically trivial case[4]. The highest valence-band is then of even parity and the lowest conduction band is of odd parity. This band inversion is theoretically predicted for heavy-element materials such as HgTe and Bi_2Se_3, which are materials with a high spin-orbit coupling.

Fig. 2.1a-c) show the crystal structure of the 3D topological insulator Bi_2Se_3. The bandgap of Bi_2Se_3 is theoretically calculated to be in the range of $0.24-0.3$ eV[5,6]. Fig. 2.1d) and 2.1e) shows the single Dirac cone in the band structure corresponding to the conductive surface states of Bi_2Se_3 as measured using angle-resolved photoemission spectroscopy (ARPES). The band structure is shown as a function of two different directions in momentum space.

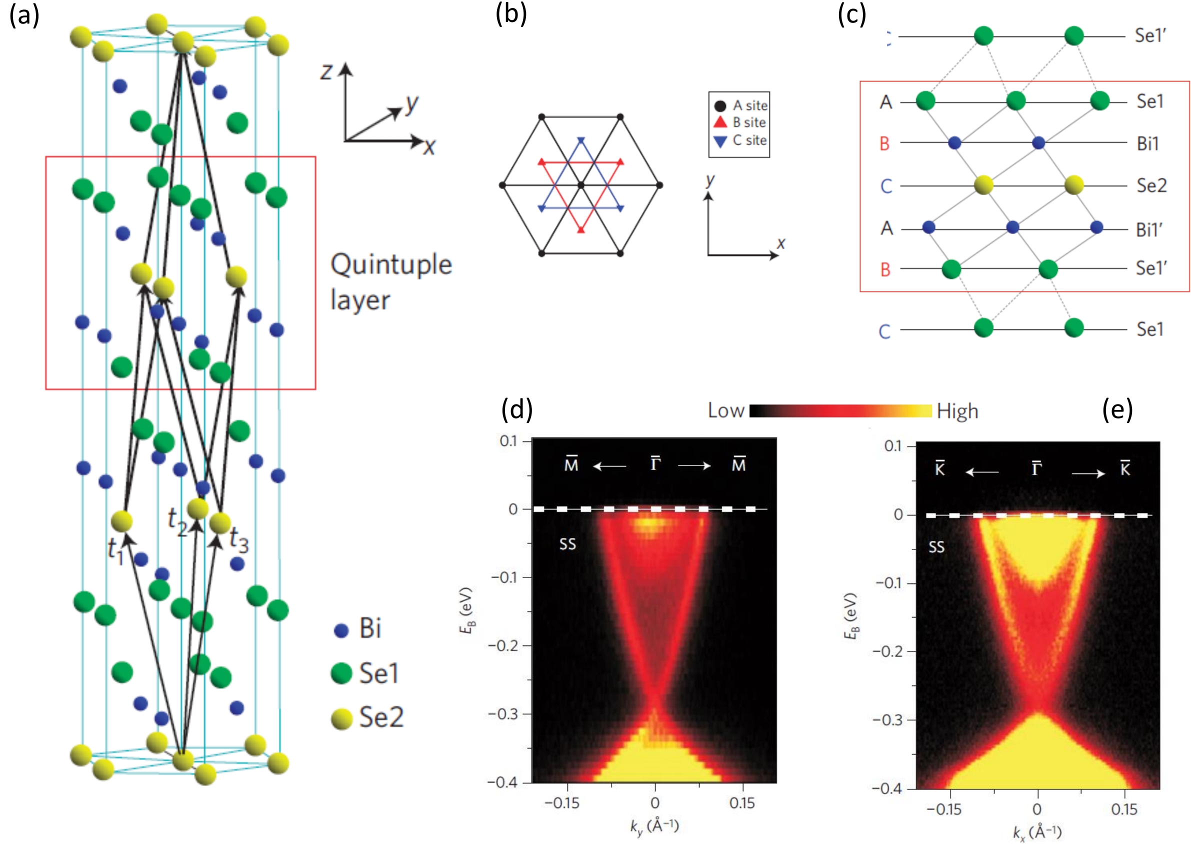

Fig. 2.1: (a) Crystal structure of Bi_2Se_3 with three primitive lattice vectors denoted by $t_{1,2,3}$. (b) Top view along the z-direction. (c) Side view of a quintuple layer structure. (d,e) High-resolution ARPES measurements of surface electronic band dispersion on Bi_2Se_3. Electron dispersion data measured with an incident photon energy of 22 eV near the $\bar{\Gamma}$-point along the $\bar{\Gamma} - \bar{M}$ (d) and $\bar{\Gamma} - \bar{K}$ (e) momentum space cuts. Figures are reproduced from ref. 5 and 6.

In contrast to TI's, topological crystalline insulators[7-8] (TCIs) are (narrow bandgap) semiconductors that have gapless surface states which are protected by the crystal symmetry of the periodic lattice. A TCI cannot be deformed into a topologically trivial insulator without breaking the particular crystal symmetry. The classification of TCIs is still in development[55-56], due to the large amount of different crystal symmetries and since combinations with T, P and C symmetry, which are the protecting symmetries of TIs, can be made. Due to a principle called bulk-boundary correspondence, only surfaces that preserve the same symmetry as the bulk are gapless. TCIs are theoretically predicted for the SnTe class of materials[14-18], transition metal oxides with a pyrochlore structure[9] and anti-perovskite materials[10].

Several TCIs are experimentally verified in the SnTe class of IV-VI semiconductors. This class contains pure and alloyed materials having the formula $Pb_{1-x}Sn_xTe$ and $Pb_{1-x}Sn_xSe$ and they are only predicted to be TCIs in their cubic rocksalt phase. Fig. 2.2 shows the rocksalt crystal structure of SnTe.
$Pb_{1-x}Sn_xTe$ is predicted to be topologically non-trivial for $x \gtrsim 0.4$[11]. However for temperatures below the ferroelectric temperature T_c it goes from the rocksalt to the rhombohedral crystal phase, therefore becoming topologically trivial (also called non-topological). $Pb_{1-x}Sn_xSe$ is topologically non-trivial for $0.23 \lesssim x \lesssim 0.4$[12-13]. It goes from the rocksalt to the rhombohedral crystal phase for

$x \gtrsim 0.4$[13]. The pure materials PbTe and PbSe are topologically trivial. Their bandgap is band-inverted in comparison to the pure rocksalt forms of the SnTe and PbSnSe.

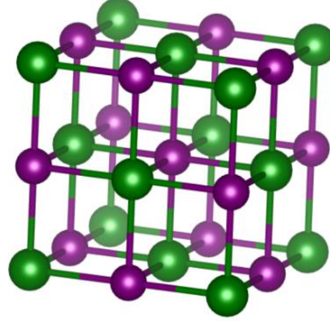

Fig. 2.2: Rocksalt crystal structure of SnTe.

As opposed to TIs, for which the Dirac cones are protected by time-reversal symmetry, for SnTe-type TCIs the Dirac cones are protected by mirror symmetry with respect to the $\{110\}$ family of planes[13]. The valence-band maxima and conduction-band minima are located at four equivalent L points in the Brillouin zone. In the vicinity of the L-points the band structure of for example the non-trivial SnTe shows band inversion with respect to the trivial PbTe. This band inversion means that for PbTe the eigenstates in the bottom of the conduction band are dominated by the orbitals of the Pb atom, while the top of the valence band is dominated by the Te atom. However for SnTe this behavior is inverted near the L-points as the top of the valence band is dominated by the Sn atom and the bottom of the conduction band is dominated by the Te atom. This band inversion will also be shown in the surface state calculations in section 4.1.1.

Materials in the SnTe class are no TIs, because band inversion takes place in an even number instead of odd number of points in the Brillouin zone. This means that the topological invariant for TIs, the Z_2 topological invariant is trivial for SnTe. However the crystal structure of SnTe is a face-centered cubic structure with a basis of two atoms, also called a rocksalt structure. This crystal structure is mirror symmetric with respect to the $\{110\}$ plane, i.e. the Hamiltonian of this system under mirror operation M satisfies

$$MH(k_1, k_2, k_3)M^{-1} = H(-k_1, k_2, k_3) \quad (2.1)$$

in which k_1 is along the direction perpendicular to the $[110]$ plane and k_2 and k_3 are parallel to this plane. Therefore on the $[110]$ plane, where $k_1 = 0$, the Hamiltonian commutates with the mirror operator, i.e. $[H, M] = 0$. Due to this fact a different topological invariant can be defined called the mirror Chern number. It has been shown that the mirror Chern number of PbTe $C_M = 0$, while for SnTe it is $C_M = -2$[13-14].

2.2 Comparison of different devices to create Majorana fermions

In this section Majorana devices are discussed. First in section 2.2.1 superconductor-semiconductor hybrid Majorana wires are discussed, which are heavy-element nanowires such as InAs and InSb in which superconductivity is induced by for example Al. These nanowires are promising candidates for Majorana devices. However TI/TCI nanowires or thin films could be a more reliable platform for these Majorana devices. Therefore in section 2.2.2 the application of TI nanowires in Majorana devices is discussed. Finally in section 2.2.3 quantum spin Hall Majorana devices are discussed, which will be applied later in section 4.2.3 on SnTe thin film superconducting junctions.

2.2.1 Superconductor-semiconductor hybrid nanowires

Topological quantum computing is not yet possible, as braiding of Majorana fermions has not yet been achieved. However the observation of the Majorana quasiparticle itself, has been reported[19]. The Majorana zero mode can be detected in tunneling spectroscopy experiments. In such an experiment a topological superconductor, realised by a hybrid material of a Rashba spin-orbit nanowire and a s-wave superconductor, is contacted between metal source and drain contacts, as shown in Fig. 2.3. In the conductance measurement of the Majorana wire a resonant peak quantized at a differential conductance of $\frac{dI}{dV} = \frac{2e^2}{h}$ will appear in the weak tunneling limit, independent of the tunnel barrier strength[20]. This is due to the resonant Andreev reflection caused by the Majorana particle located in the middle of the normal-barrier-superconductor junction. The semiconductor nanowire used in this experiment needs to show ballistic transport[21] and must therefore be defect-free. Besides that, the spin-orbit energy and the g-factor need to be large. The relevant parameters for the semiconductors and superconductors that are typically used in Majorana devices are listed in Table 2.1[22].

The nanowire can be brought into the topological phase by applying a magnetic field parallel to the wire and an electric field perpendicular to the wire. The topological phase, in which Majorana fermions appear on the ends of the nanowire, is satisfied when the Zeeman field

$$E_z > \sqrt{\Delta^2 + \mu^2}, \tag{2.2}$$

where Δ is the superconductive gap induced by the superconductor into the semiconductor and μ is the chemical potential with respect to the bottom of the conduction band.

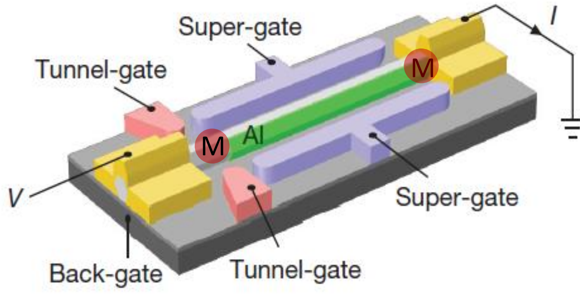

Fig. 2.3: Schematic of Majorana wire experiment[19]. The yellow contacts are the source (V) and drain (I) contacts. The red 'tunnel-gate' contacts set the height of the tunneling barrier between the normal contact and the topological superconductor. The blue contacts control the chemical potential of the nanowire. The Majorana fermions at the normal-superconductor interface and at the other end of the nanowire are indicated by an $'M'$.

Table 2.1: Parameters of semiconductors and superconductors typically used in Majorana devices[22].

Semiconductors	InAs	InSb
spin-orbit energy	$0.05 - 1$ meV	$0.05 - 1$ meV
g-factor	8 – 12	40 – 50
Superconductor	Al	NbTiN
type	type I	type II
gap Δ	0.2 meV	3 meV
critical field B_c	10 mT	10 T
T_C	1.2 K	15 K

To understand how the magnetic and electric fields bring the nanowire in the topological phase, now the dispersion of the Majorana wire is discussed in the 1D approximation. This is done by looking at the effects of a magnetic field and spin-orbit coupling separately. In Fig. 2.4a) the effect of only a Zeeman field on a nanowire is illustrated. When starting with a spin-degenerate parabolic dispersion, the Zeeman field shifts the different spin-branches upward or downward in energy. The spins of both bands are opposite and aligned parallel to the nanowire. In Fig. 2.4b) the effect of only the Rashba spin-orbit coupling, which scales with the applied electric field, is illustrated. When starting again with the spin-degenerate parabolic dispersion, the spin-orbit coupling splits the parabola in the k-direction, with the spins of both parabolas opposite but now aligned perpendicular to the nanowire. In Fig. 2.4c) the combined effect of the Zeeman field and the spin-orbit coupling on the nanowire dispersion is illustrated. The dispersion is now similar to the case without Zeeman field (Fig. 2.4b)), but now a Zeeman gap is opened where the parabolas used to intersect. Also now both bands have an opposite spin, aligned between perpendicular and parallel to the nanowire. Note that when the chemical potential is inside the Zeeman gap in Fig. 2.4c), the chemical potential intersects the bottom band at two points with a different spin and opposite momentum. This situation is similar as is seen in a topological insulator nanowire where (see section 2.2.2), if the chemical potential is in the gap of the TI, it will intersect the dispersion at two points with opposite spin and opposite momentum.

Next the superconductivity is added to the dispersion of Fig. 2.4c), which can for example be induced in the semiconductor by a layer of NbTiN or Al, which are s-wave superconductors. An s-wave superconductive coupling has the effect that a mirror image of the dispersion, with respect to the Fermi level, is superimposed to the original dispersion. On top of that, a superconducting gap of size 2Δ proportional to the strength of the superconducting coupling, is opened up around the Fermi level. The topological state is achieved by placing the chemical potential inside the Zeeman gap. Fig. 2.5 shows the resulting dispersion. The dispersion is called topological due to its band inversion: The bands above the superconducting gap are hole-like (near $k = 0$) while the bands below the superconducting gap are electron-like. This is opposite to the normal case in semiconductor where above the Fermi level states are electron-like, while below it they are hole-like.

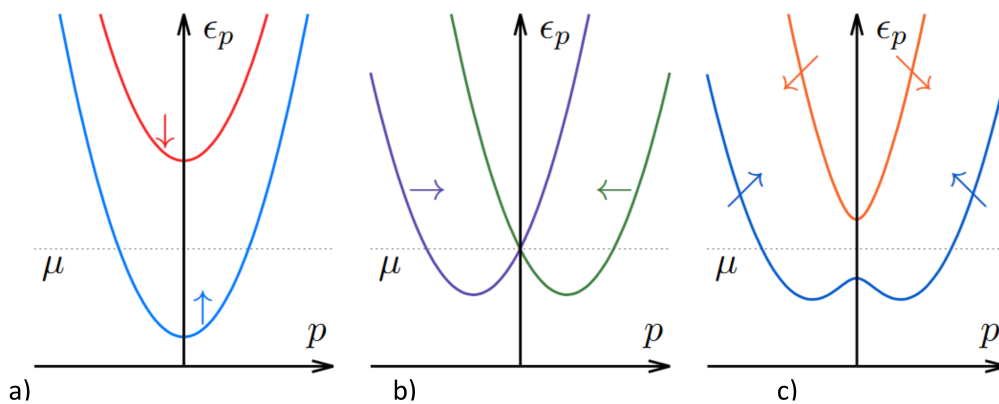

Fig. 2.4: From left the right, nanowire dispersion with only Zeeman field (Kitaev limit), with only spin-orbit coupling (topological-insulator limit without Zeeman field) and with spin-orbit coupling and Zeeman field combined (topological-insulator limit without Zeeman field). Figures are reproduced from ref. 23.

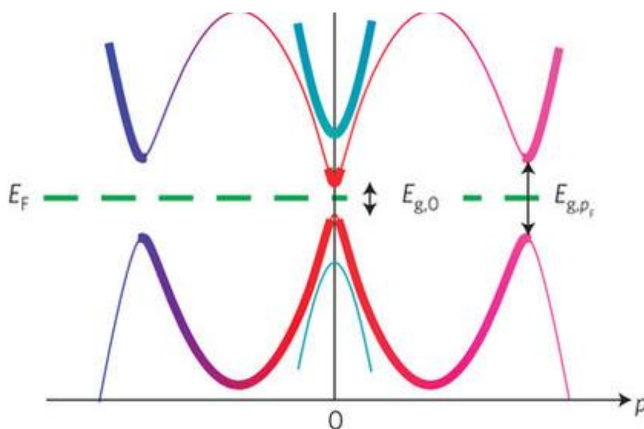

Fig. 2.5: Nanowire dispersion with spin-orbit coupling and Zeeman field combined and induced s-wave superconductivity. Figure is reproduced from ref. 24.

2.2.2 Topological insulator Majorana wires

In this section the application of topological insulators for Majorana devices is investigated. Topological insulators have been compared with Rashba spin-orbit semiconductors by Cook and Franz[25-26]. In both cases a magnetic field is needed to bring the nanowires into the topological phase. Fig. 2.6 shows the setup for the TI nanowire, where a magnetic field $\vec{B}$ is applied along the nanowire axis. Fig. 2.7a) shows the modeled dispersion of a topological insulator like Bi_2Se_3 without magnetic field[25]. It can be seen that the Dirac cone is actually not there without a magnetic field. A magnetic flux through the nanowire cross section of approximately a half-integer multiple of the magnetic flux quantum $\Phi_0 = \frac{h}{e}$ is needed to realize a 1D topological superconductor on the topologically protected surface of the nanowire.

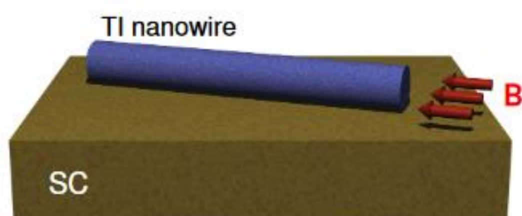

Fig. 2.6 Schematic of a TI Majorana nanowire with a magnetic field $\vec{B}$ applied along the nanowire axis[25].

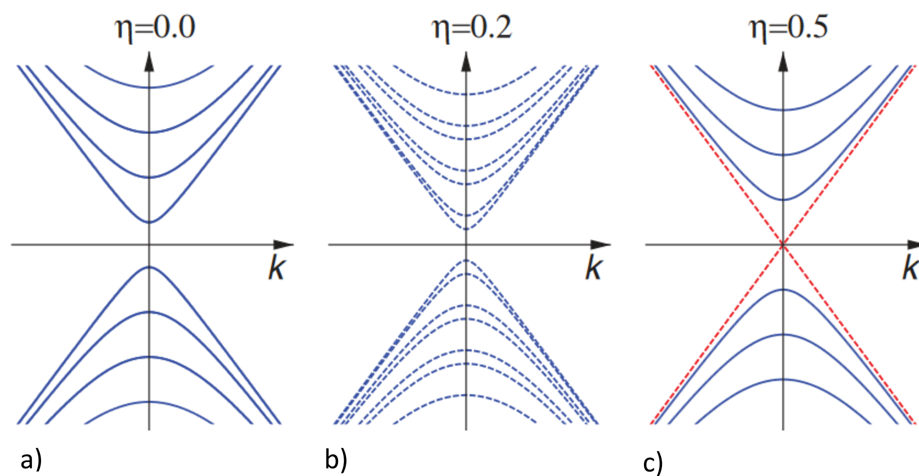

Fig. 2.7: Surface-state excitation spectra E_{kl} of a topological insulator without induced superconductivity for various values of magnetic flux $\Phi = \eta\Phi_0 = \eta\frac{h}{e}$. Figures are reproduced from ref. 25.

Fig. 2.8 shows the results of simulating a TI nanowire with 6×6 cross-section, where a model by Fu and Berg[27] was used to model the Hamiltonian of the topological insulator. To simulate the magnetic field a Peierls substitution (section 4.1.4) and Zeemann Hamiltonian (section 4.1.4) were implemented, while a BdG Hamiltonian was used to include s-wave superconductivity (section 4.2.1).

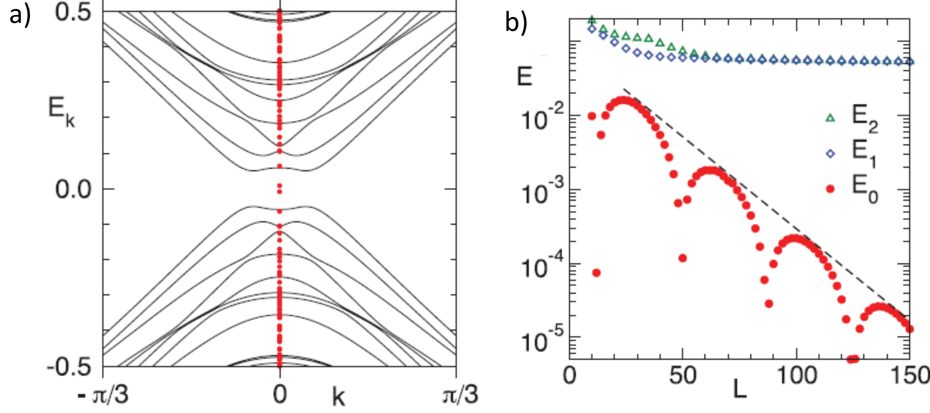

Fig. 2.8: (a) Energy bands for an infinitely long TI wire with a 6×6 base in the SC state with $\eta = 0.49$, $\mu = 0.09$, $\Delta_0 = 0.08$, and $g = 0$ (solid lines), and the energy levels for a $L = 36$ finite-length wire with open boundary conditions (red circles) obtained by exact numerical diagonalization. (b) Three lowest positive energy eigenvalues obtained by the Lanczos method as a function of L. Figures are reproduced from ref. 25.

The main advantage of using topological insulators instead of high spin-orbit semiconductors for Majorana devices is the larger energy range on which the nanowire is topological. For the topological phase to occur in a semiconductor nanowire the chemical potential must be tuned exactly so that it lies inside the Zeemann gap, whose typical size is $\sim 1 \text{ meV}$ or less in a 1 T magnetic field. However in a TI the nanowire is in a topological phase whenever the chemical potential is inside the bulk gap. For a TI such as Bi_2Se_3 the typical tuning range of the chemical potential is then as high as $\sim 300 \text{ meV}$. This tuning is important because the small tuning range of semiconductor nanowires seems to cause problems in experiments. In a research[13] of semiconductor Majorana wires many (>60) devices were tested, out of which 11 devices were selected. Only 2 of these devices[13] could be brought into the topological phase by tuning the chemical potential in the Zeemann gap using a back-gate. These problems arise because the back-gate often only allows to tune the chemical potential in a certain range, which may not be enough to achieve the topological phase. Thus the tuning range of the chemical potential in which the nanowire is topological is important to improve yield when fabricating Majorana devices.

2.2.3 Superconducting quantum spin Hall insulators

As will be discussed in section 4.1.2 the SnTe $[111]$ thin film is a quantum spin Hall insulator (QSHI). There are multiple proposals and experimental advances for the detection and braiding of Majorana fermions in QSHIs[28-30]. The geometries used to generate Majoranas in QSHI thin films seem to be more complicated than the proposals for TI nanowires. As proposed in literature[30] Majorana fermions can be generated at superconductor/QSHI/superconductor junctions. Fig. 2.7a) shows a QSHI at the edge of a disc. Pairs of edge states run over the inner and outer edges of the disc. The whole outer edge of the disc is brought into contact with a superconductor with superconducting order parameter Δ, except for a part of the edge of length L, which we'll call the junction. By introducing a magnetic flux Φ though the hole in the disc a superconducting phase difference φ is generated at both sides of the junction. This phase is realized by including it as a phase term in the superconducting order parameter $\Delta = \Delta e^{i\varphi}$. When this phase difference is exactly $\varphi = \pi$, 1 Majorana fermion is generated at each end of the junction.

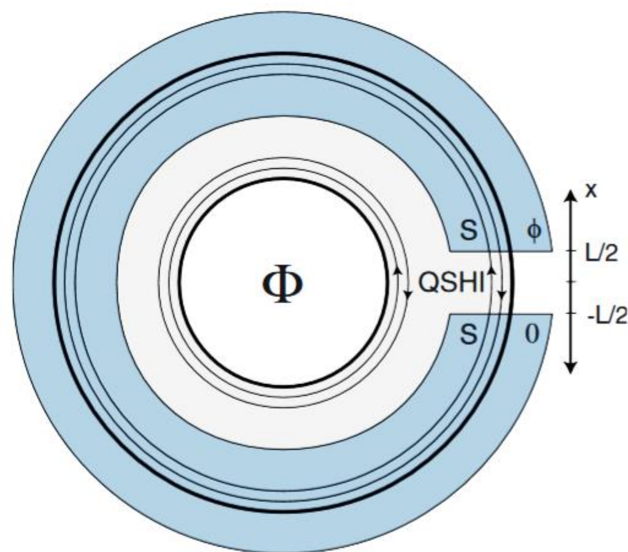

Fig. 2.7: A S/QSHI/S junction in a RF SQUID geometry where the QSHI forms a Corbino disk[30].

2.3. Molecular beam epitaxy of SnTe and $Pb_{1-x}Sn_xTe$

In this Chapter the results of literature study on MBE growth of $Pb_{1-x}Sn_xTe$ thin films and nanowires are discussed. In section 2.3.1 the basic concepts of MBE are discussed and the important parts of the machine are shown. Then in section 2.3.2 the choice of substrate is discussed, mostly in the context of thin film growth. Next in section 2.3.3 the basic concepts of nanowire growth and relevant phase diagrams for SnTe nanowire growth are discussed. Finally section 2.3.4 treats the fact that SnTe is generally found to be p-doped spontaneously.

2.3.1 General introduction to molecular beam epitaxy

The growth method used in this research is molecular beam epitaxy (MBE). MBE is an epitaxial process by which growth of materials takes place under ultra-high vacuum (UHV) conditions. Material is grown on a heated crystalline substrate by the interaction of adsorbed species supplied by atomic or molecular beams[31]. To obtain high quality materials the deposits should have the same crystalline structure of the substrate or a structure with similar symmetry and lattice parameters. The beams generally have thermal energy and are produced by evaporation or sublimation of suitable materials contained in ultra-pure crucibles.

An advantage of MBE is that diagnostic techniques monitoring the growth, such as reflection high-energy electron diffraction (RHEED), are available inside the growth chamber. Also growth temperatures can be lower than other growth method such as for example metalorganic vapour-phase epitaxy (MOVPE). This is because growth precursors are supplied in elemental form so that they do not have to be dissociated or cracked anymore. This is needed for example for the growth of InSb in MOVPE where among others the precursor tri-methyl-indium is needed. The result of these lower growth temperatures is a reduced amount of thermodynamical defects.
Another interesting property of MBE is that during growth the composition or doping of structures can be varied in well controlled abrupt or continuous profiles. This feature makes it possible to grow for example quantum wells, in which carriers are confined in 2D or 3D regions with sizes smaller or comparable to the de Broglie wavelength of carriers[32].

Fig. 2.8a) shows a schematic view of the MBE growth chamber. It is a vacuum sealed stainless steel vessel with on the inside cryopanels kept at liquid nitrogen temperature to remove contaminants from the growth. The cryopanels also thermally insulate the different effusion cells. The effusion cells are at the bottom of the MBE system and produce molecular beams pointed upward in the direction of the substrate. Shutters are mounted above the openings of the effusion cells so that molecular beams can be switched on and off instantly. A substrate holder heatable up to several hundreds of °C is located in the middle of the chamber pointing downward to the effusion cells. It is mounted to a manipulator that can rotate the sample during growth. A loadlock system allows for the introduction and extraction of wafers into and out of the growth chamber without breaking the UHV. In section 3.2.3 we discuss how UHV is reached.

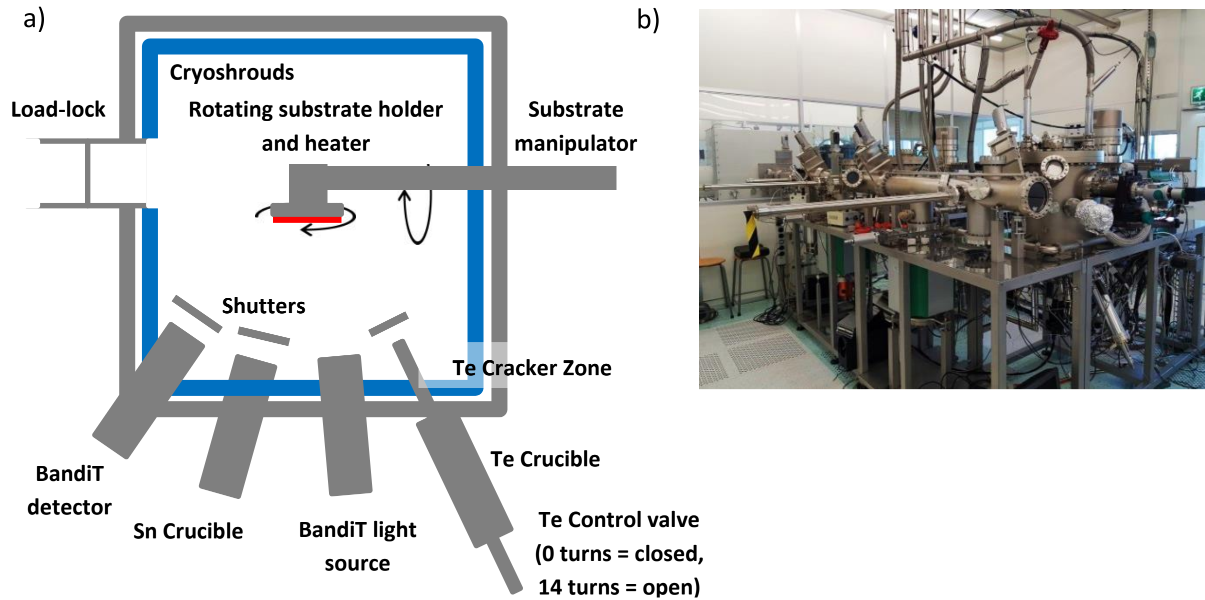

Fig. 2.8: (a) Schematic view of the MBE growth chamber.[32](b) Photo of our III/V and IV/VI MBE reactors.

In IV-VI MBE constituents are usually supplied in the form of compound effusion sources such as PbTe, PbS and SnSe since the compounds evaporate mostly in the form of binary molecules[57-59]. However for some IV-VI materials such as GeTe and SnTe the binary dissociates quickly. This results in more Sn on the target substrate then Te since Te is volatile and Sn sticks to the surface. Therefore an additional small Te flux is needed to retain the stoichiometry of the layers. In our case elemental effusion sources are used. Stoichiometric layers are formed when a sufficient excess of group VI flux is supplied to compensate the much higher reevaporation rates of the VI elements compared to those of the group IV elements. See also section 5.2 for the reevaporation rates of group IV and VI elements and compounds.

The effusion temperatures in our growth are typically between 980 and 1200 °C for Sn and between 285 and 310 °C for Te. For the Te source a cracker cell is used. The valved cracker cell, whose needle valve tip is kept at 650 °C, effectively modulates the flux. The Te beam passes through a needle valve, made of heat resistant Pyrolytic Boron Nitride (PBN), which can be opened and closed. A special heating system is attached to the top of the cell for much higher temperatures than the evaporation temperature. Insulation parts are used to minimize crosstalk between the two heating stages. With our system very low fluxes of material can be achieved.

2.3.2 Substrates and $Pb_{1-x}Sn_xTe$ film growth

For the choice of substrate it is first of all important that the substrate is lattice matched with the material to be grown. Lattice matching means that the lattice constant and the crystal structure, e.g. zinc blende, wurtzite or rocksalt, are the same. Moreover the place in the periodic table of elements of the materials should be the same. Otherwise a layer of trapped charges can form on the interface of the substrate and the grown epitaxial crystal. Besides lattice matching, it can be important that

the substrate, and if present a capping layer, have a higher bandgap than the crystal to be studied. Hereby charge carriers can be confined to the target material and electronic transport in this material can be investigated. In Fig. 2.9 the lattice constant of various semiconductors and substrates are plotted with a lattice parameter close to the lattice parameter of SnTe (0.63 nm). Finally thermal expansion coefficients k of the grown materials should be comparable so that stress emerging during cooldown after growth at high temperature is reduced.

In literature different substrates are used to grow IV-VI materials like $Pb_{1-x}Sn_xTe$. The most used are BaF_2 (111), IV-VI substrates, KCl and NaCl, silicon, GaAs and CdTe. For the growth performed in this report substrates were mostly chosen because of their good availability and at least to some extent due to their crystal symmetry. For example for GaAs the $[001]$ substrate was used instead of the $[111]$ substrate because SnTe nanowire growth in the $[001]$ direction was expected. Namely the $[001]$ surface is expected to have the lowest energy of formation due to the lowest amount of dangling bonds. However less effort was put to achieve the perfect lattice matching since lattice mismatching is less important for nanowires than for thin films. This is because nanowires can relax stress caused by lattice mismatching much easier than thin films. The following study of lattice matched growth may thus not be directly relevant for SnTe nanowire growth, however will be important for eventual thin film growth in the future or further attempts to improve the nanowire growth.
Relevant properties of commonly used substrates for $Pb_{1-x}Sn_xTe$ growth are listed in Table 2.2. The thermal strain at room temperature is defined as $\varepsilon_{th} = (\beta_{\mathrm{SnTe}} - \beta) \times 300\mathrm{K}$, where β is the thermal expansion constant of the substrate.

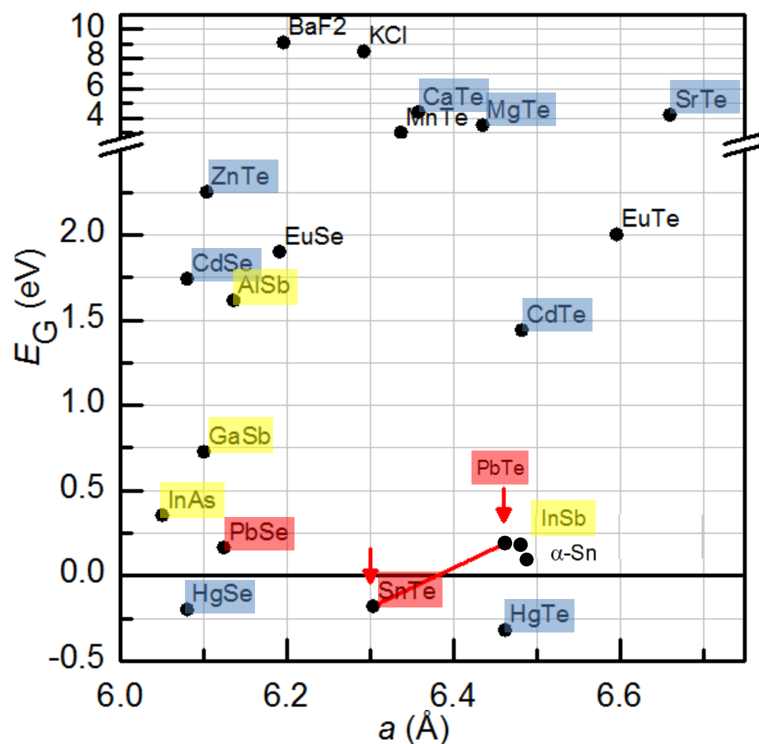

Fig. 2.9: Lattice constant vs. bandgap diagram for III-V (yellow), II-VI (blue) and IV-VI (red) semiconductors and insulators with a lattice constant close to $Pb_{1-x}Sn_xTe$ (0.630 to 0.646 nm). Also substrates such as BaF_2 and KCl are shown.

Table 2.2: Crystal structure, lattice mismatch, thermal strain and bandgap data for common substrates used to grow $Pb_{1-x}Sn_xTe$[33].

Substrate	Crystal structure	Lattice mismatch to SnTe (%)	Thermal strain at RT (%) $\varepsilon_{th} = (\beta_{\mathrm{SnTe}} - \beta) \times 300\mathrm{K}$	Bandgap (eV)
BaF_2	Calcium fluoride	-1.6	0.07	9
KCl	Rock salt	-0.16	-0.54	6.4
NaCl	Rock salt	-10.5	-0.57	9
Silicon	Diamond	-13.8	0.55	1.17
Ge	Diamond	-10.2	0.45	0.67
GaAs	Zinc blende	-10.3	0.45	1.42
CdTe	Zinc blende	2.9	0.49	1.49
PbTe	Rock salt	2.6	0.04	0.319

BaF_2 is probably the most used substrate. As can be seen in Table 2.2 its lattice mismatch to SnTe is for example only 2% and its thermal strain with respect to SnTe is only 0.07%. Besides that BaF_2 is highly insulating and optically transparent[33]. The (111) surface is mostly used because is the lowest energy surface and it is easily obtained by cleaving. For PbTe films on BaF_2 (111) the growth starts in a 3D Vollmer-Weber growth mode, with triangular shaped pyramidal islands having (100) side facets[34]. This is a consequence of the (100) surface being the lowest energy surface for lead salt compounds. The lattice mismatch of 4% of BaF_2 compared to PbTe does not play a major role for this nucleation behavior, since 3D nucleation on BaF_2 (111) is also observed for ternary $PbTe_{1-x}Se_x$ layers lattice-matched to BaF_2.
However Fig. 2.10 shows that in this type of growth threading dislocations are presents, which form pinning centers for surface steps that form the center of growth spirals on the surface. Growing thicker layers will decreases the number of dislocations, increasing the mobilities found in transport measurements. Finally the BaF_2-PbTe surface is p-type, which means that growing thicker layers also decreases the average p-type charge carrier density[35-36].

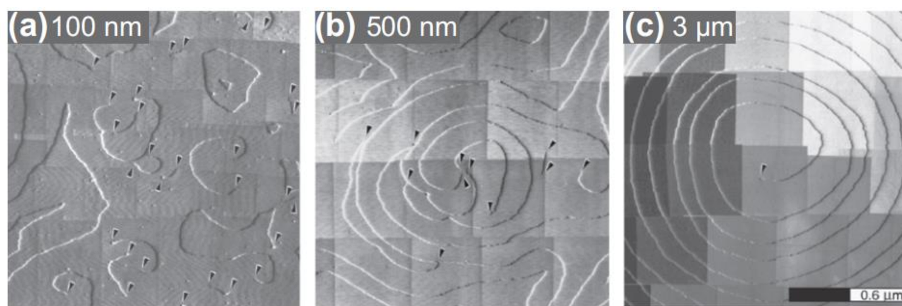

Fig. 2.10: STM images of PbTe growth on BaF_2 (111) for deposit thicknesses of (a) $100\,\mathrm{nm}$, (b) $500\,\mathrm{nm}$ and (c) $3\,\mu\mathrm{m}$. The arrow heads indicate the threading dislocations penetrating the epilayer surface.[37]

Although they are not commercially available, also IV-VI substrates can be used in $Pb_{1-x}Sn_xTe$ growth. They are generally not suited for low-dimensional heterostructures due to high carrier densities ($> 10^{17}\ \mathrm{cm}^{-3}$). They are mechanically soft and oxides have to be removed before growth by for example bromine-based etching. Independent of the ternary composition and strain value growth

occurs in the 2D Frank van der Merwe (layer-by-layer) growth mode. Fig. 2.11 shows that for film growth of PbTe on PbSe, lattice mismatch between both materials results in a network of misfit dislocation defects.

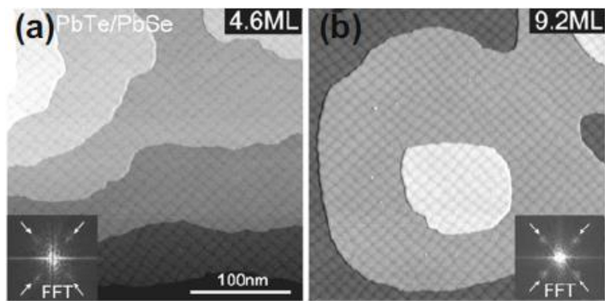

Fig. 2.11: STM surface images of PbTe on PbSe showing a highly ordered array of pure edge misfit dislocations caused by compressive strain[38].

Due to their (100) cleavage planes, KCl and NaCl can be used for growing (001) films. KCl has an even lower lattice mismatch than BaF_2 of only 0.16%. However growth of IV-VI materials on these substrates results in high defect densities and therefore electrical properties inferior to the bulk material. For example $Pb_{1-x}Sn_xTe$ layers on KCl exhibit smooth surfaces but the $77\ \mathrm{K}$ mobilities are much lower than layers deposited on BaF_2 (111) substrates[39]. A reason for this could be the high thermal strain caused by these substrates.

2.3.3 Nanowire growth and material aspects of SnTe

Since SnTe nanowires are promising for Majorana devices the growth goal of this research is SnTe nanowires. In this section the basic growth concept of nanowires is discussed. Nanowires are often grown in the vapor-liquid-solid[40] (VLS) growth mode. This method promotes growth to occur in one direction, so that the nanowire geometry instead of bulk growth is achieved. During VLS growth a seed particle, such as a gold particle of ~ 10 nm, is used to catalyze the growth of a nanowire. As Fig. 2.12 shows first (1) seed particles are formed and (2) heated up to the growth temperature. Then (3) the growth materials are supplied in the gas phase and form liquid alloys with the seed particles. At some composition (4) the particles are supersaturated and pass the liquidus curve (transition from liquid to liquid + solid). Eventually (5) the solid nanowire phase nucleates and begins to grow. The role of the seed particles is to provide preferential sites for decomposition of growth precursors. The growth temperature should be low enough to prevent the decomposition of grown structures, however, for growth methods like MOVPE, high enough to crack growth precursors. For MBE however this means that growth can occur at much lower temperatures
With a growth mechanism called vapor-solid-solid (VSS) growth, it is possible to grow nanowires with a growth temperature below the eutectic point[41], so that the seed particle is solid.
Finally one should keep in mind that phase diagrams only take into acount thermodynamics, while kintic processes could also play an important role during the growth.

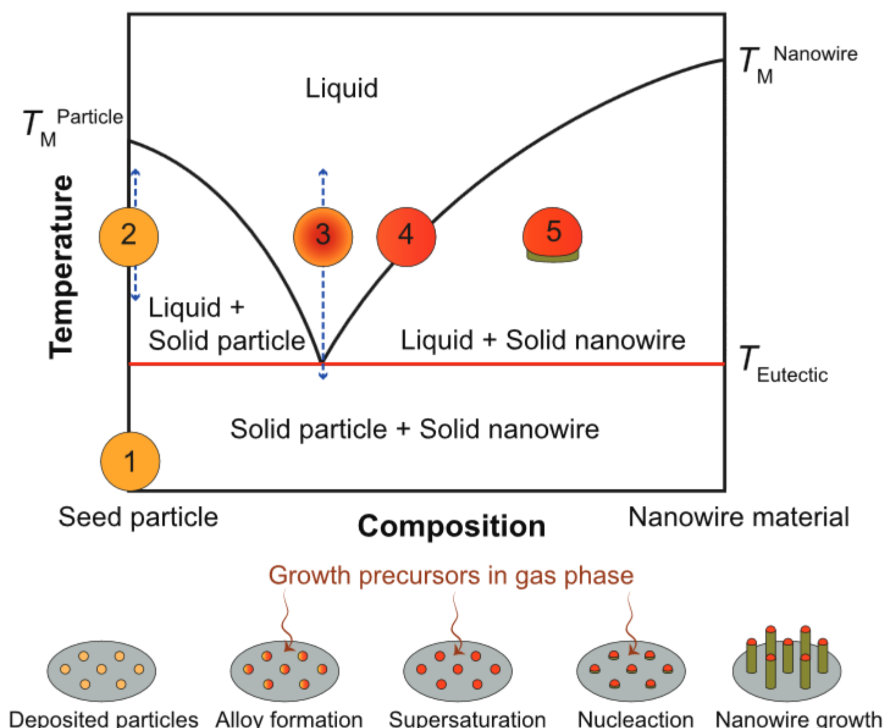

Fig. 2.12: An illustration of the VLS growth based on the temperature-composition phase diagram of the growth materials system. $T_M^{Particle}$, $T_M^{Nanowire}$ *and* $T_{Eutectic}$ *denote the melting points of the seed particle, the nanowire material(s) and the eutectic point, respectively. The involved steps are also shown on the bottom of the phase diagram.*[40]

Unfortunately the phase diagram for the gold catalyst and SnTe was not found. However Fig. 2.13 shows related band diagrams. The AuSn-SnTe (Fig. 2.13a)) and $AuTe_2$-SnTe (Fig. 2.13b)) phase diagrams could already give an idea for the Au-SnTe growth. The eutectic point for AuSn-SnTe is at $T_E = 413$ °C and a SnTe concentration of $x_E = 1.3\%$. For $AuTe_2$-SnTe the eutectic point is at $T_E = 402$ °C and a SnTe concentration of $x_E = 32.5\%$. This indicates that if the gold droplet is first filled up with Sn or Te, nanowire growth can occur at high temperatures.

Fig. 2.13c) and Fig. 2.13d) show the Au-Sn and Au-Te phase diagrams respectively. The eutectic point for the Au-Sn phase diagram is at $T_E = 232$ °C and a Sn concentration of $x_E = 93.7\%$. However there is also a minimum in the liquidus line at $T_E = 290$ °C and $x_E = 29.0$. The phase diagram indicates that a Au-Sn liquid droplet can exist at temperatures under 419.3 °C, but that the droplet will only be $50/50$ Au-Sn for higher temperatures. For the Au-Te phase diagram $T_E = 416$ °C and $x_E = 88.0$. So to have a Au-Te liquid alloy the temperature must be much higher than for a Au-Sn alloy.

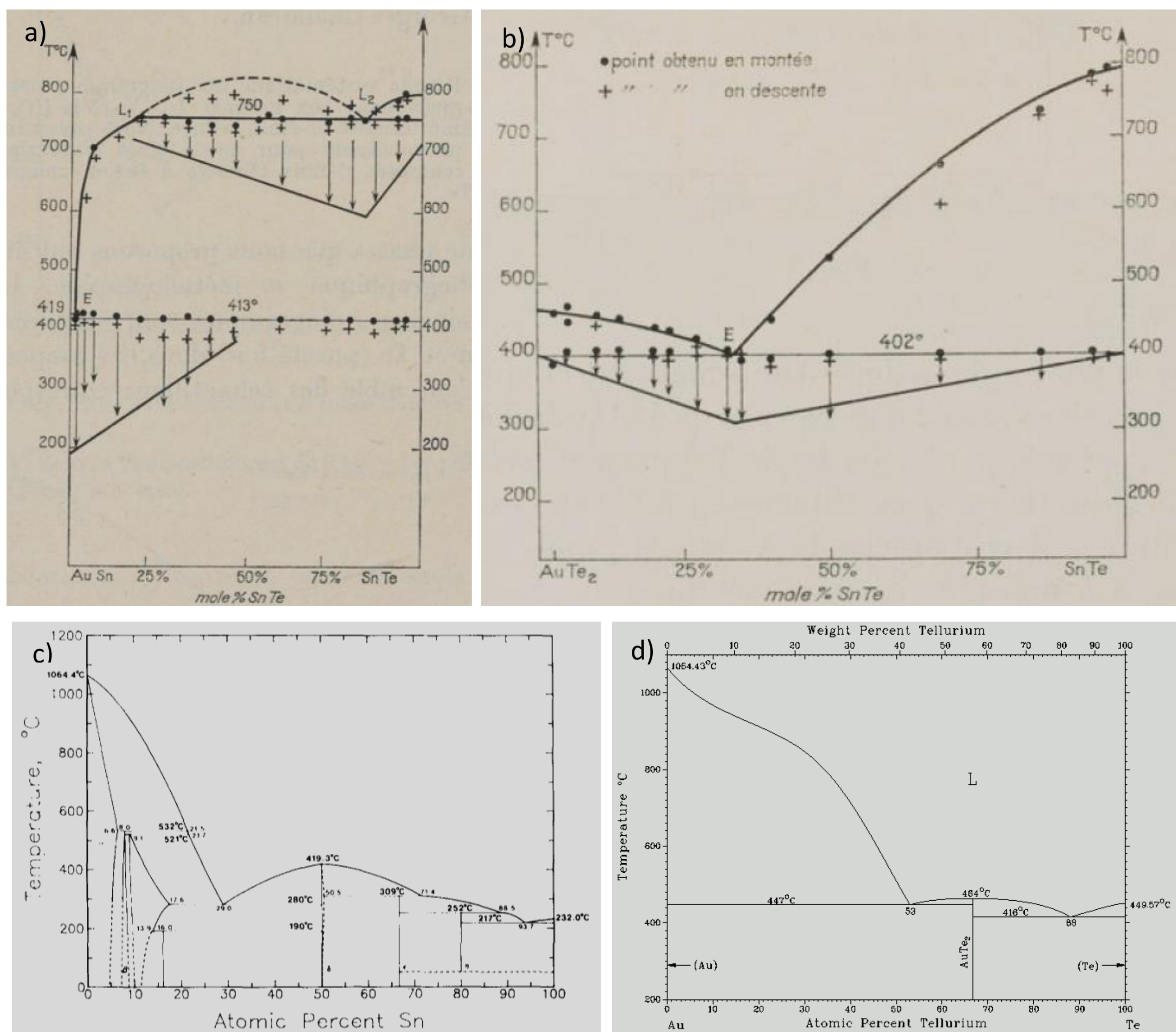

Fig. 2.13: Phase diagram of the (a) AuSn-SnT[42], (b) $AuTe_2$-SnTe[42], (c) Au-Sn[43] and (d) Au-Te[44] lines.

2.3.4 The p-doping problem of SnTe and consequences

The challenge for growing SnTe is to actually realize a low charge carrier density. Namely the special properties of the TCI are only available when the Fermi level is tuned within the band gap. However transport measurements on SnTe always find p-type conductance[45-47], while for the non-topological material PbTe both n-type and p-type behavior are found[46,48]. As Fig. 2.14 shows the charge carrier density can be tuned by varying the Pb/Sn ratio in $Pb_{1-x}Sn_xTe$. The carrier type of PbTe and compounds such as $\mathrm{Pb_{0.8}Sn_{0.2}Te}$ can also be controlled by controlling the temperatures of the effusion sources[50]. Finally the carrier type can be controlled by changing the IV/VI flux ratio. Excess group IV flux leads to n-type conductance, while excess group VI flux leads to p-type conductuctance. Te vacancies act as doubly charged donor states while Sn vacancies act as doubly charged acceptor states[52-54]. Carrier concentrations of IV-VI epilayers below $10^{16}\ \mathrm{cm}^{-3}$ have not been achieved.

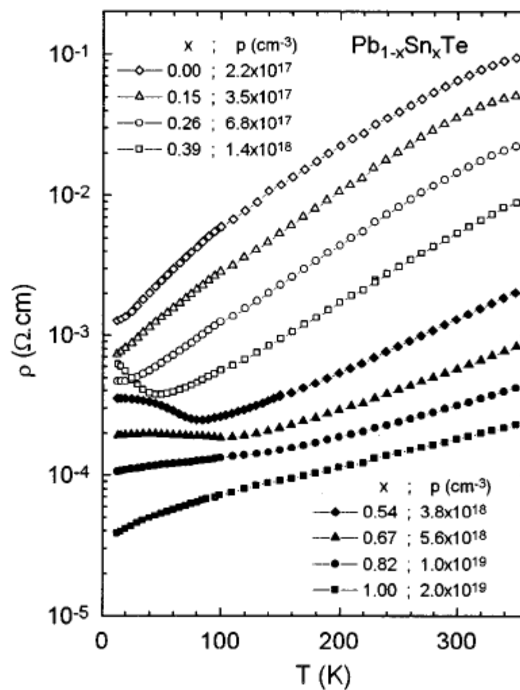

Fig. 2.14: Temperature dependence of the resistivity in $Pb_{1-x}Sn_xTe$ epitaxial layers with different x values.[49]

Using first-principles calculations the microscopic origin of the p-type conductivity of SnTe is indentified[51]. Fig. 2.15 shows the result of the calculations of defect formation energies. The negatively charged Sn vacancy (V_{Sn}^{2-}) dominates the electronic properties of SnTe: Regardless of the growth conditions, V_{Sn}^{2-} always has a negative formation energy within the band gap, which forces the Fermi level below the valence band maximum (VBM).

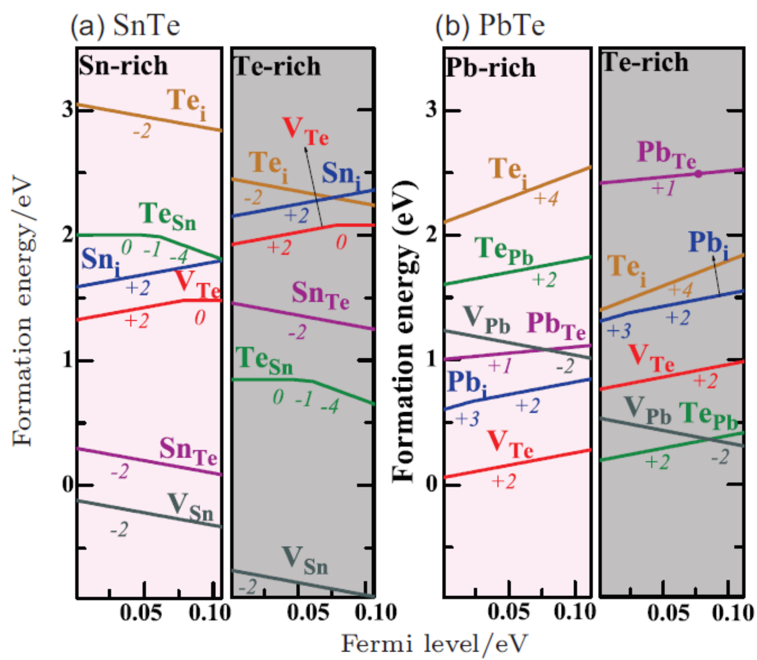

Fig. 2.15: Defect formation energies as a function of Fermi level for native point defects in (a) SnTe and (b) PbTe under Sn/Pb-rich and Te-rich conditions. Zero of the Fermi level is set to the VBM of the host. The Fermi level range spans the bulk gap. Figures is reproduced from 51.

It should be kept in mind that these calculations only hold in thermal equilibrium and in bulk. This is both not the case in MBE nanowire growth. No attempts were done yet to measure the charge carrier density of our samples. However plans are made to do this in nanowire field effect experiments.

2.3.5 SnTe nanowire growth by other growth methods

SnTe nanowires are also grown by other methods than MBE[60-64]. Most of these nanowires are grown in chemical vapor deposition methods and are Au or Sn[62] catalyzed. Reported nanowires generally have $\{001\}$ facets. Reported substrates include among other Si and mica[62].
Some papers suggest that topological phases of these SnTe nanowires are confirmed. For example it was shown in low temperature magnetotransport[61] that PbTe nanowires exhibit the weak localization (WL) effect, whereas $Pb_{0.5}Sn_{0.5}Te$ and $Pb_{0.2}Sn_{0.8}Te$ nanowires display the weak antilocalization (WAL) effect. Consequently the WAL is attributed to the topological phase of the nanowires. However interpretation of these transport studies is very questionable. Namely while looking at the temperature dependence of the resistance it was also reported that the PbTe nanowires have semiconducting (probably n-type) characteristics, whereas the SnTe nanowires are highly metallic and probably p-type.

Additionally papers report PbSnTe to have a higher thermoelectric figures of merit ZT compared to bulk samples, due to a high thermopower and low thermal conductivity. The thermopower of PbSnTe is suggested to be enhanced due to topological surface states, while the suppression of thermal conductivity is suggested to be due to increased phonon-surface scattering. Attributing the high ZT to the topological surface states is again questionable, since the nanowires showed metallic behavior[63].

References Chapter 2

1. C.L. Kane, Liang Fu, 'Topological insulators with inversion symmetry', *Phys Rev B* 76, 045302, (2007).
2. Y. Ando, 'Topological Insulator Materials', *J. Phys. Soc. Jpn.* 82, 102001, (2013).
3. C.L. Kane, E.J. Mele, 'Z_2 topological order and the quantum spin hall effect', *Phys Rev Lett* 95¸146802, (2005).
4. https://topocondmat.org/w5_qshe/qshe_experiments.html
5. H. Zhang, 'Topological insulators in Bi2Se3, Bi2Te3 and Sb2Te3 with a single Dirac cone on the surface', Nature Physics, Vol. 5, (2009).
6. Y. Xia, 'Observation of a large-gap topological-insulator class with a single Dirac cone on the surface', Nature Physics, Vol. 5, (2009).
7. L. Fu, 'Topological Crystalline Insulators', Phys. Rev. Lett, 106, 106802, (2011).
8. Y. Ando, 'Topological Crystalline Insulators and Topological Superconductors: From Concepts to Materials', Annual Review of Consensed Matter Physics 6, 361-381, (2015).
9. M. Kargarian, G. A. Fiete, 'Topological Crystalline Insulators in Transition Metal Oxides', Phys. Rev. Lett. 110, (2013).
10. T. H. Hsieh, J. Liu, L.Fu, 'Topological crystalline insulators and Dirac octets in antiperovskites', Phys. Rev. B 90, (2014).
11. L. Fu, C.L. Kane, 'Topological insulators with inversion symmetry', *Phys. Rev. B* 76, (2007).
12. P. Dziawa, B.J. Kowalski, K. Dybko, R. Buczko, T. Story, 'Topological crystalline insulator states in $\mathrm{Pb}_{1-x}\mathrm{Sn}_x\mathrm{Se}$', *Nat. Mat.* 11, 1023-1027 (2012).
13. A. Rogalski, K. Adamiec, 'Nannow-gap Semiconductor Photodiodes', *SPIE Press*, (2000).
14. T. Hsieh, H. Lin, J. Liu, W. Duan, A. Bansil, L. Fu, 'Topological crystalline insulators in the SnTe material class', Nat. Com. 3, (2012).
15. J. Wang, N. Wang, 'Electronic properties of SnTe-class topological crystalline insulator materials', *Chin. Phys. B* 25, 11, (2016).
16. Y. Tanaka, T. Sato, Y. Ando, 'Experimental realization of a topological crystalline insulator in SnTe', *Nat. Phys.* 8, 800-803 (2012).
17. P. Dziawa, R. Buczko, T. Story, 'Topological crystalline insulator states in $Pb_{1-x}Sn_xSe$', *Nat. Mat.* 11, 1023-1027 (2012).
18. Su-Yang Xu, Chang Liu, M.Z. Hasan, 'Observation of a topological crystalline insulator phase and topological phase transition in $Pb_{1-x}Sn_xTe$.' *Nat. Com.* 3, 1192 (2012).
19. H. Zhang, S. Gazibegovic, R. Op het Veld, E. Bakkers, L. Kouwenhoven, 'Quantized Majorana Conductance', Extended Data 7, *Nat.* 556, 74-79, (2018).
20. K. Law, P. Lee, T. Ng, *Phys. Rev. Lett.* 103, (2009).
21. Ö. Gül, 'Ballistic Majorana nanowire devices', *TU Delft,* (2017).
22. R. Lutchyn, E. Bakkers, L. Kouwenhoven, P. Krogstrup, C. Marcus, Y. Oreg, 'Realizing Majorana zero modes in superconductor-semiconductor heterostructures.', *Nat Rev Mat* 3, (2018).
23. F. von Oppen, Y. Peng, F. Pientka, 'Topological superconducting phases in one dimension', *Oxford Un. P.*, 2017.
24. A. Das, Y. Ronen, Y. Most, Y. Oreg, M. Heiblum, H. Shtrikman, *Nat. Phys.* 8, (2012).
25. A. Cook, M. Franz, 'Majorana fermions in a topological-insulator nanowire proximity-coupled to an s-wave superconductor', *Phys. Rev. B* 84, 201105, (2011).
26. A. Cook, M. Vazifeh, M. Franz, 'Stability of Majorana fermions in proximity-coupled topological insulator nanowires', *Phys. Rev. B* 86, 155431, (2012).

27. L. Fu, E. Berg, 'Odd-Parity Topological Superconductors: Theory and Application to $Cu_xBi_2Se_3$', *Phys. Rev. Lett.* 105, 097001, (2010).
28. S. Mi, M. Wimmer, C. Beenakker, 'Proposal for the detection and braiding of Majorana fermions in a quantum spin Hall insulator', *Phys. Rev. B* 87, 241405, (2013).
29. E. Bocquillon, P. Leubner, L. Molenkamp, 'Gapless Andreev bound states in the quantum spin Hall insulator HgTe.' *Nat. Nanotechnology* 12, 137-143, (2017).
30. L. Fu, C. Kane, 'Josephson current and noise at a superconductor/quantum-spin-Hall-insulator/superconductor junction', *Phys. Rev. B* 79, 161408, (2009).
31. A. Cho, J. Arthur, 'Molecular Beam Epitaxy. Progress in Solid-State Chemistry', 10, *New York: Pergamon*, part 3, p. 157-191, (1975).
32. S. Franchi, 'Molecular beam epitaxy: fundamentals, historical background and future prospects', *Elsevier Science*, (2013).
33. G. Springholz, 'Molecular beam epitaxy of IV-VI semiconductors: multilayers, quantum dots and device applications', *Elsevier Science*, (2013).
34. H. Clemens, E. Fantner, 'Growth and characterization of PbTe epitaxial films grown by hot-wall epitaxy', *J. Crystal Growth*, 66, 251, (1984).
35. A. Ueta, G. Springholz, G. Bauer, *J. Crystal Growth*, 175/176, 1022, (1997).
36. B. Tranta, H. Clemens, *Lecture notes in physics*, 301, 281, (1988).
37. G. Springholz, A. Ueta, N. Frank, G. Bauer, *Applied Physics Letters*, 69, 2824, (1996).
38. K. Wiesauer, G. SpringHolz, *Applied Surf Sci*, 188, 49, (2002).
39. E. Abramoff, S. Ferreira, *J. Cryst Growth*, 96, 637, (1989).
40. M. Ghasemi, J. Johansson, 'Phase diagram for understanding gold-seeded growth of GaAs and InAs nanowires', *J. Phys. D: Appl. Phys.* 50, (2017).
41. G. Bootsma, H. Gassen, 'A quantitative study on the growth of silicon whiskers from silane and germanium whiskers from germane', *J. Cryst. Growth* 10, 223-34, (1971).
42. B. Legendre, C. Souleau, J. Rouland, 'Étude des diagrammes d'équilibre de phase des lignes $AuTe_2$-SnTe et AuSn-SnTe du système ternaire Au-Sn-Te', *Compt. rend.,* 275, C, 805, (1972).
43. J. Ciulik, M. Notis, 'The Au-Sn phase diagram', *J.Alloys and Compd.* 191, 71-78, (1993).
44. H. Okamoto, T.B. Massalski, 'The Au-Te (Gold-Tellurium) System', *Bulletin of Alloy Phase Diagrams*, *Vol. 5 No. 2,* (1984).
45. P.B. Littlewoord, 'Band Structure of SnTe Studied by Photoemission Spectroscopy', *Phys. Rev. Lett.* 105, (2010).
46. K. Lischka, 'Deep level defects in narrow gap semiconductors', *Phys. Status Solidi (b)* 133, 17, (1986).
47. J. Richard Burke, R. Allgaier, B. Houston, J. Babiskin, P. Siebenmann, 'Shubnikov-de Haas Effect in SnTe, *Phys. Rev. Lett.* 14, 360, (1965).
48. R.S. Allgaier, W. W. Scanlon, 'Mobility of Electrons and Holes in PbS, PbSe, and PbTe between Room Temperature and 4.2 °K', *Phys. Rev* 111, 1029 (1958).
49. I. Kasai, D.W. Bassett, J. Hornung, 'PbTe and $Pb_{0.8}Sn_{0.2}Te$ epitaxial films on cleaved BaF_2 substrates prepared by a modified hot-wall technique.
50. E. Abramof, S. Ferreira, 'Electrical properties of $\mathrm{Pb}_{1-x}\mathrm{Sn}_x\mathrm{Te}$ layers with $0 \leq x \leq 1$ grown by molecular beam epixtaxy, *J. of Applied Physics* 82, 2405, (1997).
51. N. Wang, D. West, J. Liu, Q. Yan, B. Gu, S. Zhang, W. Duan, *Phys. Rev. B* 89, (2014).
52.G. Pratt, *J Nonmetals,* 1, 103, (1973).
53. N. Parada, *Phys Rev B*, 3, 2042, (1972).

54. H. Heinrich, W. Zawadski, ‘Narrow gap semiconductors: physics and applications.’, *Berlin Springer Verlag*, 407, (1980).
55. B. Bradlyn, B. Bernevig, ‘Topological quantum chemistry’, *Nature* 57, 298-305, (2017).
56. H. Po, A. Vishwanath, H. Watanabe, ‘Symmetry-based indicators of band topology in 230 space groups’, *Nat. Communications* 8, 50, (2017).
57. G. Springholz, ‘Molecular beam epitaxy of IV-VI semiconductors: multilayers, quantum dots and device applications’, *Elsevier Science*, (2013).
58. D. Khokhlov, ‘Lead Chalcogenides: Physics and Applications’, *CRC Press,* (2002).
59. R. Colin, J. Drowart, *J Chem Phys*, 37, 1120, (1962).
60. M. Safdar, ‘Crystal Shape Engineering of Topological Crystalline Insulator SnTe Microcrystals and Nanowires with Huge Thermal Activation Energy Gap’, *Cryst. Growth Des.* 14, 2502-2509, (2014).
61. M. Safdar, ‘Weak antilocalization effect of topological crystalline insulaor $Pb_{1-x}Sn_xTe$ nanowires with tunable composition and distinc {100} facets’, *Nano Lett.* 15, pp 2485-2490, (2015).
62. Q. Wang, ‘Oriented Growth of $Pb_{1-x}Sn_xTe$ Nanowire Arrays for Integration of Flexible Infrared Detectors’, *Advanced Materials* 18, (2016).
63. E. Xu, ‘Enhanced thermoelectric properties of topological crystalline insulator PbSnTe nanowires grown by vapor transport’, *Nano Research* 9, 820-830, (2016).
64. E. Xu, ‘Diameter dependent thermoelectric properties of individual SnTe nanowires’, *Nanoscale* 7, (2015).

3. Methods

In this Chapter first the tight-binding approach is discussed that is used for the modelling of the normal and (induced) superconductive states of SnTe (section 3.1). In section 3.2 the technical aspects of the MBE setup and substrate processing are discussed.

3.1 Tight-binding approach

The properties of SnTe material such as band structure, (surface) density of states and conductance were calculated for different geometries using the tight binding approximation. In the tight binding approximation electrons are localized on the atoms and the overlapping of the atomic orbitals is studied. The eigenstate of one electron in the periodic lattice is approximated by a linear combination of atomic orbitals.
The tight binding Hamiltonian is used in simulations executed using the quantum transport Python package Kwant[1]. Since Kwant can be used for any lattice and dimension, 1D, 2D and 3D periodic lattices are treated. Kwant takes the hopping and onsite terms of a tight binding model, which are defined for each crystal site, and constructs a Hamiltonian for the ensemble of lattice sites.

All calculations are done using a tight binding Hamiltonian taken from C.S. Lent et al[2]. This tight binding model Hamiltonian contains onsite and hopping terms for the s, p and d orbitals of the cation (Sn) and anion (Te) of the system. The model can also be used to investigate other materials such as PbTe, GeTe, PbSe and PbS. Moreover using the virtual crystal approximation, the band structure of alloys such as $Pb_{1-x}Sn_xTe$ can be calculated. The model used here is also used in literature for most predictions on SnTe, such as for the prediction of the quantum spin Hall effect on its (111) surface[6]. A simpler 6 orbital model[3,4] is used later in section 4.2. This model predicts the same number of Dirac cones for the investigated geometries, however shows qualitatively different band structures. Details of the 18 orbital model are further discussed below and section 4.1.

Bulk dispersion

The SnTe dispersion calculations in this research were performed using a nearest-neighbor 18 orbital sp^3d^5 tight-binding Hamiltonian acquired from C.S. Lent et al[2]. The parameters of the model of C.S. Lent are obtained by fitting the eigenvalues of Lent's tight binding Hamiltonian to the energy bands published by F. Herman et al[4]. Both bulk dispersions of C.S. Lent and F. Herman are shown in Fig. 3.1.

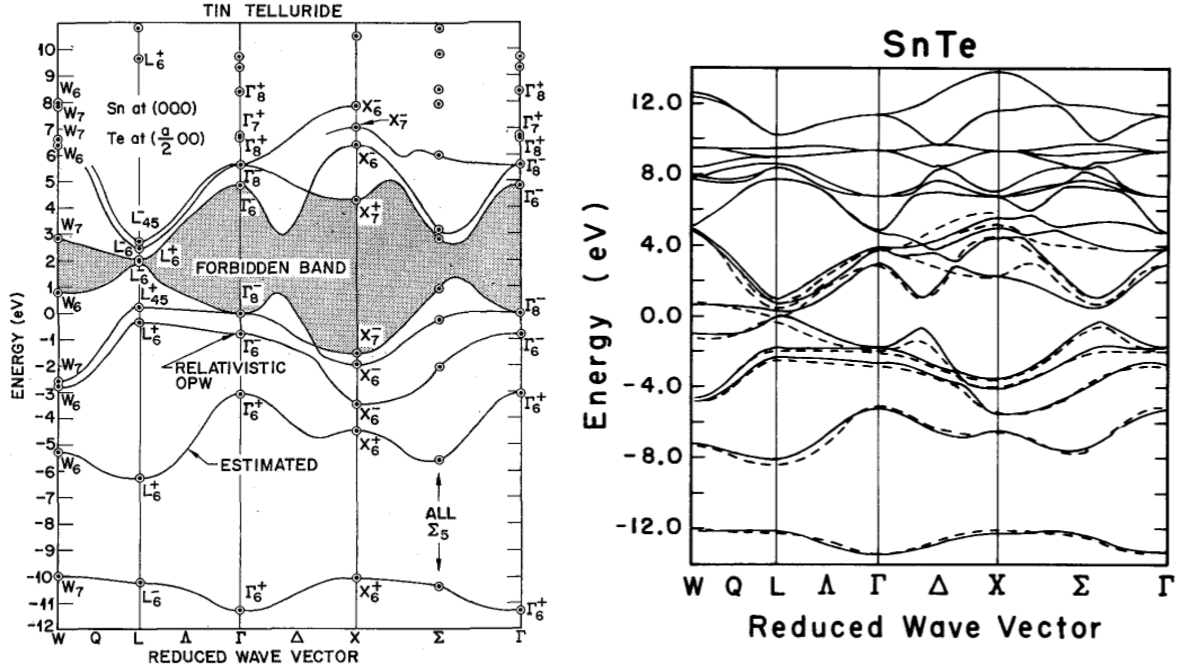

Fig. 3.1: a) Energy band structure of SnTe calculated by Herman et al.[5] b) Energy band structure of SnTe of calculated by Lent at al.[2] using a tight-binding model. Dashed is the band structure of Herman et al.

To calculate the SnTe 3D bulk dispersion a unit cell is chosen with one Sn and one Te atom, which are placed in a rocksalt structure on a cubic lattice with length 1 between the Sn and Te atom. Periodic boundary conditions are then applied in the $(1,1,0)$, $(1,-1,0)$ and $(1,0,1)$ directions. These directions are non-orthogonal, but if orthogonal translation directions are used then the unit cell must contain 4 instead of 2 atoms at least, making calculations more computationally expensive.
Next the translation directions and the tight binding Hamiltonian are passed to the Kwant Python package. Using the new (3D) $\vec{k}$-dependent Hamiltonian that Kwant then generates the energy dispersion can be acquired by calculating the eigenvalues of this Hamiltonian for specific $\vec{k}$-points.
Since the SnTe primitive lattice is a face-centered cubic FCC lattice, the high symmetry $\vec{k}$-points between which the energy bands are calculated are defined with respect to the BCC reciprocal lattice given by

$$\vec{k} = u\overrightarrow{b_1} + v\overrightarrow{b_2} + w\overrightarrow{b_3}, \qquad (3.1)$$

where $\overrightarrow{b_1}$, $\overrightarrow{b_2}$ and $\overrightarrow{b_3}$ are the reciprocal primitive lattice vectors in the orthogonal basis. The high symmetry points (u, v, w) are $(0{,}0{,}0)$ and $(1{,}1{,}1)$ for Γ, $\left(\frac{1}{2}, \frac{1}{2}, \frac{1}{2}\right)$ for L, $\left(0, \frac{1}{2}, \frac{1}{2}\right)$ for X and $\left(\frac{1}{4}, \frac{3}{4}, \frac{1}{2}\right)$ for W. To get the actual $\vec{k}$-points for our model, which has non-orthogonal real lattice vectors, the original orthogonal real lattice vectors of an FCC lattice have to be transformed to the new non-orthogonal real vectors. From there the expression for $\overrightarrow{b_1}$, $\overrightarrow{b_2}$ and $\overrightarrow{b_3}$ in the non-orthogonal lattice are obtained so that the $\vec{k}$-points of the high symmetry points in the non-orthogonal lattice can be acquired.

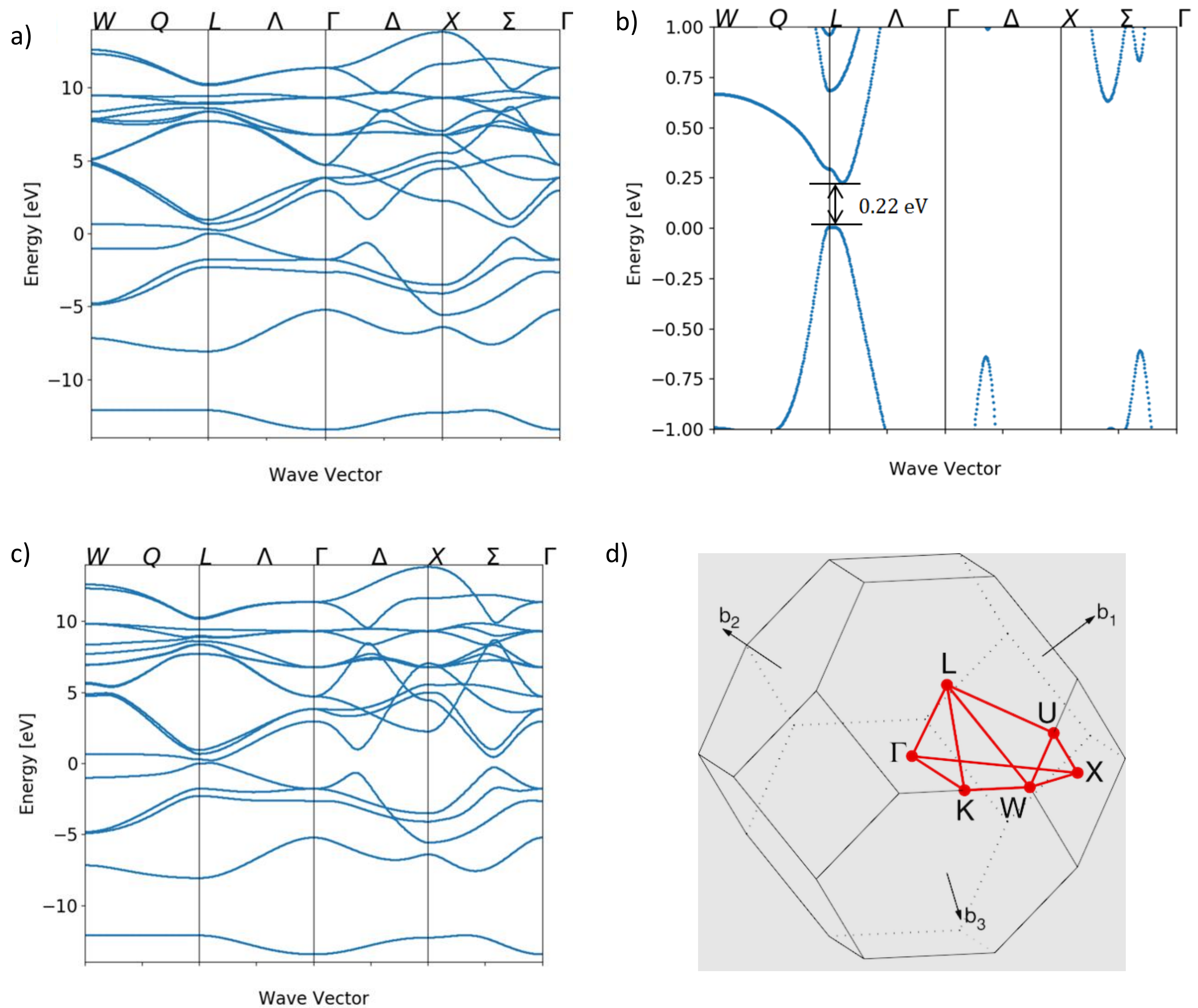

Fig. 3.2: a) Calculated SnTe bulk dispersion with the parameters of Lent[2]. b) Zoomed representation of Fig. 3.2a) showing the bandgap. c) Calculated SnTe bulk dispersion with the parameters of Safaei[7]showing not much qualitative change with respect to 3.2a). d) The 3D Brillouin zone of the FCC SnTe lattice. Figure d) is reproduced from ref. 12.

The band structures of Fig. 3.1b) and Fig. 3.2a) are calculated on the same $\vec{k}$-points, same band parameters and the same model. One discrepancy seems to be that along the Δ and Σ lines there are some points were the bands are crossing in Fig. 3.2a), while there is a small gap at those $\vec{k}$-points in Fig. 3.1b). Fig. 3.2b) shows a zoomed graph of Fig. 3.2a) where the calculated band gap of 0.221 eV is shown, which agrees reasonably well with the value of 0.18 eV found in literature[6]. In Fig. 3.2c)

shows the bulk dispersion using the parameters of Safaei[7]. The bang gap is 0.188 eV. For the simulations in section 4.1 the tight-binding parameters corresponding to Fig. 3.2c) published by Safaei[7] are used. These parameters use the correct signs for the parameters as defined by Slater and Koster[8]. As can be seen by comparing Fig. 3.2c) with Fig. 3.2a) this change of parameters doesn't change the band structure qualitatively, especially not near the Fermi level.

3.2 Molecular beam epitaxy setup and sample preparation

In this section all technical aspects of the MBE setup and substrate processing are discussed. Firstly in section 3.2.1 practical considerations are discussed such as the time frame in which could be grown and growth strategy. Then in section 3.2.2 substrate processing is discussed. Next the realization of UHV by different pumping methods is discussed in section 3.2.3. Then the reliable method of temperature measurement called BandiT is discussed in section 3.2.4. In section 3.2.5 the effusion flux calibration is discussed, as well as a discussion on substrate temperatures.

3.2.1 Practical considerations

Growth time in this research was limited since the IV-VI MBE chamber is new in our group and renovations were still ongoing at the start of the research. Therefore in the first half of the project, while the modelling of this research was done, several modifications were done to the machine. For example effusion cells were loaded and mounted and electronics such as effusion cell and substrate temperature controllers were installed. Moreover compartments of the system were baked (heating from the outside) and pumped to attain the UHV conditions. Also the system was down for some time due to maintenance on the substrate manipulator. Due to all of this the growth days were limited to about 40 growth days.

Since to our knowledge no literature of SnTe MBE is available, different parts of the growth parameter space were discovered. Most notably growth runs with substrate temperatures between $T_B = 190$ °C and $T_B = 450$ °C were done. Additionally differently processed substrates were loaded each growth run (about 5 to 10 samples per run).

In the 40 days of growth time, 51 growth runs were performed, since only 1 to 2 growth runs per day could be done. This is first of all because a lot of time is consumed by substrate processing, which needs to be done daily before loading the MBE machine. Moreover that preparing the MBE machine involves loading the sample, which involves venting and pumping down the loadlock, degassing/baking the substrates, heating the effusion cells, ramping up and stabilizing the substrate temperature etc.

3.2.2 Substrate processing

Several different substrates were mounted on the substrate holder during the different growth runs. Some of the substrates used are processed with a silicon nitride (SiN_x) mask with holes. The strategy here is to eliminate parasitic layer growth on the substrate and to increase the incoming amount of molecules arriving at the gold particles in the holes. Holes are patterned into the mask in which the nanowires can selectively grow. Holes have sizes varying from 8 to 50 nm and distances between the holes range from 250 nm to 4 μm. The fabrication procedure is illustrated in Fig. 3.3 below. First (1) (10 nm) SiN_x is deposited in a plasma-enhanced chemical vapor deposition (PECVD) reactor on the substrate, e.g. Ge(110) with 2 inch diameter. Then (2) a CSAR resist is spin-coated on the SiN_x mask, which is a special resist that is compatible with reactive ion etching (RIE). Next a set of holes with different sizes and pitches (mutual distance) is patterned into the CSAR resist using electron-beam lithography (EBL). Fig. 3.4 shows the EBL design with all the different hole-sizes and pitches. Each array is exposed to a different dose of electrons in the EBL to make sure that all the SiN_x will be removed from the mask. This design is repeated about 700 times over the wafer, where over each 6

copies of the design the EBL dose is varied. After developing (3) the by EBL exposed resist the wafer is put in the (4) nitride reactive ion etcher (RIE). Using pure CHF_3 the etching rate is slow enough to etch away the thin 10 nm mask and not to damage the substrate and resist much. This step does deposit long teflon polymer chains, which could have a negative effect on the growth. This could be countered by using a CHF_3 + O_2 recipe. However this would damage the resist, making the lift-off process worse, and results in larger hole sizes than intended. Next the 8 nm layer of gold (5) is deposited in the electron beam evaporator filling only the etched holes with gold. Finally the remaining resist with superfluous gold on top is removed in a lift-off process using the chemical PRS.

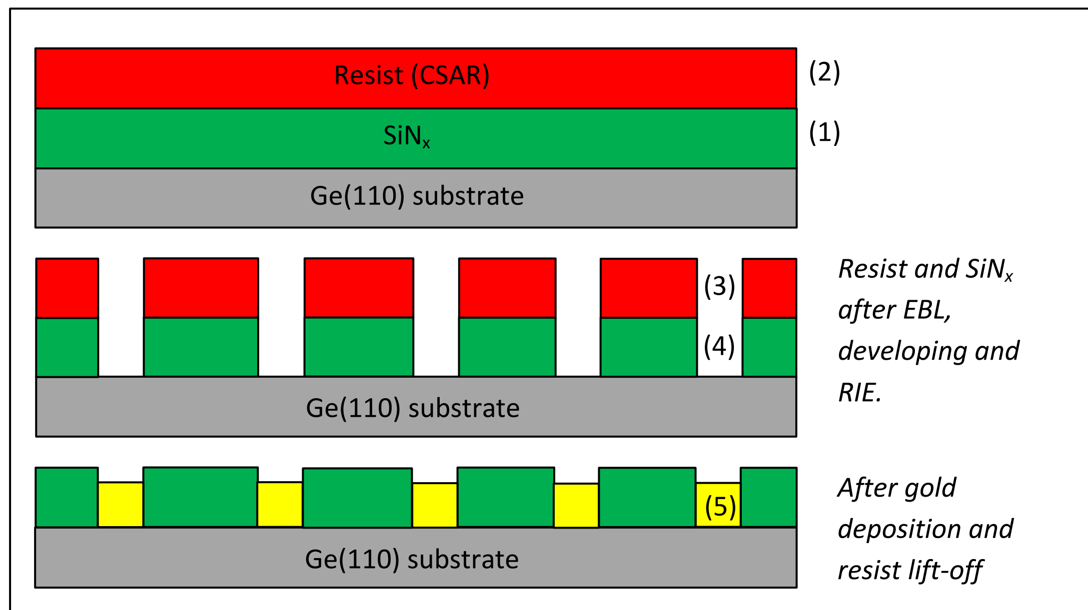

Fig. 3.3: Lithographic patterning using a SiN_x mask and EBL for nanowire growth.

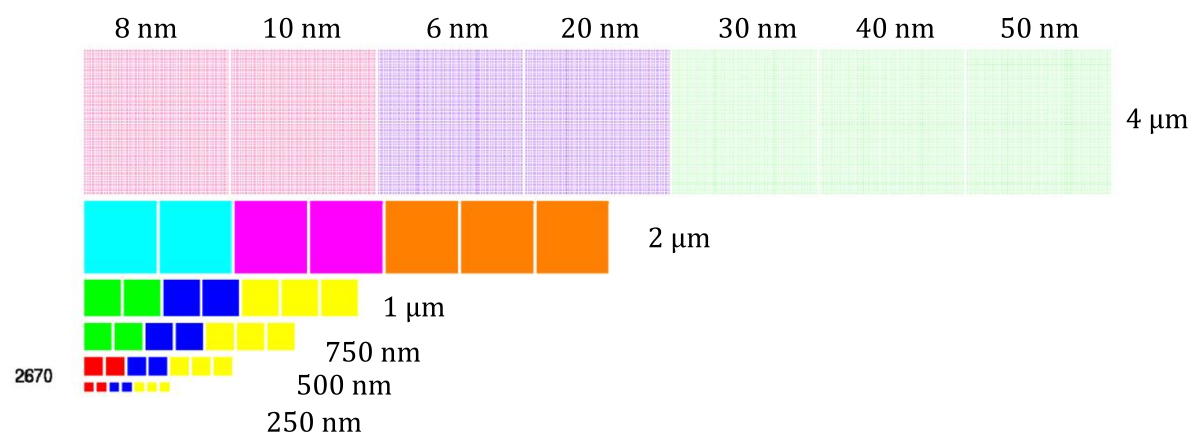

Fig. 3.4: Design of the EBL patterning. Each array has a certain hole-size and pitch. The hole-size is varied in the horizontal direction, while pitch is varied in the vertical direction.

Fig. 3.5 shows results after substrate processing of a GaAs substrate with a patterned SiN_x mask for the smallest hole sizes of 8 nm and a 250 nm distance between the holes. In these scanning electron microscopy (SEM) pictures the same array of holes is shown for different EBL doses,

however while in b) all holes are opens, in a) more than half of the holes is not. This means that in the EBL the same pattern is exposed with electrons, but each hole in the Fig. 3.5b) was exposed to more electrons than in Fig. 3.5a). The consequence is that some holes in Fig. 3.5a) are under-exposed, due to the low dose of electrons, thereby not opening all holes.

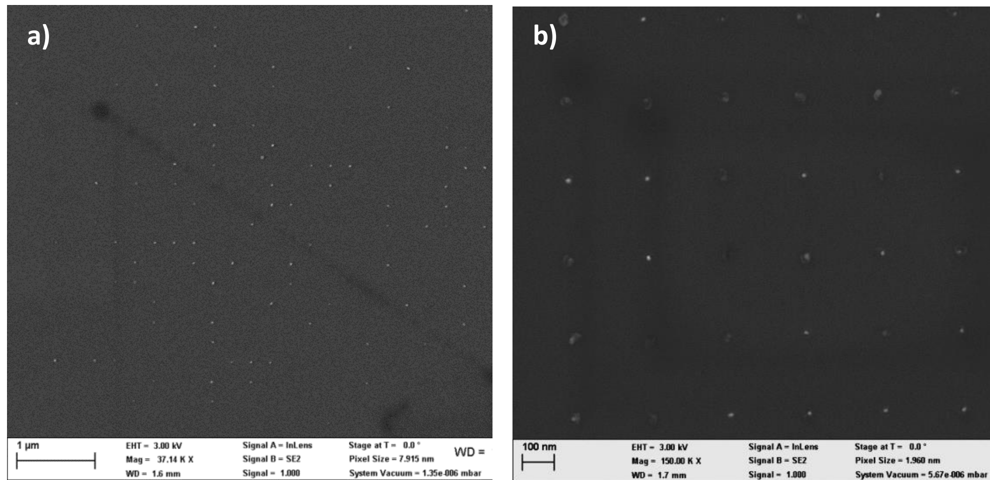

Fig. 3.5: SEM images of a EBL dose test of the patterned SiN_x mask with Au particles on a GaAs substrate. A hole-array is shown with a (designed) 8 nm hole-size and 250 nm distance between the holes. In (a) the wafer is exposed to an EBL dose of 2010, while in (b) the wafer is exposed to an EBL dose of 3140. Magnifications are (a) 37 KX and (b) 150 KX.

Fig. 3.6a) shows a close-up SEM of a GaAs substrate with patterned SiN_x mask for a dose of 2850, a hole-size of 50 nm and a distance between the holes of 250 nm. The holes seem to be quite clean except for some small white dots in and around the holes which could indicate some SiN_x residues. The dark rim around the high contrast gold particle presumably indicates that the SiN_x layer is fully etched way in the hole, exposing the low contrast GaAs substrate. In Fig. 3.6b) the a similar SEM is shown for a Ge substrate. The same SiN_x residues are found and also the dark rim is visible. A lot of dirt can be seen though on or under the SiN_x which could imply that the Ge substrate was not as clean of oxides as the GaAs substrate was before depositing the SiN_x layer.

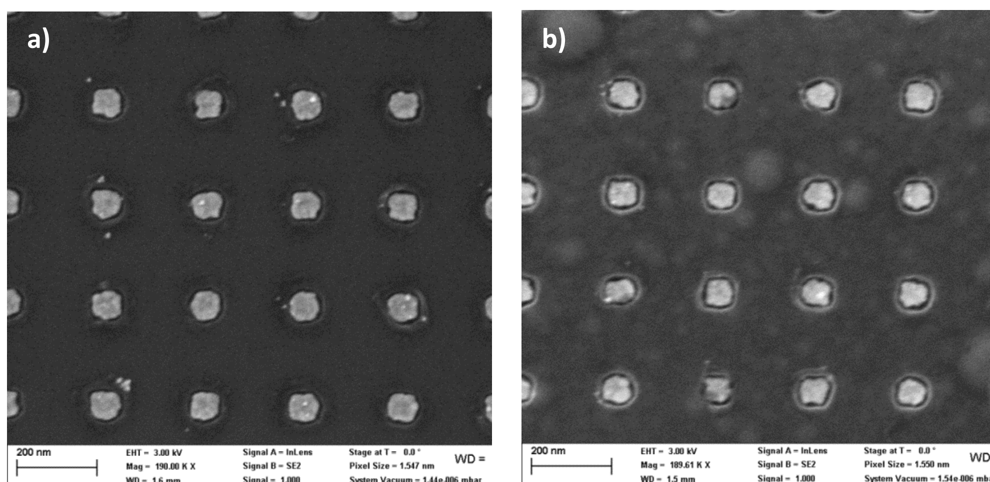

Fig. 3.6: SEM images of (a) GaAs substrate and (b) Ge substrate with a patterned SiN_x mask and Au particles. Magnifications are (a) 190 KX and (b) 190 KX.

At some areas of the substrate larger amounts of gold are present, which will be important for the growth in section 4.2.2. Fig. 3.7a) and b) show the EBL dose markers. These are large areas (feature size $\sim 5\ \mu\mathrm{m}$) were the SiN_x is etched away, but is probably under-etched. Besides that, within a marker but between the numbers also gold is deposited. This is due a collapse of the CSAR resist with Au on top of it during lift-off. This collapse during lift-off is also found at the hole arrays for $50\ \mathrm{nm}$ hole sizes with 250 mutual distance, as shown in Fig. 3.7c). The result of these processes is the deposition of large amounts of gold. The morphology of this gold is much rougher than the gold in a hole, as can be seen in Fig. 3.7b) for a close-up of a dose number.

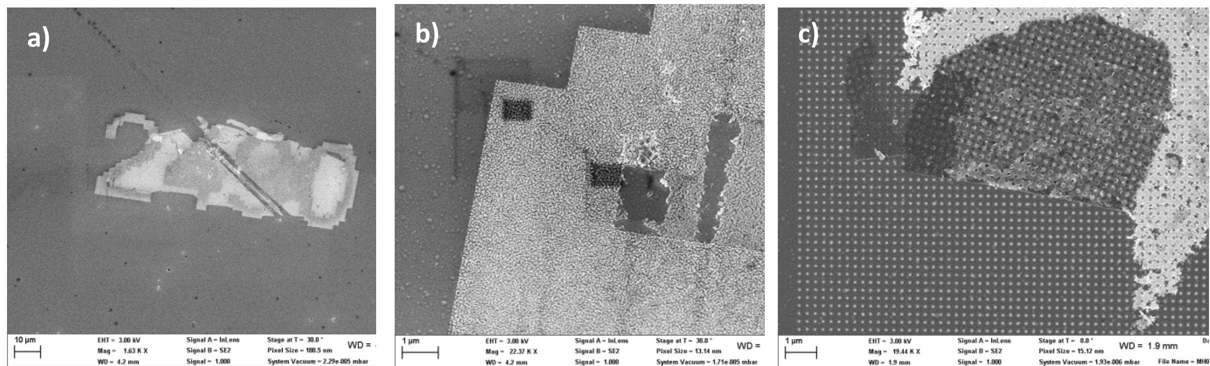

Fig. 3.7: SEM images of a Ge substrate with a patterned SiN_x mask showing large amounts of gold on EBL dose-markers (a-b) and patterns with bad-liftoff (c). The black areas in Fig. 6.4b) are due to carbon deposition by the SEM. Magnifications are (a) 2 KX, (b) 22 KX and (c) 19 KX.

Another approached used is buffered hydrofluoric acid (BHF) gradient etching. Here a gradient in the SiN_x mask is fabricated with a thickness ranging for 0 to 25 nm. Since the BHF does not etch the mask with exactly an equal rate, in the thin parts of the SiN_x mask a rough texture in the SiN_x is achieved. Here the substrate is only exposed at some place.

Just before growth all substrates (except for some of the last runs and the substrates with stems) were cleaned and oxidized in a O_2 plasma. To remove oxides finally the GaAs substrates were dipped in ammonia 10:1 ($\mathrm{NH_3}$) and ultra-pure water (UPW), while Si substrates were in some cases deoxidized in BHF 10:1 and UPW prior to growth.

The substrates that are tested are GaAs (001), Ge(110), Si (001) and Si (111) with and without gold catalysts. The gold catalysts were evaporated in an electron beam evaporator or were deposited on the substrate by spin coating a $2\ \mathrm{nm}$ gold colloid solution. Also nanowire stems were used as substrates, such as catalyst free and gold catalyzed InAs, InP, InSb, GaAs and Ge nanowire stems.

Finally after the substrate processing steps several samples are mounted onto an molybdenum sample holder by gluing the samples with indium at about 200 °C. Next the samples are degassed at 250 °C for 2 hours to remove all contaminants such as water.

3.2.3 UHV Pumping

Reaching UHV conditions is very important in the growth process so that atoms can reach the target substrate and so that the impingement of air or other gas molecules at the target surface and therefore contamination is minimized. When all cell shutters and cracker valves are closed, the system has a pressure of about $2 \cdot 10^{-10}$ mbar. This is achieved by a combination of rough, turbo, cryo- and ion pumps, where the last two are essential. The rough pumps used can reach pressure of $5 \cdot 10^{-3}$ to $5 \cdot 10^{-4}$ mbar. The turbo pumps used can reach pressures of $1 \cdot 10^{-8}$ mbar without baking the chamber, while pressures of $1 \cdot 10^{-9}$ mbar can be obtained after baking and engaging the ion pump. Baking the chamber strips water from the chamber walls so that the pumps can reach lower pressures. The last order of magnitude is delivered mostly by the ion and cryo pumps.

The ion pumps in our system (MECA 2000) are a combination of titanium sublimation pumps and getter ion pumps of the type diode pump[10]. The ion pumps cannot pump noble gasses effectively. The titanium that is sublimated onto the walls of the chamber binds chemically to the gasses to be pumped. The ion getter pump, shown in Fig. 3.8a) below, is composed of an anode made of cylindrical cells in a honeycomb structure and two cathodes made of flat plates. Perpendicular to the plates is a $0.1 - 0.2$ T magnetic field and between the anode $(+)$ and cathode $(-)$ a voltage of 4 to 6 kv is applied. In the cells gasses are ionized and the electrons are trapped in the electromagnetic field thereby ionizing other gas molecules. The ions are then bombarded into the cathodes.

The cryopumps in the system (CTI 8&10) have 80 K and 15 K cooling parts[11] in them and a 80 K radiation shield to prevent warming up[10]. These parts are cooled by a helium refrigerator in which helium gas is cooled down in a closed circuit via adiabatic expansion. Under the low temperature the mutual binding energy of gas molecules condensates them. In first approximation the pressure in the system is determined by the vapor pressures of the gasses at the temperature of the cooling arrays. Fig. 3.8b) shows the vapor pressure curves for gasses typically found in a process chamber. The 80 K condensing array condenses water and hydrocarbon vapors. As can be concluded by Fig. 3.8b) the 15 K cooling array condenses nitrogen, oxygen and argon. However helium, hydrogen and neon are not effectively condensed, because their vapor pressure at 15 K is too high. This is no problem for helium and neon, as they don't naturally arise in the vacuum system. However the hydrogen in the residual gas is trapped by the layers of activated carbon that is mounted on the 15 K cooling array.

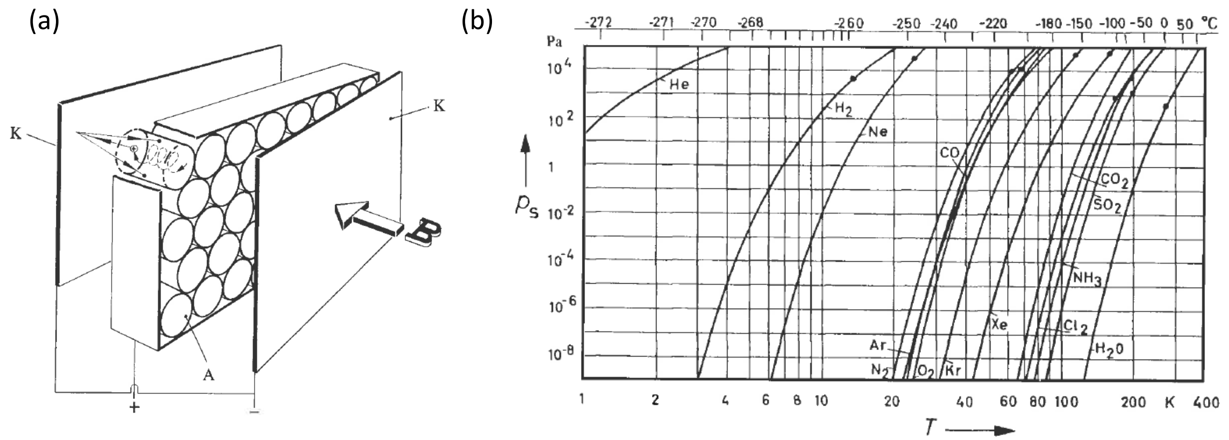

Fig. 3.8: (a) Schematic of a getter ion pump, with A the anode cylinders, K the titanium cathodes and B the magnetic field[10]*. (b) Vapor pressure curves for some gasses.*[10]

3.2.4 BandiT temperature measurements

In our MBE system the substrate temperature is measured by a combination of a thermal couple in the neighborhood of the substrate and a BandiT[12] temperature detector. The BandiT temperature is a very reliable read-out of the real temperature. The BandiT system is composed of a black body light source directed at a GaAs dummy sample and a detector directed at it under a different angle. From the slope of the band edge in the absorption spectrum the temperature can be calculated. An example of a BandiT spectrum, made after depostion of SnTe, is shown in Fig. 3.9a). For an empty substrate before growth the intensity would be much larger (up to $\sim 6000 - 7000$), however due to the deposition of metals or narrow-gap semiconductors like SnTe the BandiT signal is reduced. Therefore the intensity of the BandiT signal is a way to estimate the amount of deposited SnTe.

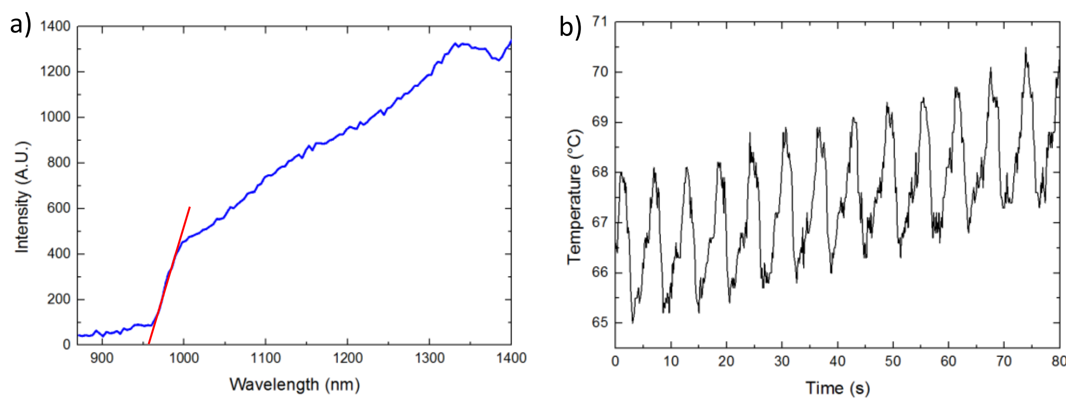

Fig. 3.9: (a) BandiT spectrum after SnTe deposition on GaAs (001) *(blue) with band edge slope fitting (red). (b) Temperature readout showing temperature oscillations of about* 1.5 °C during rampup.

Before growth the substrate is heated to a certain temperature, which is called the rampup stage. The samples rotates so that incoming material is divided evenly over the substrate. Fig. 3.9b) shows that the rotation causes an oscillation in the BandiT signal with an amplitude of about 1.5 °C. The oscillation is there because in some point in the rotation the BandiT detector does not receive light

from the GaAs dummy samples but of different materials on the substrate holder. The oscillations can be reduced by correctly aligning the BandiT detector on the dummy samples. Alignment of the BandiT detector can be done by changing the tilt of the substrate holder or by directly changing the tilt of the BandiT detector.

In Fig. 3.10a) a typical BandiT temperature measurement is showed. From $t = 0$ to $t = 4230$ s the substrate temperature is ramped up. The temperature has to stabilize to the growth temperature which at low substrate temperatures can take a long time. At $t = 4230$ s the effusion shutters (Sn and Te) are opened which increases the temperature on the substrate by about 2 ℃ (Fig. 3.10b)). After about 7.8 min of deposition the BandiT read-out breaks down due to SnTe deposits. At around $t = 2500$ s there is a gap and a sudden increase in BandiT temperature. This is the result of closing the shutter on the BandiT detector and stopping the substrate rotation, so that the substrate holder can be repositioned in the manipulator. The manipulator namely has 3 rotations at which the substrate holder can be attached. It was found that the heating does not have the same efficiency for all 3 substrate holder positions. This is further investigated in Fig. 3.11. Here the temperature is first ramped up until it stabilizes. The thermal couple temperature was constantly 410 ℃, however different BandiT temperatures are found four the 3 positions, namely 207 ℃, 170 ℃ and 202 ℃. This means that for some positions the heating has a different efficiency (probably by heat conduction) than in other positions. Fig. 3.11 b) shows the substrate holder inside the carriage that transports the substrate to the degas heating station. The mounting on the manipulator is similar, as the same 3 metal pins on the substrate holder are used.

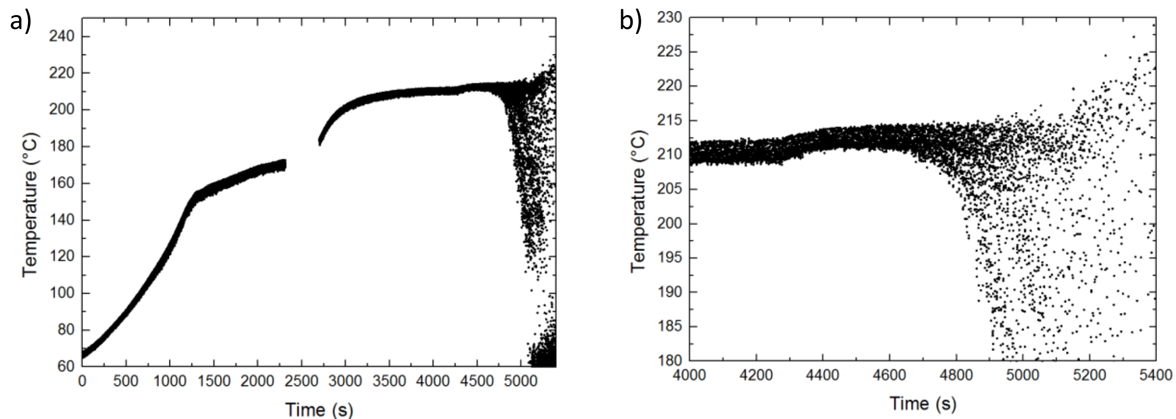

Fig. 3.10: (a) BandiT signal during substrate rampup and growth, the substrate position was changed to match the required temperature. Growth starts at $t = 4230$ s, which results in a temperature rise of about 2 ℃. After 7.8 minutes the BandiT read-out breaks down due to SnTe deposits.

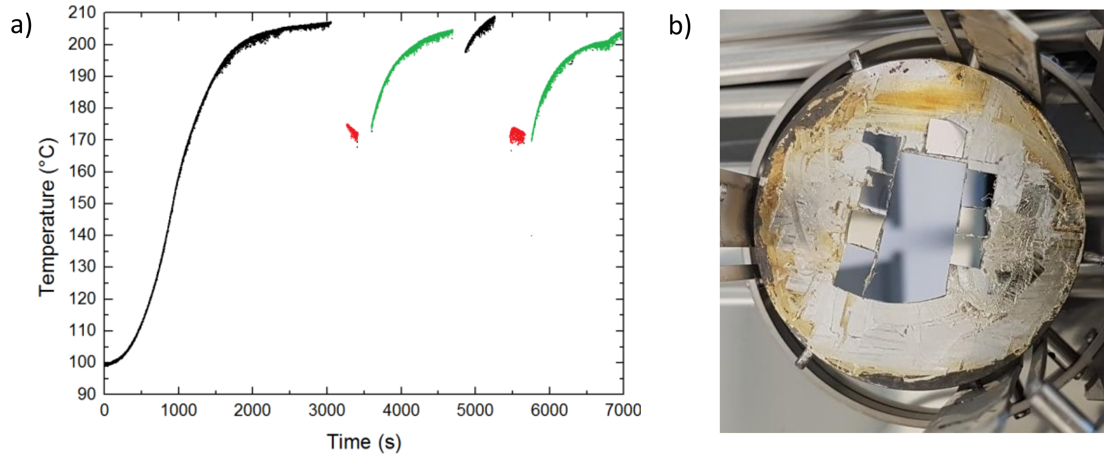

Fig. 3.11: (a) BandiT signal during substrate rampup, after temperature stabilization at 207 °C the substrate holder (moly) is repositioned on its 3 different positions. Black represents position 1, red is position 2 and green is position 3. (b) Substrates on a substrate holder showing that the holder can be attached to a manipulator in 3 different ways.

3.2.5 Effusion flux calibration and substrate temperature

The material flux generated by an effusion cell (standard cell or cracker) depends on details of the MBE system, such as its geometry, the vapor pressure and temperature of the effused material, where the latter two are related. The beam equivalent flux F in mbar can be estimated by

$$F = K \cdot p(T), \tag{5.1}$$

where K is the geometrical constant and $p(T)$ is the vapor pressure of the material as a function of temperature T. K is fixed for the standard Sn effusion cell, but for the Te cracker cell it depends on the valve opening. Namely the valve of the Te cracker can be openinged and closed by turning the valve open and closed. Our Te cracker is operated by hand so that the valve opening can be continuously varied from completely closed (0 turns) to completely open (16 turns).
The vapor pressure is approximated by

$$p(T) = 10^{\left(A - \frac{B}{T}\right)}, \tag{5.2}$$

where A and B are fitting parameters found in literature for Sn[13] and Te[14].
The Sn and Te fluxes are calibrated by inserting a beam flux monitor in the effusion beams, which measures the beam equivalent pressure (BEP). The beam flux monitor is an ionization flux gauge[15] on a movable positioning system that allows to measure the beam equivalent pressure of a molecular beam near the substrate. The beam flux monitor broke down in the beginning of the experiments, however the calibration data was used to establish the desired material fluxes.
The calibration data is plotted in Fig. 3.12 for Sn as a function of effusion cell temperature and for Te as a function of valve opening expressed in number of turns. Since the Sn cell is at much higher temperature than the Te cell it reacts much faster to temperature changes then the Te cell. Therefore the Te flux is generally not controlled by changing the base temperature, but by changing the valve opening. The fit for the Sn flux is made by inserting eq. 5.2 into eq. 5.3 and changing the geometrical constant K until good correspondence with the data points is achieved. The fitting curve follows the data points well, except for low temperatures. During the calibration the chamber was not pumped by the cryopump yet and the background pressure was $0.030 \cdot 10^{-7}$ Torr. Therefore the low Sn fluxes generated at low effusion temperatures are not considerably larger than the

background and measured fluxes are higher than expected based on the fitting curve. The black curve through the data points in Fig. 3.12.b) is made by interpolation. The Te flux curves for different temperatures are acquired by multiplying the interpolation curve with a factor $p(T_2)/p(T_1)$. From Fig. 3.12b) it becomes clear that for a high valve opening ~ 14 turns the Te flux is the least sensitive with respect to the valve opening. Therefore, to decrease uncertainties in the Te flux, the valve is mostly set almost completely open during growth at a valve opening of 14 turns.

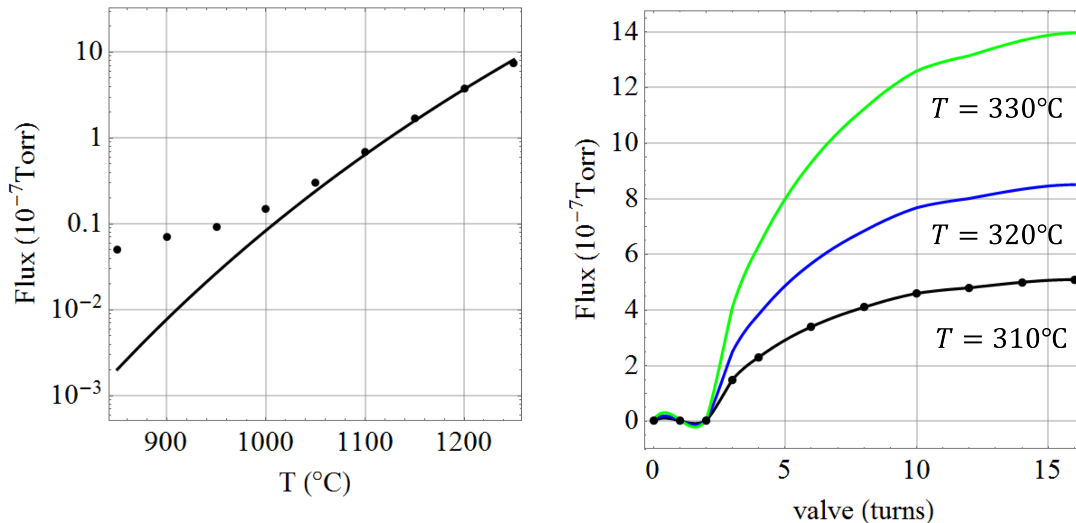

Fig. 3.12: Beam flux monitor data and calibration curves of (a) Sn as a function of temperature and (b) Te as a function of valve opening.

Another important growth parameter in IV-VI material growth, besides the effusion cell temperatures, is the substrate temperature. The growth rate and composition of the epitaxial layers should be determined by the beam fluxes and not by the substrate temperature. Therefore the substrate temperature must be low enough such that the reevaporation rate of the growth-determining species is much lower than its impingement rate. The reevaporation rate of materials from the surface into the UHV environment is given by[16]

$$J_{reevap} = \alpha_v \frac{p}{\sqrt{2\pi m k_B T}}, \tag{5.3}$$

where m is the mass of the molecule, k_B is the Boltzmann constant, T is the temperature and p is the vapor pressure. α_v is the evaporation coefficient, which is around 0.3 to 0.5 for smooth low index surfaces with strongly bound surface atoms and is close to one for rough high index surfaces or polycrystalline materials.

The evaporation rates for IV-VI materials calculated from vapor pressure data, assuming an evaporation coefficient $\alpha_v = 0.5$, is shown in Fig. 3.13. As can be seen the reevaporation rates of the PbX and SnX compounds as well as of Pb are quite comparable and are exceeding 1 ML/s at around 440 °C. Therefore when the fluxes are set so that 1 ML/s arrives at the substrate, no layer deposition occurs at temperatures above 440 °C. For the same fluxes, to attain the condition that the epitaxial growth rates are independent of substrate temperature, the reevaporation rates should be well below 0.01 ML/s, as indicated by the horizontal line in Fig. 3.13, which is fulfilled below about 380 °C for SnTe. Based on these considerations the MBE process window in Fig. 3.13 shows the range of substrate temperatures in which IV-VI materials can be grown. Note also that for substrate temperatures above about 200 °C, the reevaporation rate of Te is high. The reevaporation rate of

Sn, which is not shown in Fig. 3.13, is negligible ($< 10^{-4}$) for temperatures lower than about 700 ℃. Therefore at temperatures above 200 ℃ all Te that is not incorporated into the SnTe growth is reevaporated again, leaving droplets of Sn on the substrate.

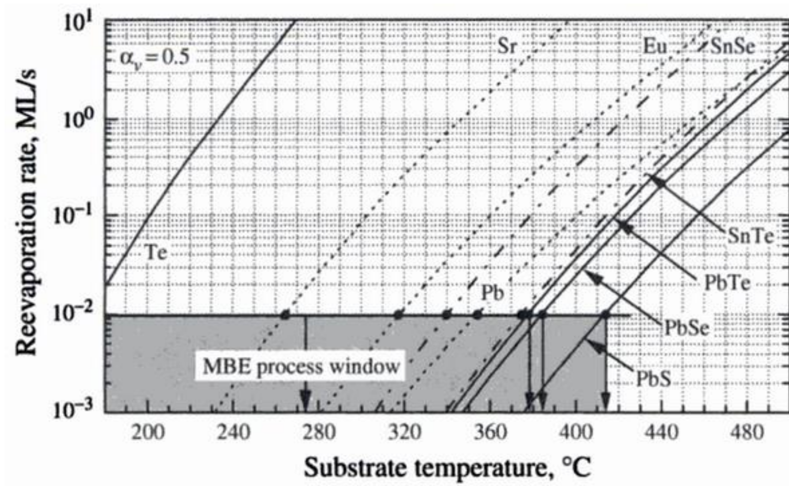

Fig. 3.13: Process window[17] for IV-VI MBE (shaded region) based on the reevaporation rates of the various components of IV-VI epilayers as a function of substrate temperature using an evaporation coefficicent of $\alpha_v = 0.5$.

References Chapter 3

1. C. Groth, M. Wimmer, A. Akhmerov, X. Waintal, ‘Kwant: a software package for quantum transport’, *New Journal of Physics*, Vol. 16, (2014).

2. C.S. Lent, ‘Relativistic empirical tight-binding theory of the energy bands of GeTe, SnTe, PbTe, PbSe, PbS, and their alloys’, *Superlattices and Microstructures*, Vol. 2, Issue 5, 491-499, (1986).

3. T. Hsieh, H. Lin, J. Liu, W. Duan, A. Bansil, L. Fu, ‘Topological crystalline insulators in the SnTe material class’, *Nat. Com. 3,* (2012).

4. P. Sessi, ‘Robust spin-polarized midgap states at step edges of topological crystalline insulators’, *Science* 354, 6317, pp. 1269-1273, (2016), Supplementary Materials.

5. F. Herman, ‘Relativistic band structure of GeTe, SnTe, PbTe, PbSe and PbS’, *Journal de Physique Colloques,* 29 (C4), 62-77, (1968).

6. Madelung, Rössler, Schuler, ‘Tin telluride (SnTe) energy gaps, interband transition energies’, *Springer Materials*, (1998).

7. S. Safaei, R. Buczko, ‘Quantum spin hall effect in IV-VI topological crystalline insulators’, *New J. Phys,* 17, (2015), (Supplementary data).

8. J.C. Slater and G.F. Koster, ‘Simplified LCAO Method for the Periodic Potential Problem’, *Phys. Rev. 94*, 1498 (1954).

9. https://en.wikipedia.org/wiki/File:Face-Centered_Cubic_Lattice_(Brillouin_zone).png

10. E. Suurmeijer, T. Mulder, J. Verhoeven, ‘Basisboek Vacuümtechniek’, *Nederlandse Vacuümvereniging*, (2008).

11. Cryo-Torr High-Vacuum Pump Installation, Operation and Maintenance Instruction, *Helix Technology Corporation*, (2001).

12. https://www.k-space.com/wp-content/uploads/BandiT_Product_Specs.pdf

13. https://www.mbe-komponenten.de/selection-guide/element/sn.php

14. https://www.mbe-komponenten.de/selection-guide/element/te.php

15. https://createc.de/index.php?index=1&menuid=29&lng=de&id=45

16. D. Khokhlov, ‘Lead Chalcogenides: Physics and Applications’, *CRC Press,* (2002).

17. G. Springholz, ‘Molecular beam epitaxy of IV-VI semiconductors: multilayers, quantum dots and device applications’, *Elsevier Science*, (2013).

4. Results and discussion

4.1 Normal state SnTe tight binding simulations

In this section the quantum transport properties of different SnTe structures are investigated. The goal is to study the topologically protected gapless surface states and edge states that are predicted for bulk surfaces[1-2] and thin films[3-4] and to gain confidence in the tight binding model that is used. Sections 2.2, 2.3 and 2.4 will mostly reproduce results from literature. In section 2.5 SnTe nanowires are studied. SnTe nanowire energy dispersions are to our knowledge not yet reported in literature. Calculating the nanowire dispersions is an important step to find out whether these nanostructures are suitable for Majorana devices.

4.1.1 Surface state dispersion

The reason for which SnTe has regained interest since about 2012 is the existence of topologically protected gapless states on its surface. The appearance of these states can be seen in studying the 3D bulk, by studying the band inversion and mirror Chern number topological invariant of the bulk as mentioned in section 2.1, but can also be obtained by studying the 2D surface band structure. Here the surface band structure calculations are treated, where the results using an eigenvalue calculation method are shown. Appendix 6.1 shows that the same results can be achieved by using a surface density of states method.

As was done in section 3.1 for the bulk band dispersion, again the translation directions with periodic boundary conditions have to be chosen. Here the translation vectors are chosen so that the first two are parallel to the surface under investigation and the third is chosen in a direction out of this plane. For the different surfaces that are mirror symmetric with respect to the $\{110\}$ plane the chosen translation directions are given by

$$
\begin{aligned}
&[001] \text{ plane: } (1,1,0), (1,\text{-}1,0) \text{ and } (1,0,1), \\
&[110] \text{ plane: } (0,0,2), (1,\text{-}1,0) \text{ and } (1,0,1) \quad \text{and} \\
&[111] \text{ plane: } (1,\text{-}1,0), (1,0,\text{-}1) \text{ and } (0,1,1).
\end{aligned}
\tag{2.2}
$$

Then the same tight binding Hamiltonian as in section 3.1 is passed together with one of the above sets of translation vectors to the Kwant Python package. Kwant then applies periodic boundary conditions in the directions of the first two vectors of the vector set and applies open boundary conditions to the third vector. The thickness in the direction perpendicular to the simulated plane can be set by specifying the open boundary conditions.

The band structure is plotted as a function of $\vec{k}$-points in the surface Brillouin zone corresponding to the surface facet that is studied, for which the $[001]$, $[110]$ and $[111]$ planes are the most relevant. The high symmetry points in the surface Brillouin zone are chosen by looking at the surface Brillouin zones corresponding to a real FCC lattice. The BCC Brillouin zone, which is the reciprocal counterpart of the real FCC lattice, is shown in Fig. 2.3, together with the 2D projections on the various surface facets. The $\vec{k}$-vectors shown here are in the original orthogonal basis.

The band structures that are obtained for the different surface facets are shown in Fig. 4.3 and 4.4. The surface Brillouin zone corresponding to the simulated surface facet, are shown in the insets of the figures. They correspond to the surface Brillouin zones marked in green in Fig. 4.1. The parts of high symmetry lines along which the eigenvalues of the system are calculated are marked red in the insets.

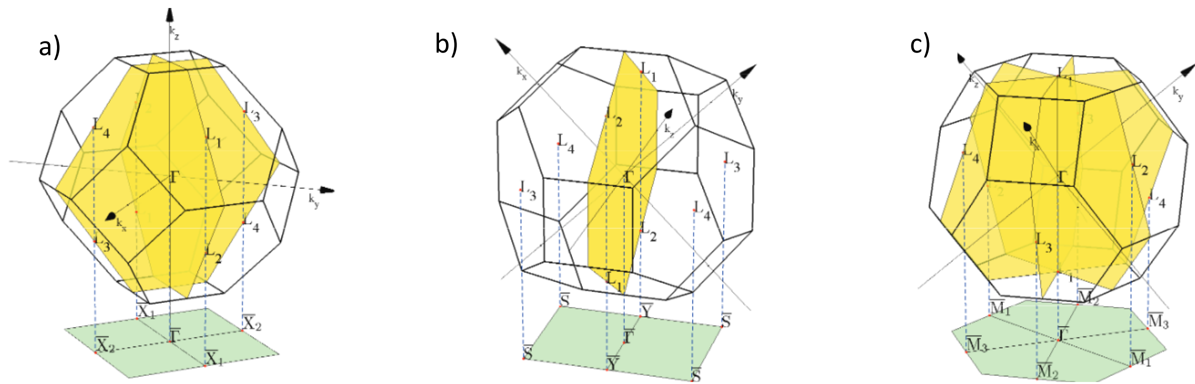

Fig. 4.1: The Brillouin zone corresponding to the FCC lattice of SnTe. The 2D surface Brillouin zones are shown in green for the (a) $[001]$ *, (b)* $[110]$ *and (c)* $[111]$ *surface facets. The* $[110]$ *mirror planes are marked in yellow. Figures reproduced from ref. 2.*

Each point in the band structure also shows a color which represents the contribution of the orbitals of the Sn atom (the cation) to the wave function corresponding to that point in the band structure. The colors clearly show the band inversion for the (001) and (110) surfaces. The top of the valence band (the bottom of the conduction band) clearly shows that the wave functions corresponding to these states are dominated by the Sn atom (Te atom), whereas the rest of the valence band (conduction band) states are dominated by the Te atom (Sn atom).

The surface state dispersions show four Dirac cones in the Brillouin zone. A distinction of two types[5] of surface states can be made which have qualitatively different properties. The first type is found for the (001) and (110) surface facets, for which the surface state dispersions are shown in Fig. 4.3a) and b) respectively. For these the Dirac cones are not located exactly on the high symmetry points, which are the time-reversal-invariant momenta, but are displaced from it along the {110} mirror planes. This type of surface states exhibit a Lifshitz transition[5] as a function of Fermi energy, which is accompanied by a Van Hove singularity in the density of states arising from saddle points in the band structure.
The (001) surface state dispersion shown in Fig. 4.3a) shows a Dirac cone on the $\overline{\mathrm{X}}-\overline{\Gamma}$ line located displaced but close to the $\overline{\mathrm{X}}$-point. 4 Dirac cones emerge near the two inequivalent $\overline{\mathrm{X}}$-points in the (001) Brillouin zone. The shift away from the $\overline{\mathrm{X}}$-point is due to the interaction between different L valleys in the 3D Brillouin zone. Displaced off the $\overline{\mathrm{X}}$-point along the $\overline{\mathrm{X}}-\overline{\mathrm{M}}$ is a anticrossing with a gap of 0.037 eV. The reason why there is a Dirac cone (crossing) at the $\overline{\mathrm{X}}-\overline{\Gamma}$ line, but not at the $\overline{\mathrm{X}}-\overline{\mathrm{M}}$ line is that the $\overline{\mathrm{X}}-\overline{\Gamma}$ line coincides with a $\{110\}$ symmetry plane, while the $\overline{\mathrm{X}}-\overline{\mathrm{M}}$ line does not.
The (110) surface state dispersion shown in Fig. 4.3b) shows a Dirac cone close to the $\overline{\mathrm{Y}}$-point, and a anticrossing close to the $\overline{\mathrm{S}}$-point. This is again because the first is located in the $\{110\}$ symmetry plane, while the latter is not.

The second type of surface states is found on the $\{111\}$ facets. Here the 4 Dirac cones are located exactly at the $\bar{\Gamma}$ and $\bar{\mathrm{M}}$ points. Choosing an odd number of atomic monolayers enables to study separately slabs with surfaces consisting of only Sn or Te. This polar behavior of the $\{111\}$ facets is shown in Fig. 4.2. For the slab with only Sn terminations the Dirac point, which is the point where the gapless states actually cross, merges with the top of the valence band as is shown in Fig. 4.4a). For the slab with only Te terminations the Dirac points merges with the bottom of the valence band, which is shown in Fig. 4.4b).

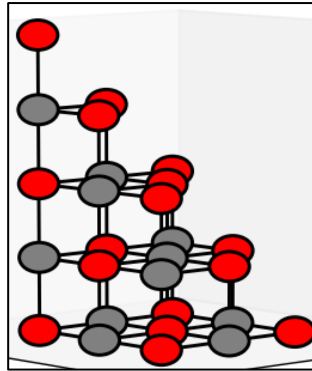

Fig. 4.2: Rod-stick model of the polar $\{111\}$ *surface.*

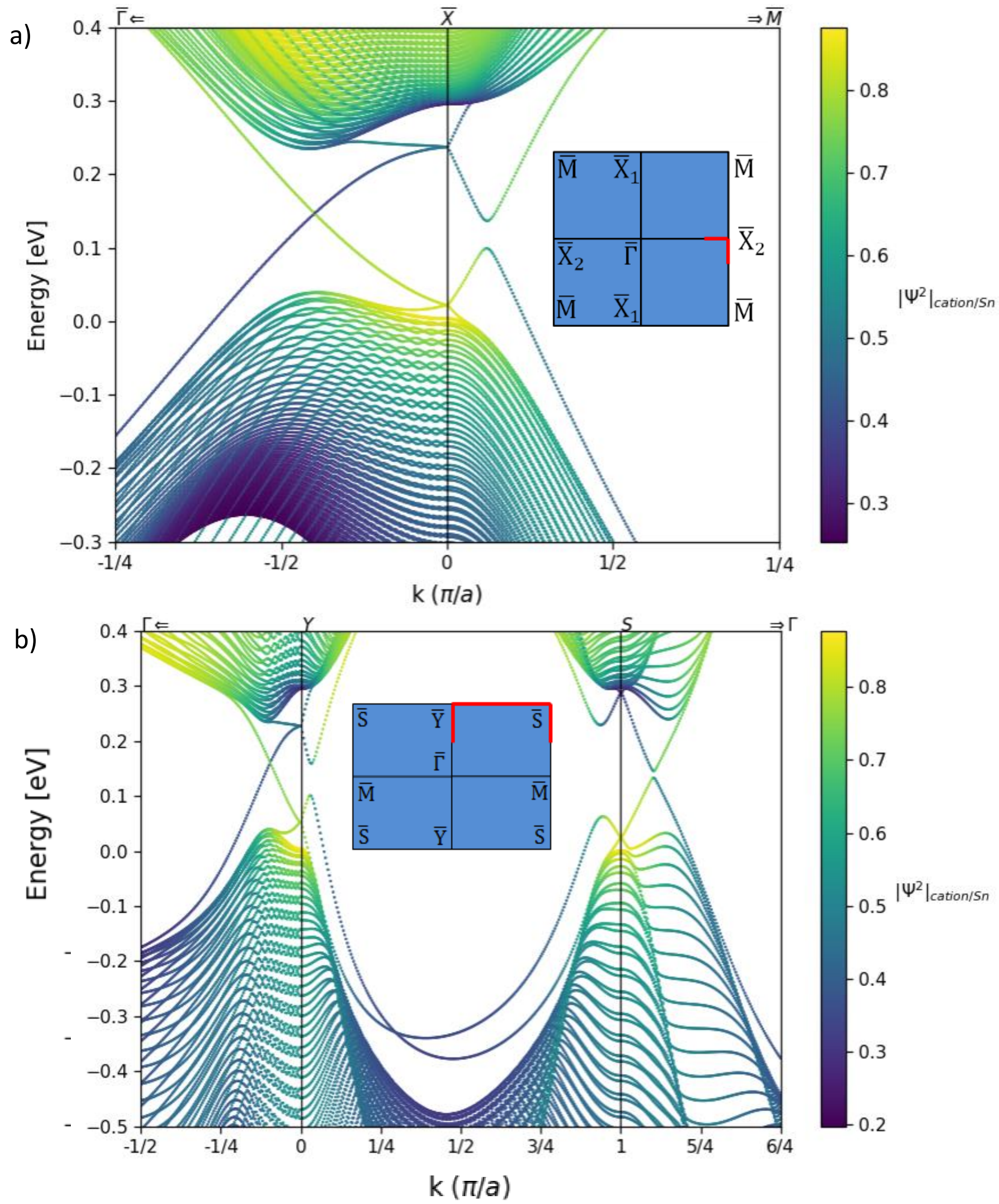

Fig. 4.3: Energy dispersion of SnTe for the (a) (001) *and (b)* (110) *surface facets. The* (001) *slab is 141 atomic monolayers (atml) or* $44\ \mathrm{nm}$ *thick, were an inter-layer distance of half a lattice constant* a *per atomic monolayer is used. The simulated* (110) *slab, which has a different inter-layer distance of* $\frac{a}{2}\sqrt{2}$*, is 159 atml or* $71\ \mathrm{nm}$ *thick. In the bottom-left of a) is a white area where there should also be states, but this could be optimized by raising the number of calculated eigenvalues or using the density of states method discussed in appendix 6.1.*

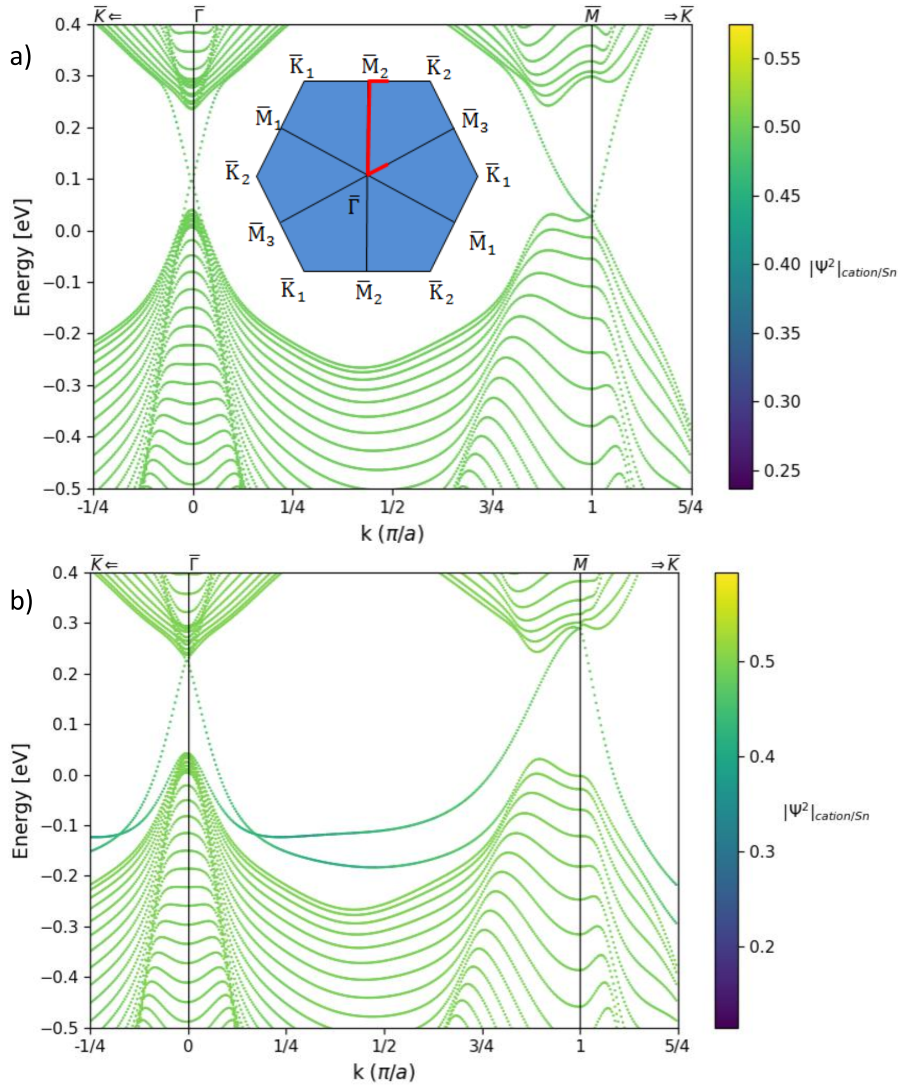

Fig. 4.4: Energy dispersion of SnTe for the (111) *surface facets with (a) Sn and (b) Te terminated surfaces. The Sn-terminated slab is 141 atomic monolayers (atml) or* $77\,nm$ *thick, while the Te-terminated slab is 143 atomic monolayers (atml) or* $78\ \mathrm{nm}$ *thick, were an inter-layer distance of* $\frac{a}{2}\sqrt{3}$ *per atomic monolayer is used. For the* (111) *surface facets no band inversion in the surface state dispersion was observed.*

4.1.2 Demonstration of edge states in thin films

This section will look into similar simulations as section 4.1.1, but looking into much thinner slabs of SnTe. In section 4.1.1, for example for the $[001]$ facet, a unit cell of 2×139 atoms was used, corresponding to a thick slab of $71\ \mathrm{nm}$ thickness. In appendix 6.1 it is shown that the resulting (surface) dispersion is the same for a semi-infinite slab. So we can conclude that the films in section 4.1.1 are in the thick slab regime. This means that the surface states on both sides of the film do not overlap. However when the film thickness is decreased to about 50 atoms or 16 nm, the wave functions of the surface states on both sides of the thin film start to overlap. This overlapping or interaction of the wave functions results in the opening of a gap in the Dirac cone. In Fig. 4.5 the energy of the opened gap is plotted in red for $[001]$ thin films consisting of an odd or even number of layers[6]. The graph shows an oscillation of the energy gap in addition to an exponential decay as function of the thickness. The damped oscillation is also known for the TI Bi_2Se_3[7-8], as shown in blue. In green the bandgap (not induced bandgap) of PbTe is shown. This bandgap does not oscillate, it only decays exponentially for small thicknesses and stabilizes after 60 atomic monolayers. Besides the oscillations and exponential decay an even-odd effect appears for SnTe. The top and bottom layers are the same for odd numbers of layers of the $[001]$ film, while they are different for an even number of layers. This results in different symmetries of the odd and even systems, and therefore different topological invariants have to be defined for both. The consequence is the different dependencies of the energy gap on the film thickness. Similar dependencies of the energy gap are found for $[111]$ thin films[3].

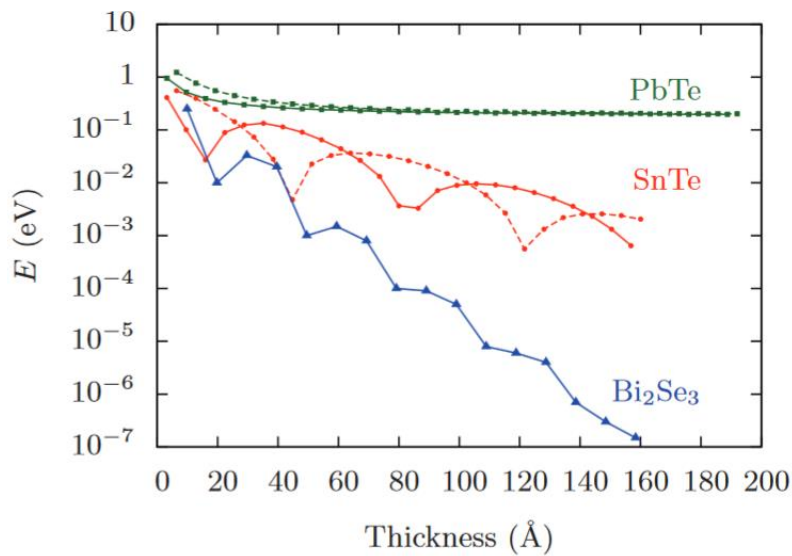

Fig. 4.5: Induced energy gap dependence on the thin film thickness. Figure reproduced from ref. 6.

To illustrate the opening of a gap in the Dirac cone of the $[001]$ surface facet, its band structure is plotted for different film thicknesses in Fig. 4.5 above. By reducing the slab thickness from 61 to 31 atomic monolayers (atml) a gap clearly opens up. Additionally, by reducing the slab thickness even further from 31 to 23 does not raise the induced gap, but lowers it somewhat again. This indicates the oscillating behavior of the induced gap as a function of film thickness. For lower film thickness the induced gap gets even larger, however the overall gap seems to be limited by the 40 meV gap of

the anticrossing along the $\bar{X}-\bar{M}$ line. This 40 meV limit of the gap seems to be in contrast to Fig. 4.5 were the SnTe energy gap raises further to 300 meV, however probably only the induced energy gap $E_{g,ind}$ is plotted, not the overall gap which is smaller.

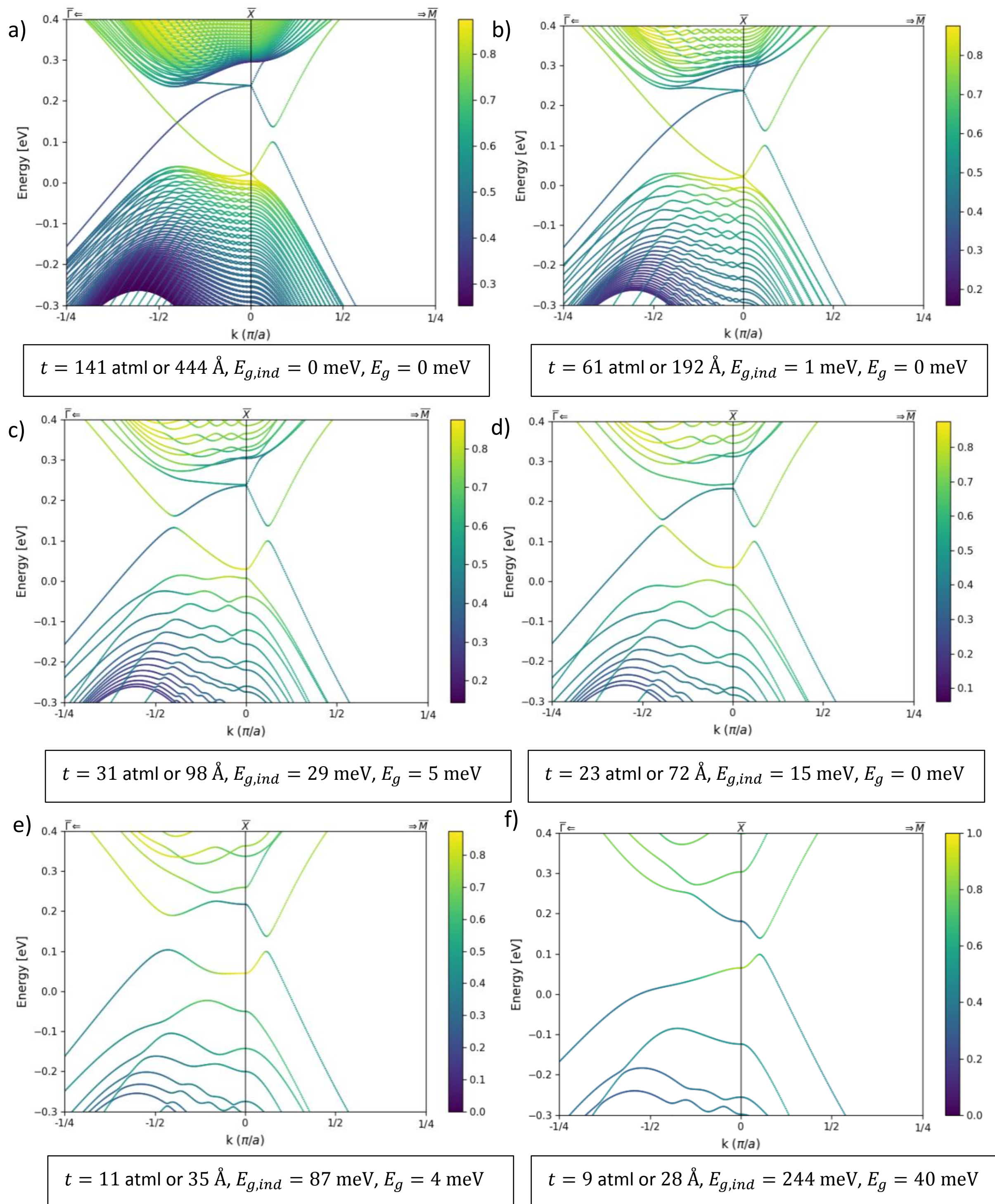

Fig. 2.8: Energy dispersion of a 2D film without edges for different thicknesses of (a) 444 Å *, (b)* 192 Å *, (c)* 98 Å *, (d)* 72 Å *, (e)* 35 Å *, (f)* 28 Å*. Under each plot the induced gap* $E_{g,ind}$ *(left of the* $\bar{X}$*-point) is given as well as the overall gap* E_g *that is calculated by taking into account the gaps at both sides of the* $\bar{X}$*-point. For 9 atml or* 28 Å *the induced gap is merged with the valence and conduction bands. The color bars represents the* $|\Psi|^2_{cation/Sn}$*.*

While it can be seen in Fig. 4.5 that the Dirac cones on the 2D infinite surface start to gap out for very thin films ($\lesssim 16$ nm), this is not true for the edges of a 2D surface. In literature this was first found for the $[001]$[9] surface and was later extended to $[111]$[3] and $[110]$[6] surfaces. In this section the dispersion of such thin films with edges are calculated. The dispersion is calculated using an eigenvalue method by defining a unit cell with a thin side in the direction perpendicular to the surface facet and a long side parallel to the surface facet. Next periodic boundary conditions are applied in the direction perpendicular to this 2D cross-section.

It turns out that the details of the dispersion depend strongly on the number of layers. However overall it can be stated that if edge states are present we can make the following observations: The $[001]$ facet will have 2 Dirac cones per BZ near $k = \pm\pi$ at its $[100]$ or $[010]$ edge. An example of the band structure is shown in Fig. 4.7 for a thin film with a 79 × 9 atml cross-section. The example is for a $[100]$ surface facet, with the edge is along the $[001]$ direction and the long 79 atml side in the $[010]$ direction. The same cross-section is modeled in appendix 6.1 using a density of states method. In Fig. 4.6 the wave function probability $|\Psi|^2$ summed over the lowest 4 states near the Dirac point is plotted, where Ψ is the wave function. The eigenvalues are 2 times degenerate, because both edges of the thin slab contribute one Dirac cone shifted right from $k = \pi$ and one shifted left from $k = \pi$.

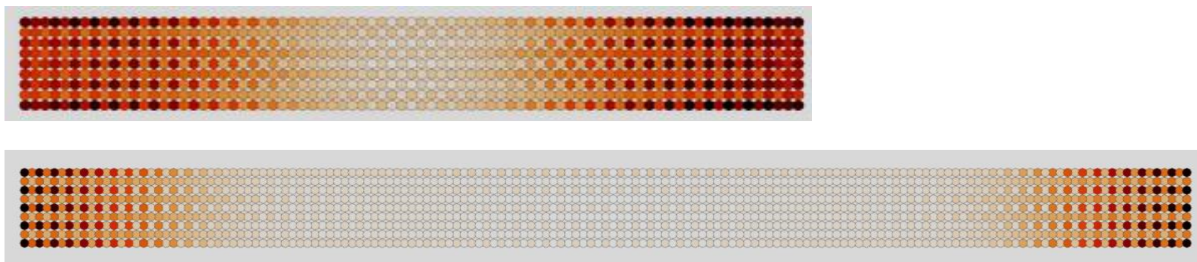

Fig. 4.6: Plot of sum of the lowest 4 states near the Dirac point for a 79×9 atml (249×28 Å) and a 157×9 atml (495×28 Å) slab.

The $[110]$ surface will have 2 Dirac cones per BZ, where one is located at $k = \pm\pi$ and one is located at $k = 0$. An example of the band structure is shown in Fig. 4.8 for a thin film with a 151×11 atml cross-section. The example is for a $[110]$ surface facet, with the edge is along the $[1\text{-}10]$ direction and the long 151 atml side in the $[001]$ direction.

The $[111]$ surface will have 1 Dirac cone per BZ located at $k = 0$. An example of the band structure is shown in Fig. 4.9 for a thin film with a 301×16 atml cross-section. The example is for a $[111]$ surface facet, with the edge is along the $[\text{-}1\text{-}12]$ direction and the long 151 atml side in the $[1-10]$ direction.

The $[111]$ surface facet has only 1 Dirac cone on its edge, therefore its $\mathbb{Z}_2$ topological invariant has a non-trivial value and can therefore be classified as a quantum spin Hall (QSHI) insulator. It is shown in literature[3] that for a thin film with an even number of layers, which does not have inversion symmetry, the topological phase can be found by directly calculating the edge states. For thin films with an odd numbers of layers the $\mathbb{Z}_2$ topological invariant can be calculated. The $\mathbb{Z}_2$ topological invariant is non-trivial (topological) if the parity of the occupied Bloch wave functions is odd at an odd number of time-reversal invariant (TRIM) points in the Brillouin Zone. Therefore to calculate $\mathbb{Z}_2$ these parities are calculated at $(k_x, k_y) = (0,0), (0,\pi), (\pi, 0)$ and (π,π). For certain thicknesses and

surface terminations of the $[111]$ surface (infinite in the two directions perpendicular to $[111]$) the parities are found to be odd at $(k_x, k_y) = (0,0), (0, \pi)$ and $(\pi, 0)$, but even at (π, π) which makes $\mathbb{Z}_2$ non-trivial. It is reported that the bandgap in the QSHI phase can reach $18\ \mathrm{meV}$ at 25 layers for Sn termination and $66\ \mathrm{meV}$ at 19 layers for Te termination. This was checked but smaller gaps were found of $6\ \mathrm{meV}$ and $10\ \mathrm{meV}$ respectively. This could be due to a different choice in edges, namely we choose the edges [1-10] and [-1-12] with a width of 601 atml in the [1-10] direction. Only the fact that the edges were of armchair-type was reported in literature, not their directions.
The $\mathbb{Z}_2$ topological invariant is also calculated for topological $[001]$ and $[110]$ thin films with odd number of layers. For the $[001]$ thin film the parity was odd on all 4 TRIMs, while for the $[110]$ film the parity of even for all 4 TRIMS. Since the parity is thus not odd of an odd number of TRIMs, these films cannot be identified as a quantum spin Hall Insulator. However this does not necessarily mean that these films cannot be applied in Majorana devices. Since there are no proposals yet of these films in Majorana devices, their potential for generating Majoranas is investigated in section 4.2.3, where the focus is on comparing the $[001]$ and $[111]$ thin films.

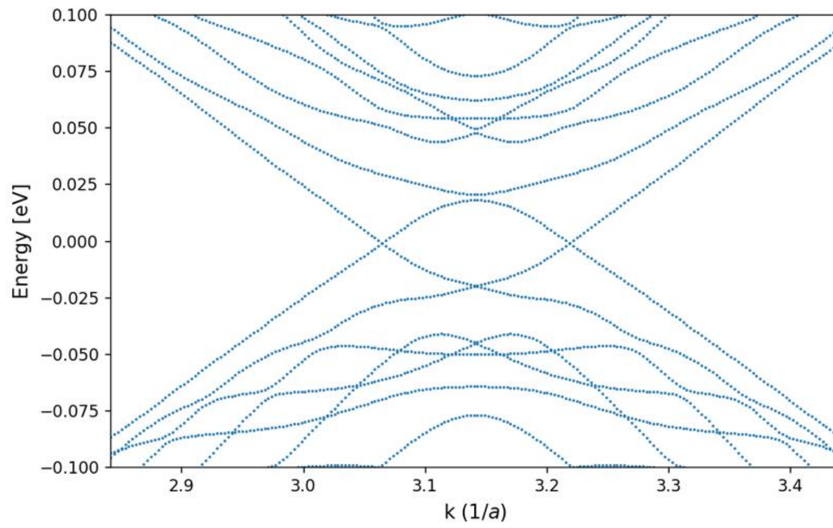

Fig. 4.7: Thin film dispersion for a $[100]$ surface facet with 79×9 atml or 249×28 Å cross-section, with the edge along the $[001]$ direction and the long 79 atml side in the $[010]$ direction. The chemical potential is set at $\mu = -0.12$. For the calculations where the chemical potential is not mentioned $\mu = 0$.

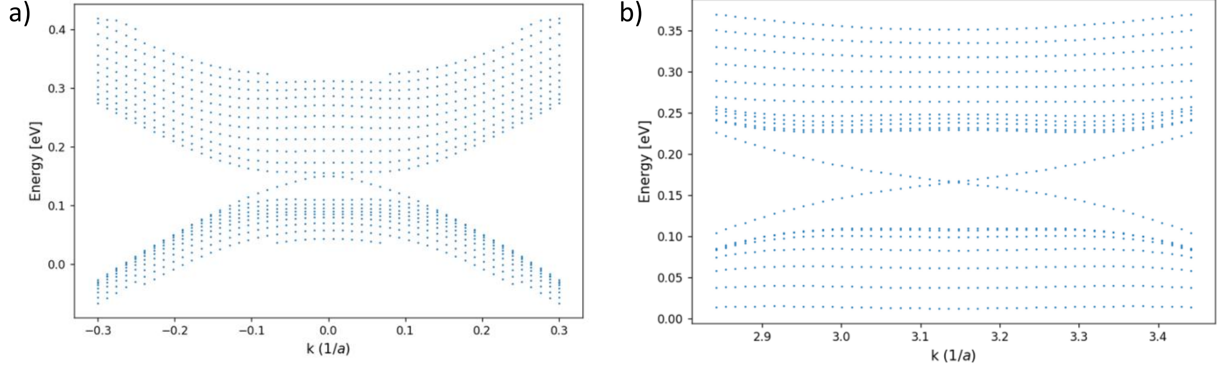

Fig. 4.8: Thin film dispersion for a $[110]$ *surface facet with* 151×11 *atml or* 476×49 Å *cross-section, with the edge is along the* $[1-10]$ *direction and the long* 151 *atml side in the* $[001]$ *direction. (a) around* $k = 0$ *and (b) around* $k = \pi$.

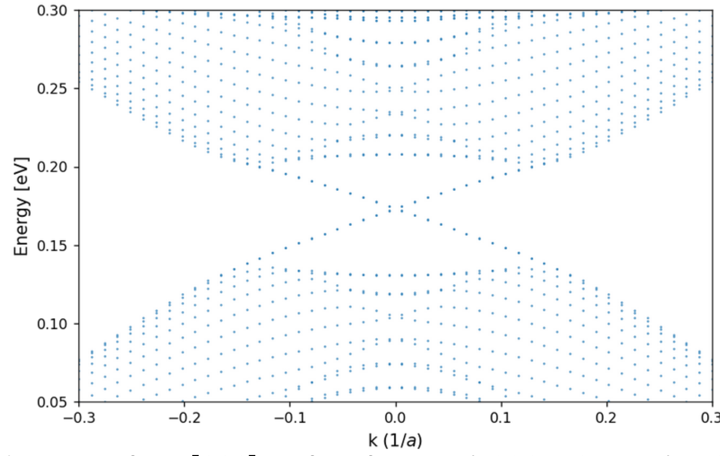

Fig. 4.9: Thin film dispersion for a $[111]$ *surface facet with* 301×16 *atml or* 1340×87 Å *cross-section, with the edge is along the* [-1-12] *direction and the long* 301 *atml side in the* [1-10] *direction.*

As noted above, the details of the dispersion depend strongly on the number of layers. Moreover it matters whether the thin slab has an even or odd number of atomic layers. For example the topological regions for odd and even number of layers of a $[001]$ thin film are shown in Fig. 4.10. For an odd number of layers the thin film is topological between 3 and 51 number of layers, as (Fig. 4.10a)), while for the even number of layers this is between 12 and 38 number of layers (Fig. 4.10a)). For the odd number of atomic layers holds that if the mirror Chern number N_M has a value of $+2$ or -2 , the thin film is topological and has edge states. If $N_M = 0$ it is non-topological and has no edge states. For the even number of atomic layers holds that if the winding number ζ_M has a value of 2, the thin film is topological, while if $\zeta_M = 0$ it is not[14].

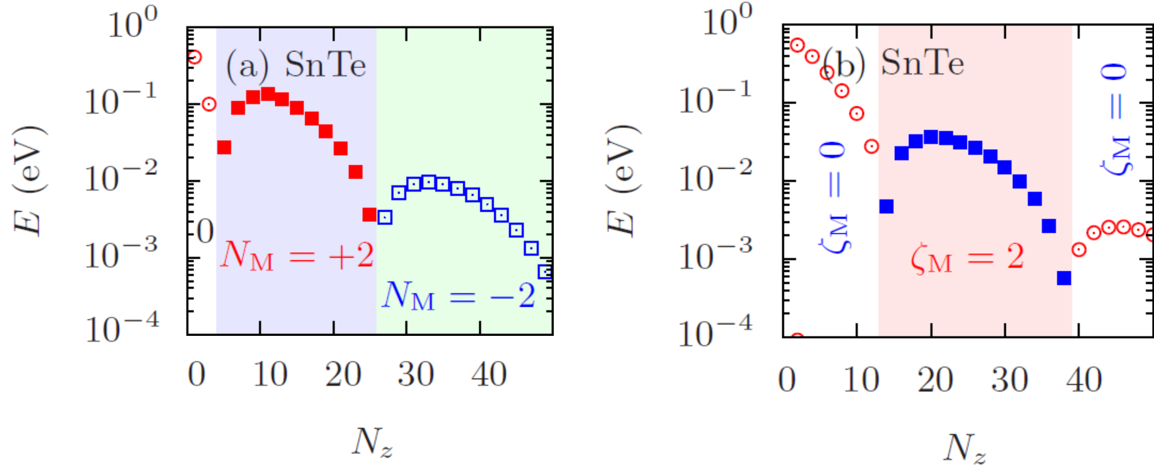

Fig. 4.10: (a) Topological phase diagram in odd number of layers of a $[001]$ *thin film of SnTe. TCI with* $|N_M| = 2$ *is realized in the shaded regions. The energy gap is denoted by the open circles, closed squares, and open squares for a nontopological insulator* $N_M = 0$*, a TCI with* $N_M = 2$*, and a TCI with*$N_M = -2$*, respectively. (b) Topological phase diagram in even number of layers of a* $[001]$ *thin film of SnTe. Energy gap and topological invariant* ζ_M *are shown.* $|\zeta_M| = 2$ *is denoted by the closed square in the shaded region. Figures reproduced from ref. 6.*

4.1.3 Simulating non-superconducting SnTe Nanowires

In this section, in a similar way as in section 4.1.2 the dispersions of SnTe nanowires are modeled. Nanowires are quasi-1D systems having a cross-section within the range of 10 to $100\ \mathrm{nm}$. The SnTe nanowires show quite different dispersions for nanowires with different facets. In Fig. 4.11 below the nanowire dispersions for a nanowire with a $[001]$ translation direction, with $[010]$ and $[100]$ facets are shown for different sizes of its cross-section.

As is discussed in section 2.2.2 no Dirac cones are to be expected, only gapped Dirac cones. Indeed no gapless surface states are found in the dispersions of the $[001]$ oriented nanowire. Only in Fig. 4.11b) for a $13 \times 13\ \mathrm{nm}$ cross-section there are features in the dispersion close to $E = 0$ and $k = \pi$ that look like gapped Dirac cones, so Dirac physics seems to be present. However, what was not expected, the bandgap seems to close for cross-section larger than about $13 \times 13\ \mathrm{nm}$. For these cross-section the Dirac cones seem to be buried in the bulk bands. A possible explanation is that the bandgap is filled up with trivial surface states.

The nanowire dispersions for nanowires with certain $[111]$ and $[110]$ facets are plotted in Fig. 4.12 and 2.16 respectively for different cross-sections. Fig. 4.12 shows the dispersion for a rectangular $[1\text{-}10]$ oriented nanowire with $[001]$ and $[110]$ side-facets. In Fig. 4.13 the nanowire dispersions for a rectangular $[\text{-}1\text{-}12]$ oriented nanowire with $[\text{-}110]$ and $[111]$ side-facets are plotted for different cross-section. Both sets of figures show that the gap is closing for increasing size of the nanowire cross-section. In Fig. 4.13a) for a $[\text{-}1\text{-}12]$ oriented nanowire with $[\text{-}110]$ and $[111]$ side-facets a nicely gapped spectrum is plotted. However the Dirac cone has a small gap and the cross-section is unrealistically small.

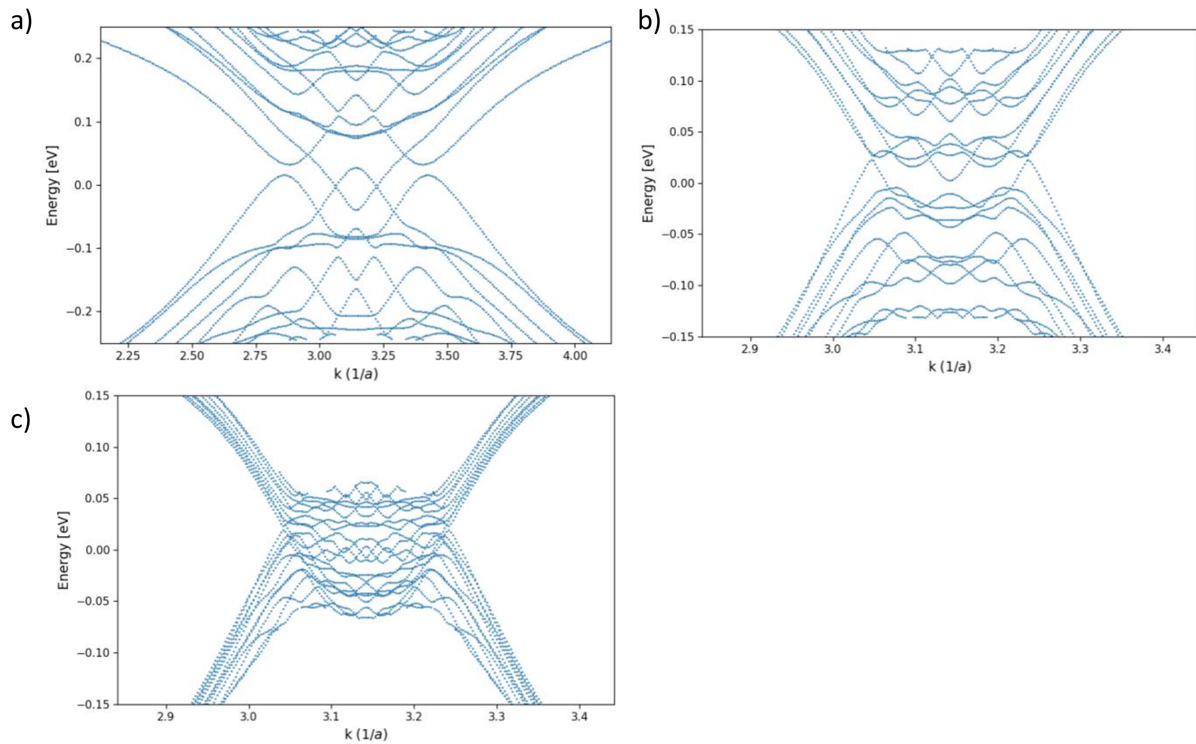

Fig. 4.11: Nanowire dispersions for a square $[001]$ *oriented nanowire with* $[010]$ *and* $[100]$ *side-facets for (a)* 21×21 *or* 66×66 Å, *(b)* 41×41 *or* 129×129 Å *and (c)* 81×81 *or* 255×255 Å *cross-sections. The chemical potential is set at* $\mu = -0.12$.

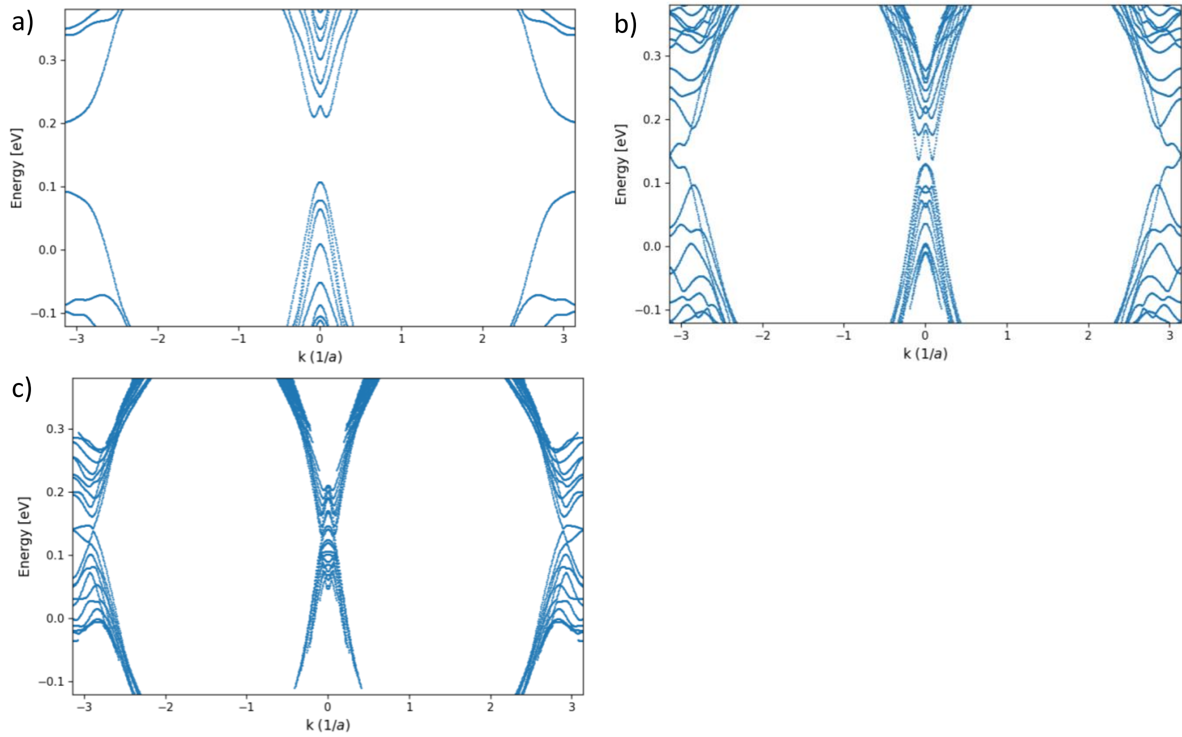

Fig. 4.12: Nanowire dispersions for a rectangular [1-10] *oriented nanowire with* [001] *and* [110] *side-facets for (a)* 21×21 *or* 66×93 Å, *(b)* 41×41 *or* 129×183 Å *and (c)* 81×81 *or* 255×361 Å *cross-sections.*

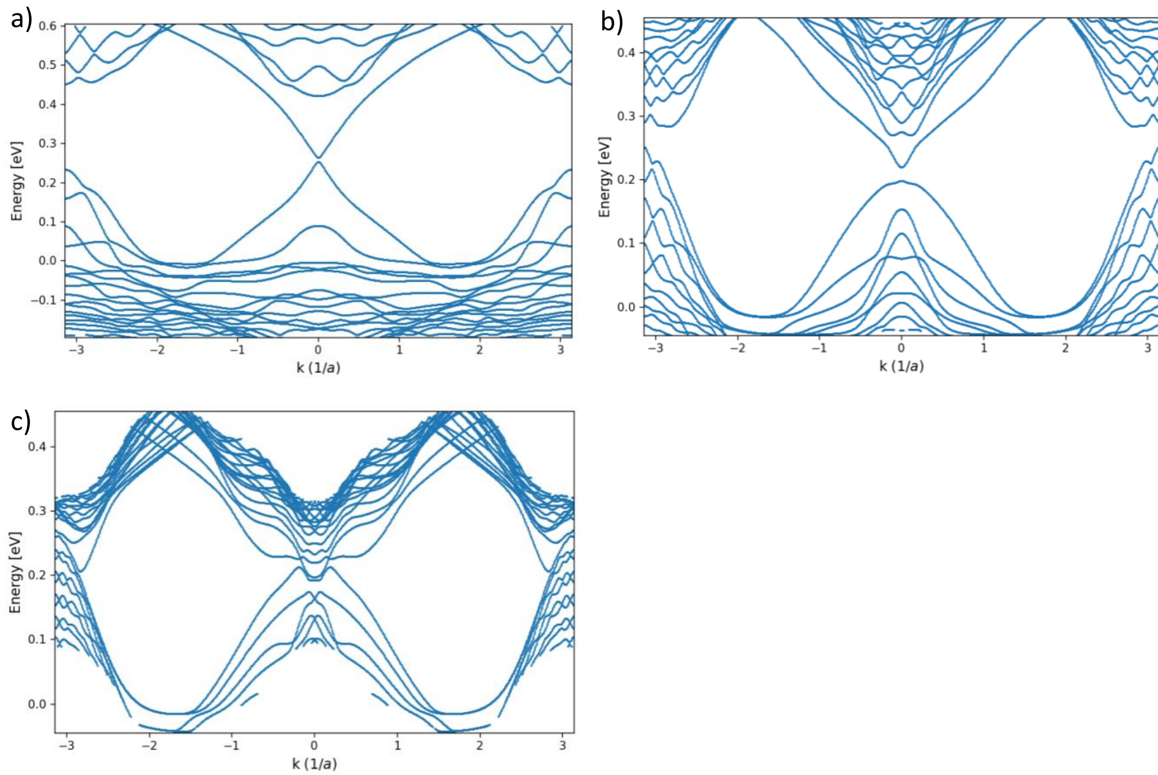

Fig. 4.13: Nanowire dispersions for a rectangular [-1-12] *oriented nanowire with* [-110] *and* [111] *side-facets for (a)* 21×21 *or* 94×115 Å, *(b)* 41×41 *or* 182×224 Å *and (c)* 81×81 *or* 361×442 Å *cross-sections.*

4.1.4 Modelling the Magnetic fields in SnTe

As discussed in section 2.2.2 a magnetic field parallel to the nanowire is needed to make sure surface states are present. The magnetic field is realized in the model by the introduction of a Zeeman term in the Hamiltonian that deals with the effect of the magnetic field on spin of the electron and the by introduction of a Peierls substitution to deal with the magnetic effect on the orbital part of the momentum of the electrons.

Zeeman Hamiltonian

The Zeeman splitting is chosen the same for both the anion and cation, but different for the each orbital. In the following the derivation of the Zeeman Hamiltonian for the 18 orbital sp3d5 model is given. For the 6-orbital p3 model the derivation is similar but only for the p orbitals.

The Zeeman Hamiltonian of a particular orbital is given by

$$H_Z = \vec{B} \cdot \vec{M}, \tag{2.3}$$

where $\vec{B}$ is the magnetic field and $\vec{M}$ is the orbital's magnetic moment

$$\vec{M} = \begin{pmatrix} M_x \\ M_y \\ M_z \end{pmatrix}, \tag{2.4}$$

where M_i are magnetic moment matrices for each component x, y and z.

The derivation for M_z is given below. M_z is an 18×18 matrix. Assuming that the electron behaves as a free electron in a magnetic field, it is given by

$$M_z = \mu_B(2S_z + L_z), \tag{2.5}$$

where $\mu_B = 5.79 \cdot 10^{-5}\mathrm{eV} \cdot \mathrm{T}^{-1}$ is the Bohr magneton and S_z and L_z are the spin and orbital momentum matrices of the orbitals.

Since the s-orbitals do not have an angular component L_z (the angular momentum quantum number $l = 0$), the 2×2 magnetic moment matrix of the s-orbitals is given by

$$M_{s,z} = 2\mu_B S_z = 2\mu_B \sigma_z = 2\mu_B \begin{pmatrix} 1 & 0 \\ 0 & -1 \end{pmatrix}, \tag{2.6}$$

where σ_z is the Pauli matrix for the z-component of the spin. The $M_{s,x}$ and $M_{s,y}$ components are acquired by replacing σ_z by σ_x and σ_y.

The i-th component of magnetic moment matrix of the p-orbitals is given by 6×6 matrix

$$M_{i,d} = \mu_B(2S_i \otimes I_3 + I_2 \otimes L_i), \tag{2.7}$$

where I_n is the $n \times n$ unit matrix and $S_z = \sigma_i$ is again the Pauli matrix corresponding to the component of the magnetic moment. The derivation of the L-matrices for the p-orbitals is given in

appendix 6.2.2. The magnetic moment matrix of the d-orbitals is calculated similarly, where also the derivation of the L-matricces for the d-orbitals is given in appendix 6.2.3.

Peierls substitution

The Peierls substitution[10] is a method to deal with the effect of the magnetic field on the orbital motion of electrons. For example the Aharonov-Bohm effect can be simulated by using a Peierls substitution. The gauge-invariance of the Schrodinger equation requires to transform the wave-function amplitude or equivalently the creation operator of an electron at a site as

$$c_j^\dagger \to c_j^\dagger e^{-i\frac{e}{\hbar}\Lambda(r_j)} \tag{2.8}$$

where $\Lambda(r_j)$ generates at site j the gauge transformation of the vector potential $\vec{A}(\vec{r}) \to \vec{A}(\vec{r}) + \nabla\vec{A}(r)$. If there is no magnetic field then the vector potential can locally be set to $\vec{A} = 0$ by an appropriate gauge choice of Λ. The hopping term in the absence of a vector potential is written as $H_t = t_{jl} c_j^\dagger c_l + h.c.$, where $h.c.$ is the Hermitian conjugate, which must gauge transform to

$$H_t = t_{jl} e^{-i\frac{e}{\hbar c}\left(\Lambda(r_j)-\Lambda(r_l)\right)} c_j^\dagger c_l + h.c. = t_{jl} e^{-i\frac{e}{\hbar}\left(\int_{r_l}^{r_j} dr' \cdot A(r')\right)} c_j^\dagger c_l + h.c. \tag{2.9}$$

While this expression is derived for zero magnetic field it is used to include magnetic fields in lattice models by choosing the integration path to be the shortest distance over nearest neighbor bond.

The vector potential is not unique, but is chosen in our model to be

$$\vec{A}(\vec{r}) = \begin{pmatrix} (z-z_0)B_y - (y-y_0)B_z \\ 0 \\ (y-y_0)B_x \end{pmatrix}, \tag{2.10}$$

where (x_0, y_0, z_0) is the origin of the system and (x, y, z) is the difference vector of the start vector of a nearest-neighbor hopping. Therefore

$$\vec{A} \cdot \vec{r} = \begin{pmatrix} (z-z_0)B_y - (y-y_0)B_z \\ 0 \\ (y-y_0)B_x \end{pmatrix} \cdot \begin{pmatrix} x_j - x_l \\ y_j - y_l \\ z_j - z_l \end{pmatrix}. \tag{2.11}$$

The transformation of the hopping terms is then

$$c_j^\dagger \to c_j^\dagger e^{-i\frac{e}{\hbar}\vec{A}\cdot\vec{r}}. \tag{2.12}$$

4.2 Modelling SnTe Majorana devices

In this section the potential of SnTe nanostructures for Majorana devices is investigated. Section 2.2.2 introduced that a TI nanowire can host Majorana fermions (in combination with a parallel magnetic field and induced superconductivity). Besides that section 4.1.2 showed that SnTe thin films host topological phases, where the $[111]$ thin film is particularly interesting due to its quantum spin Hall phase. To generate the Majorana fermions typically magnetic fields and induced superconductivity are needed. Simulating the magnetic fields in SnTe was already discussed in section 4.1.4. In section 4.2.1 the introduction of superconductivity to the model is treated. While we were not able to show any Majorana fermions in SnTe nanowires yet, in section 4.2.2 the potential of this method is discussed. In section 4.2.3 another approach of generating Majorana fermions using SnTe thin films is discussed, which is supported by simulations including superconductivity. Indications of Majorana fermions in SnTe thin films are discussed.

4.2.1 Modelling superconductivity

The s-wave superconductive coupling is applied to the original model hamiltonian H by transforming it into a Bogoliubov-de Gennes Hamiltonian[11] given by

$$H_{BdG} = \begin{pmatrix} H & \Delta \\ -\Delta^* & -H^* \end{pmatrix}, \tag{3.2}$$

where Δ is the superconducting order parameter.
H_{BdG} has a higher symmetry than H, since H_{BdG} is conserved under applying the particle-hole symmetry operator P, i.e.

$$PH_{BdG}P^{-1} = -H_{BdG}. \tag{3.3}$$

Because of the minus sign in the particle-hole symmetry, the spectrum of H_{BdG} must be symmetric around zero energy.

4.2.2 Majorana fermions in SnTe nanowires

As discussed in section 3.2, TI nanowires, which have a single Dirac cone can host Majorana fermions. A magnetic field has to be applied parallel to the nanowire growth axis to make sure surface states are running over the nanowire as shown in Fig. 3.4 for the non-superconductive state. Then inducing s-wave superconductivity to the wire will produce Majorana fermions at each of its ends. We have not been able to show yet the existence of Majoranas in the SnTe, which is a TCI (section 2.3) and not a TI (section 2.2). To show the existence of Majoranas in SnTe nanowires the following steps have to be taken:

First of all the existence of topologically protected surface states on the nanowire geometry have to be demonstrated. Therefore the dispersions for different nanowire cross-section (sizes and surface facets) have been calculated in section 2.4. While Dirac cones on these nanowires were expected, the bandgaps of these nanowires seemed to close for larger nanowire cross-sections. While there were indications of Dirac physics (mostly in Fig. 2.16a)) no full Dirac cones (without a gap in the Dirac cone) where found, located in a considerably sized gap in the energy dispersion.

Secondly to show the existence of Majorana fermions in SnTe nanowires it would be a huge improvement if the model would be reduced to an effective model. Quite big nanowire cross-sections had to be simulated in section 3.4, which makes computations very expensive. Also the surface state spectrum kept changing when changing the nanowire cross-section, which indicates that the simulated nanowire cross-sections were not even big enough. If it can be shown that the SnTe nanowire for a certain type of surface facets (such as $\{001\}$) has a specific number of Dirac cones on specific $\vec{k}$-points, then maybe such an effective model can be formulated. In this effective model the units cell could then be decreased to a much smaller size than the one used now for a full nanowire crossection.

Finally here we convey our thoughts on the different surface facets of SnTe nanowires. The results of section 3.4 showed a closing of the bandgap for increasing nanowire diameter. However if it is assumed that the bandgap would stay open still some conclusions can be done. First of all, except for the simulations which have $[111]$ surfaces, the number of Dirac cones (if the gap would not close) seems to be 2. This is the same as was found for the $[001]$ and $[110]$ thin films in section 3.3. Since the original TI Majorana nanowire proposal discussed in section 3.2 has only 1 Dirac per BZ it is not clear whether this proposal would work for a TCI with 2 Dirac cones on its surface. With an effective model this could be investigated. Such a model was not found yet since for example the $[001]$ wires the Dirac cones seem to be close to $k = \pm\pi$, while most effective models in literature produce Dirac cones at $k = 0$.

4.2.3 SnTe thin film superconducting junctions

The SnTe $[111]$ QSHI slab is simulated in the π-junction geometry discussed in section 2.2.3 (Fig. 2.7) to check whether these Majorana fermions are also generated in SnTe. A schematic of the simulated geometry is shown in Fig. 4.14. This geometry is basically only the part of the superconducting ring near the junction, but in our simulation the width of the junction is set to $L = 0$. Besides that the superconducting phase difference of the junction in our simulation is not implemented by a magnetic field, but by directly implementing the superconducting phase into the superconducting part of the Hamiltonian of the system.

For the simulation of the thin film geometry of Fig. 4.14 a different model[12-13] is used then was used for all the previous simulations. The model used is a 6 orbital model that only simulates the p-orbitals of SnTe. The model is not derived from the 18 orbital model used above and it also does not produce the exact same energy dispersions. Still it reproduces most characteristics such as the number of Dirac cones quite well, however mostly for different (often smaller) dimensions of the geometry as for the 18 orbital model. This model is used to make computations less expensive, since by introducing superconductivity into the model the size of the Hamiltonian is increased from $N \times N$ to $2N \times 2N$. Also the computations to confirm the existence of Majorana fermions such as conductance calculations are slower than energy dispersion calculations.

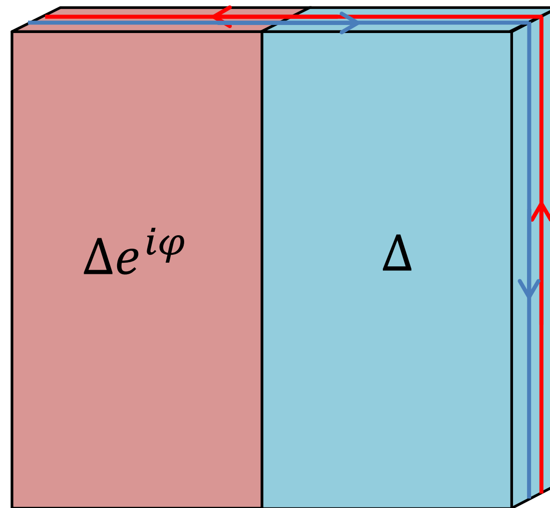

Fig. 4.14: A simplified geometry used in the simulations to recreate the physics of the geometry in Fig. 3.6a).

Firstly the eigenvalues and eigenvectors of a thin film with open boundary conditions in 3 dimensions are calculated. Using a sparse matrix diagonalization method, only the eigenvalues close to the Fermi level are calculated. In the 6 orbital model a 7 atml thick $[111]$ thin film and a 3 atml thick $[001]$ thin film were simulated. By calculating the dispersions it was checked that these thin films also have 1 and 2 Dirac cones per BZ respectively, as was already found using the 18 orbital model in section 2.4. Since the whole geometry is made superconductive by the method discussed in section 3.3.1 no states should exist in the superconducting gap, except in the case of Majorana states. Fig. 4.15a) and 4.16a) show the energy dispersions of the normal states of the $[111]$ and $[001]$ thin films as calculated with the 8 orbital model. For the $[111]$ thin film there is a discrepancy

compared to the 18 orbital calculations (section 2.4) in that the bandgap is much smaller at $k = \pm\pi$. Therefore care must be taken that the Fermi level is set within this gap.

In Fig. 4.15b) and 4.16b) the energy dispersion are shown for the superconductive state. $\Delta = 2\ \mathrm{meV}$ was set for the $[111]$ film and $\Delta = 20\ \mathrm{meV}$ for the $[100]$ film, which are both much bigger values than for typical induced superconductivity (see table 2.1). It was found that large superconductive order parameters Δ are needed so that the Majorana wavefunctions are less delocalized. Since the width of the thin film is only finite the Majorana wavefunctions can overlap, resulting in a energysplitting in the spectrum. This energy splitting can thus be decreased by either increasing the width of the thin film (which is computationally expensive) or by increasing Δ. In Fig. 4.15c) and Fig. 4.16c) zoom-ins of the dispersion near the Dirac points are shown. On top of that the eigenvalues of a thin film finite in 3D is plotted, where the finite thin film has the same cross-section as was used for the dispersion calculation. It seems that Majorana states exist in the middle of the superconducting gap.

For the $[111]$ thin film there are 4 states in the gap (two degenerate states at positive and two degenerate states at negative energy). This can be understood because at both sides of the QSHI, which has 1 Dirac cone, two Majorana fermions exist at the π-junction. For the $[001]$ film 8 states are present inside the superconducting gap, which is because there are 2 Dirac cones on the edge of the thin film, which is double the number of Dirac cones compared to the $[111]$ thin film. In Fig. 4.15d) and 4.16d) the wave function probability density summed over the 4 and 8 midgap states are shown respectively. For the $[111]$ thin film the Majorana seems to be located on the two ends of the π-junction (top and bottom of the figure), however probably since the geometry and the superconducting order parameter Δ are not big enough the Majorana wavefunctions are not well localized. Therefore the Majorana fermions also extended partly over the edge of the thin film. For the $[001]$ thin film a larger Δ was chosen, therefore more localized Majoranas, 4 at each end, seem to exist on the ends of the π-junction. The 8 midgap states consist of 4 states at positive and 4 states at negative energies. The 4 states are not all degenerate, but degenerate in pairs of two.

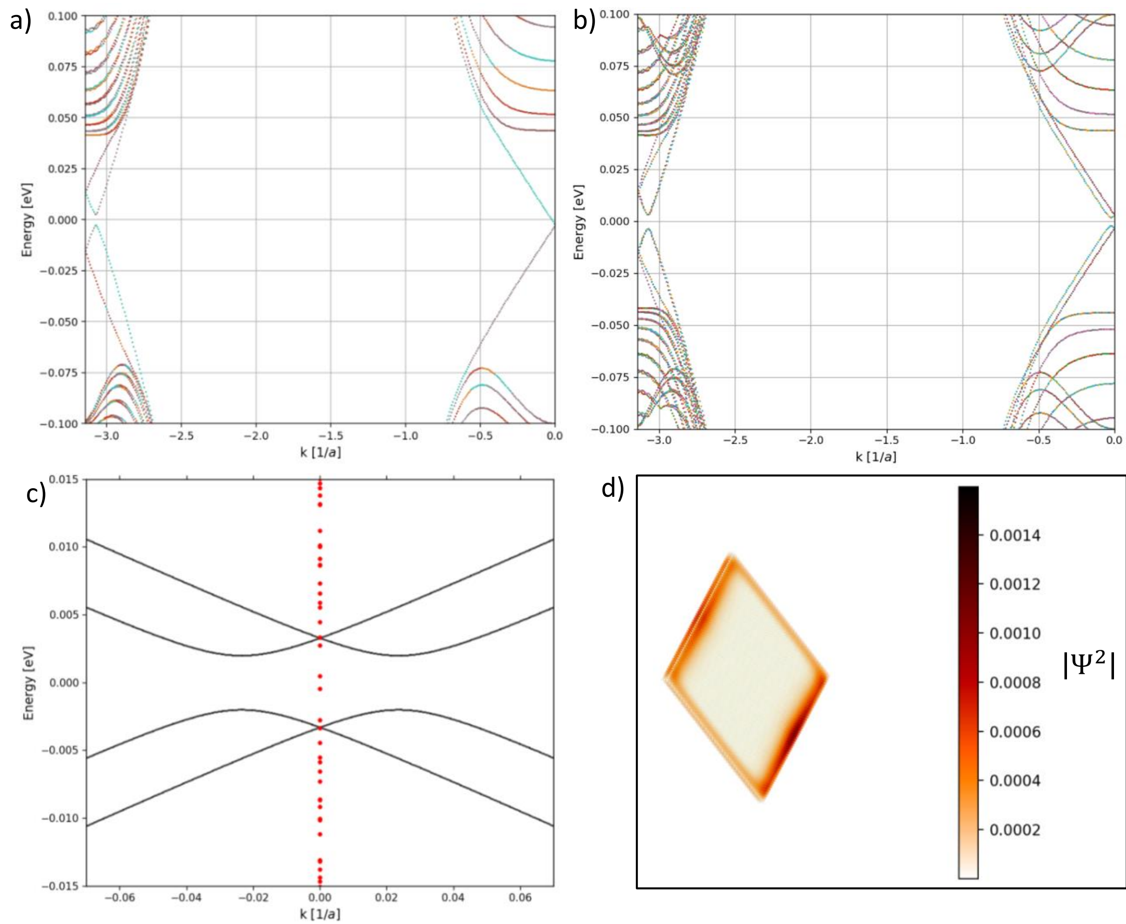

Fig. 4.15: $[111]$ *thin film dispersion without (a) and with (b) superconductivity with order parameter* $\Delta = 2\ \mathrm{meV}$. *(c) In black a zoom-in of the dispersion of Fig. 4.15b) near zero energy and* $k = 0$ *and in red the eigenvalues of a thin film finite in 3D of* $121 \times 241 \times 7$ *atml (d) Wave function probability density summed over the 4 midgap states.*

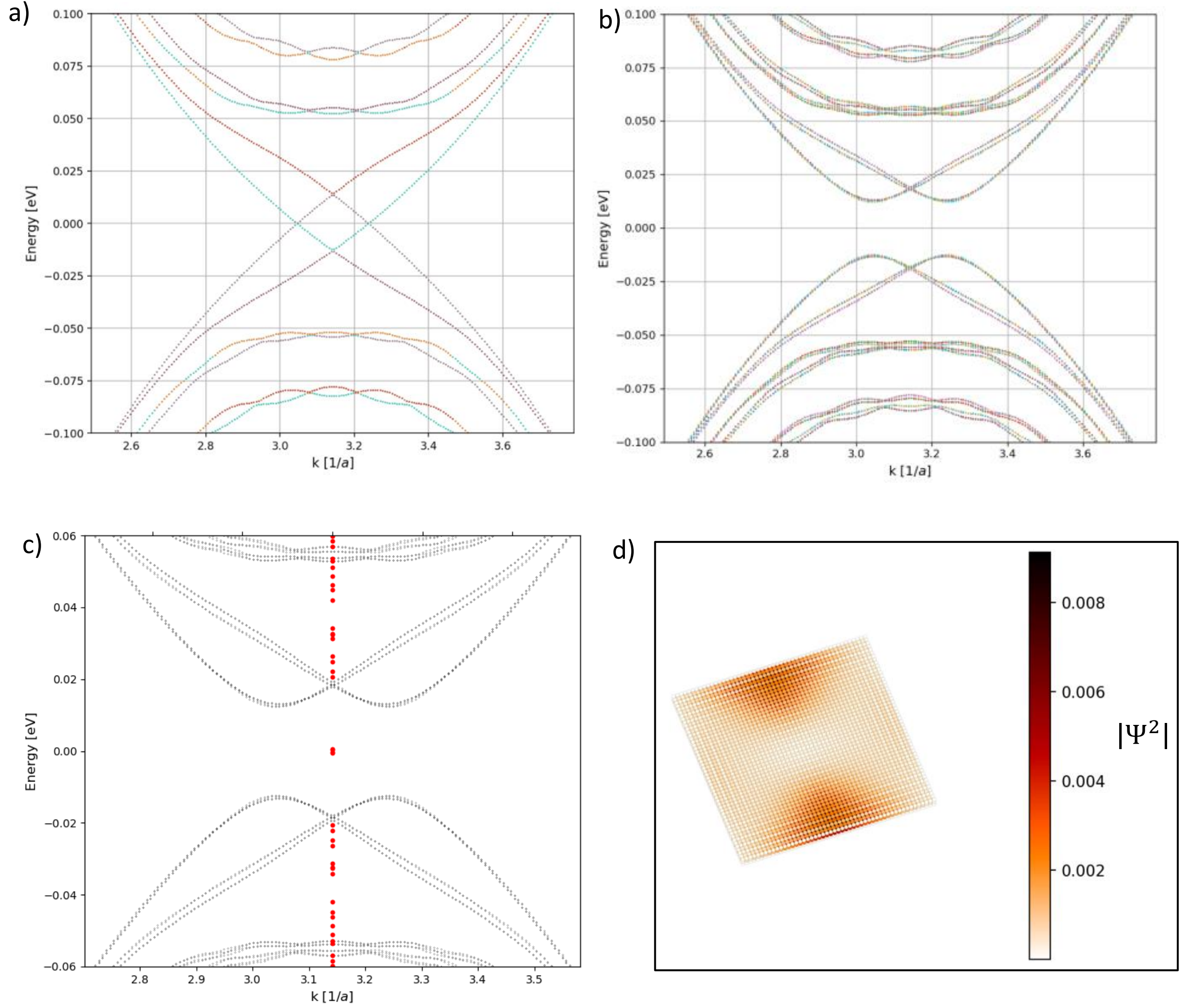

Fig. 4.16: $[001]$ *thin film dispersion without (a) and with (b) superconductivity with order parameter* $\Delta = 20$ meV. *(c) In black a zoom-in of the dispersion of Fig. 4.16b) near zero energy and* $k = 0$ *and in red the eigenvalues of a thin film finite in 3D of* $51 \times 51 \times 3$ *atml (d) Wave function probability density summed over the 8 midgap states.*

Further evidence that the actual states plotted in Fig. 4.15d) and Fig. 4.16d) really are Majorana fermions could have been acquired in two ways. First of all a topological invariant can be defined and calculated to check whether the system is in a topological Majorana state. For Rashba-spinorbit nanowires the existence of Majorana fermions on its two ends is verified by calculating the product of the Pfaffians at $k = 0$ and $k = \pi$, i.e.

$$\mathrm{Pf}[iH(0)]\mathrm{Pf}[iH(\pi)]. \tag{3.4}$$

If this so-called Majorana topological invariant is equal to -1 the system is topological, while for a value of 1 the system is trivial. The Pfaffian computes the fermion parity at a particular k-value. Therefore if a band inversion is present at one of the $k = 0$ or $k = \pi$ this induces a parity switch resulting in a change of sign of the Majorana topological invariant. The topological invariant was calculated for the geometry shown in Fig. 4.17, both for the $[111]$ and $[001]$ thin films. A cross-section of the thin film including the π-junction with periodic boundary applied in the direction

perpendicular to the cross-section is simulated. For both films $\mathrm{Pf}[iH(0)]\mathrm{Pf}[iH(\pi)] = 1$, indicating a trivial system.

However, this does not necessarily mean that no Majorana fermions are present. Similarly to the situation investigated in ref. 14, multiple Majorana modes located at the same position may be topologically protected by mirror symmetries of the system. The fact that these modes are degenerate to a high precision hints at such a scenario. We leave the question of defining a different topological invariant that captures the non-trivial nature of the 2 or 4 Majorana modes at each end of the junction to future work.

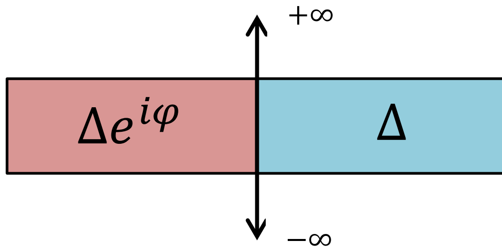

Fig. 4.17: Simulated geometry for the Majorana topological invariant of a thin film.

Another approach to prove the existence of the Majoranas would be to do conductance calculations. This could be done in a tunneling geometry similar as is shown in Fig. 3.1. A different approach proposed in literature proves the existence of Majorana fermions by calculating the conductance through a normal metal/QSHI/superconductor junction. As Fig. 4.18 shows a Andreev quantum dot is created by a gate electrode at the edge of a QSHI in a prependicular magnetic field B. A current I is passed between metallic and superconducting contacts, and the differential conductance $G = dI/dV$ is measured as a function of the bias voltage V for different gate voltages. By averaging G over the different gate voltages a zero-bias peak appears with a height of $4e^2/h$ above a $\left(\frac{2}{3}\pi^2 - 4\right)e^2/h$ background.

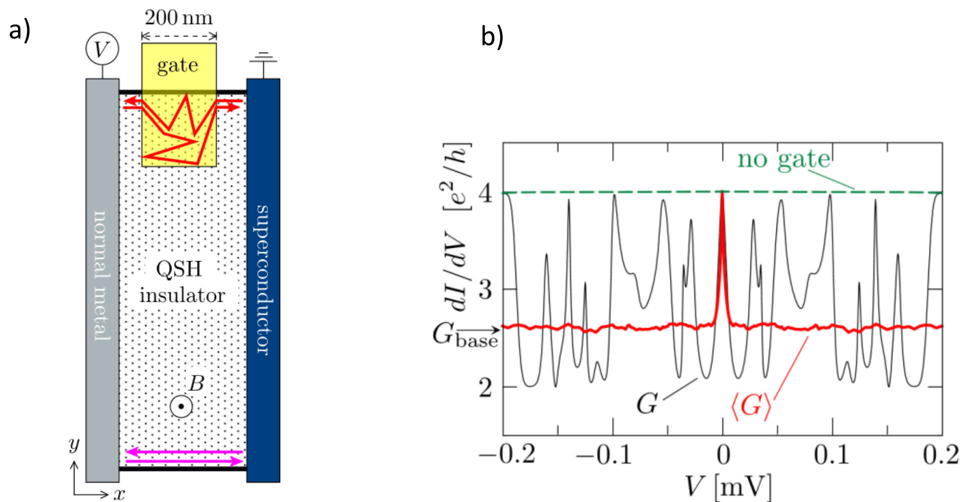

Fig. 4.18: (a) Andreev quantum dot setup. (b) Conductance as a function of bias voltage V for a gate voltage of $E_c = -1.5$ meV (black line), conductance as a function of bias voltagae V averaged over different gate voltage (red line) and conductance curve without gate electrode (green line). Reproduced from ref. 15.

To calculate the conductance of a thin film in the Kwant python package, leads are connected to a scattering region, which for the $[111]$ thin films is taken to be of size $61 \times 7 \times 3$ atml. First Kwant's conductance calculation would not converge, which was solved by applying a small electric field of $0.1\ \mathrm{meV/atml}$ perpendicular to the tin film. Fig. 4.19 shows the both the result of the conductance calculation in units of e^2/h as well as the energy dispersion of the corresponding $61 \times 7 \times \infty$ atml thin film. The conductance calculation took about 355s per calculation point to converge, while identical but superconducting thin film would take about 2790s per calculation point. If then also an ensemble average over these calculations would have to be done then this would be a too expensive calculation given the limited time on the multi-user cluster on which the computation was performed.

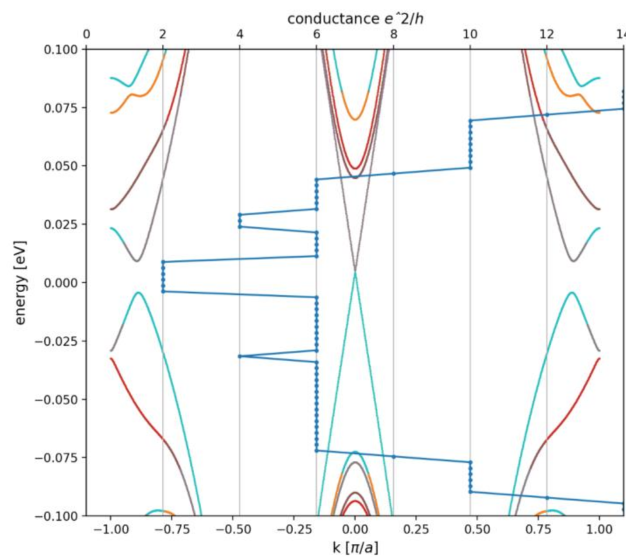

Fig 4.19: Conductance calculation of a $[111]$ *film of* 61×7 *atml (blue dotted line) on top of the film's dispersion.*

Due to the long computation times of the conductance, the thin film conductance was not further investigated. An effective model should be formulated to reduce the computation times.

4.3. SnTe nanowire growth results

4.3.1 High temperature growth ($250 \leq T_B \leq 450$ ℃)

This section discusses the growth results of the first 18 growth runs, in which BandiT temperatures were between $T_B = 250$ °C and $T_B = 450$ °C. For growth runs at 400 °C the Sn flux was mostly set at $p_{Sn} = 3.5 \cdot 10^{-7}$ Torr, while a Te series was done in the range $p_{Te} = 2.8 \cdot 10^{-7} - 22 \cdot 10^{-7}$Torr. The growth time was 30 min for most growth runs. As the SEM images in Fig. 4.20 show, at this temperature mostly droplets of material were deposited. These droplets contain mostly Sn and, at places where there is Au present, a Au_xSn_y alloy. SnTe is probably not deposited, at least not in big quantities, since not much characteristics of crystalline growth are found. From Fig. 4.20 it is clear that for low Te fluxes much more material is deposited than for the high Te fluxes. This could be due two effects. First of all due to a high Te flux, more SnTe can be formed, depositing effectively less elemental Sn. As can be seen in Fig. 5.1, at 400 °C the reevaporation rate of SnTe is about 0.02 ML/s, while Sn has a negligible reevaporation rate. However, because this reevaporation rate is small, a more influential effect could be due to a possible surfactant effect of Te. It could be that Te actually passivates the substrate, so that Sn cannot stick to it and in total less material is deposited.
Finally from Fig. 4.20c is can be seen that nucleation seems to occurs for the high Te fluxes. Here the gold particles in the lithographic array of holes clearly have picked up material, which could be Sn or SnTe.
Fig. 4.21 shows the result of growth runs at the slightly lower temperature of $T_B = 340$ °C. At this temperature and $p_{Te} = 5.0 \cdot 10^{-7}$Torr a Sn series was done in the range of $p_{Sn} = 3.5 \cdot 10^{-7} - 0.77 \cdot 10^{-7}$Torr. The results are very similar as at 400 °C, namely droplets of probably mostly Sn are deposited. Besides that decreasing the Sn flux has a similar effect as increasing the Te flux. Moreover, as can be seen in Fig. 7.2, nucleation occurs again for the lowest Sn fluxes at 340 °C, similarly as was the case for the high Te fluxes at 400 °C in Fig. 4.20.

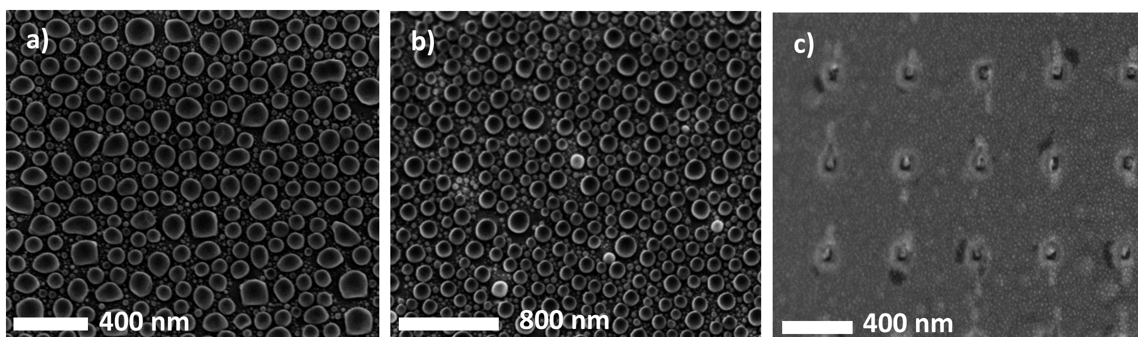

Fig. 4.20: SEM images of SnTe growth runs at 400 °C. *The Sn flux* $p_{Sn} = 3.5 \cdot 10^{-7}$ Torr *and the Te flux is varied such that a)* $p_{Te} = 2.8 \cdot 10^{-7}$ Torr *b)* $p_{Te} = 8.0 \cdot 10^{-7}$ Torr *and c)* $p_{Te} = 22 \cdot 10^{-7}$ Torr. *(a) is on a patterned* SiN_x *mask on GaAs substrate, while (b) and (c) are on a a patterned* SiN_x *mask on Ge substrate. Magnifications are (a) 50 KX, (b) 70 KX, (c) 112 KX.*

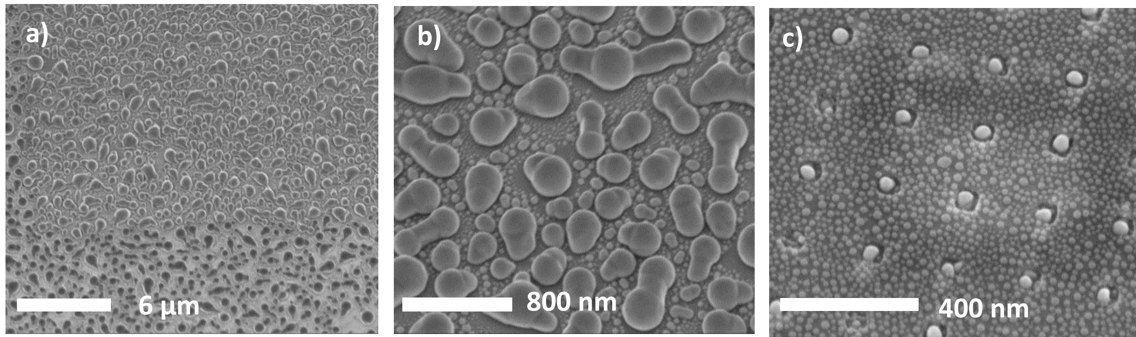

Fig. 4.21: SEM images of SnTe growth runs at $340\ ^\circ\mathrm{C}$. *The Te flux* $p_{Te} = 5.0 \cdot 10^{-7}\ \mathrm{Torr}$ *and the Sn flux is varied such that a)* $p_{Te} = 3.5 \cdot 10^{-7}\ \mathrm{Torr}$ *b)* $p_{Te} = 2.2 \cdot 10^{-7}\ \mathrm{Torr}$ *and c)* $p_{Te} = 0.77 \cdot 10^{-7}\ \mathrm{Torr}$. *(a) and (b) are on a patterned* SiN_x *mask on GaAs substrate, while (c) is on a a patterned* SiN_x *mask on Ge substrate. Magnifications are (a) 10 KX, (b) 70 KX, (c) 200 KX.*

A big difference in surface morphology can be seen for even lower growth temperatures, as is shown in Fig. 4.22. More film-like, but polycrystalline growth is observed for temperatures of $250\ ^\circ\mathrm{C}$ and $300\ ^\circ\mathrm{C}$.

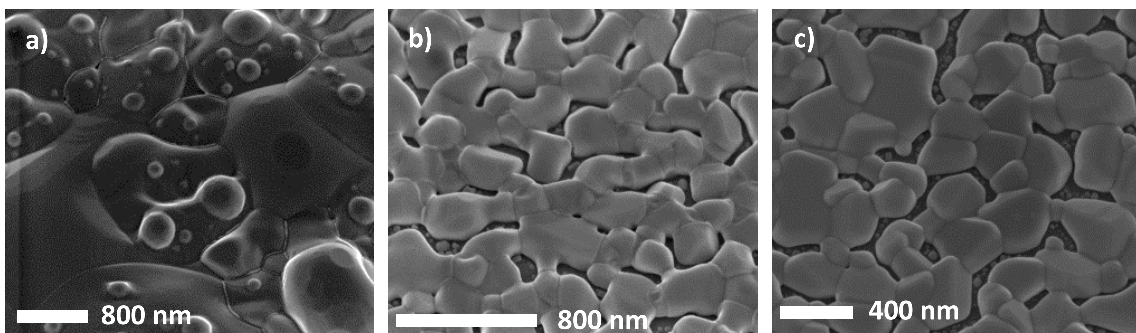

Fig. 4.22: SEM images of SnTe growth runs at (a) $303\ ^\circ\mathrm{C}$, $p_{Sn} = 3.5 \cdot 10^{-7}\ \mathrm{Torr}$, $^\circ\mathrm{C}$, $p_{Te} = 3.1 \cdot 10^{-7}\ \mathrm{Torr}$ *(b)* $300\ ^\circ\mathrm{C}$, $p_{Sn} = 1.3 \cdot 10^{-7}\ \mathrm{Torr}$, $^\circ\mathrm{C}$, $p_{Te} = 5.0 \cdot 10^{-7}\ \mathrm{Torr}$ *(c)* $250\ ^\circ\mathrm{C}$, $p_{Sn} = 0.77 \cdot 10^{-7}\ \mathrm{Torr}$, $^\circ\mathrm{C}$, $p_{Te} = 5.0 \cdot 10^{-7}\ \mathrm{Torr}$. *(a) and (c) are on a* SiN_x *gradient on GaAs substrate, while b) is on a patterned* SiN_x *mask on a Ge substrate. (a) has a growth time of 60 min, while (b) and (c) have a growth time of 30 min. Magnifications are (a) 50 KX, (b) 100 KX, (c) 100 KX.*

4.3.2 Low temperature Au-catalyzed SnTe nanowires

Growth 19 with $T_B = 210$ °C was the first growth run on which a considerable amount of nanowires was produced. The growth time was 30 minutes and the fluxes $p_{Sn} = 7.7 \cdot 10^{-8}$ Torr and $p_{Te} = 5.00 \cdot 10^{-7}$ Torr. The nanowires are found on Ge (110) and GaAs (001) substrates with a patterned 10 nm SiN_x mask with 8 nm thick gold particles. However the nanowires do not grow on the patterned gold particles in the holes of the mask. The nanowires only grow in specific areas of the substrate, namely on the EBL dose markers and on the hole arrays with lift-off problems. These areas contain a larger density of gold (but approximately equal thickness) with a rough morphology.
The growth procedure was simple: The substrate is heated up to 210 °C, then the Te and Sn cells are opened for 30 min and after closing them again the substrate is cooled down to room temperature.
It could be that the wires grow during cooldown, due to strain effects. However this is not likely because not a closed film is grown under the wires as reported for PbTe wires[16], but a polycrystalline layer that can easily relax stresses. Similar results were obtained for a substrate temperature of 230 °C, while for 250 °C less nanowires where found.

The results after growth are shown in the SEM images in Fig. 4.23. In Fig. 4.23a) a zoom-out view is shown of a collection of hole-arrays. In the top the overgrown EBL dose-marker is shown. On the bottom the 2 hole-arrays (one for a hole-size of 50 nm and one for 40 nm) show overgrown bad-liftoff (resist stripping) areas where a large density of gold is present. As could be seen from the EBL design in Fig. 6.2, between the dose marker and these array are also arrays of holes, but these are fully overgrown. A zoom-in of the bottom 50 nm hole-size /250 nm pitch array is shown in Fig. 4.23b). Typically tens of nanowire can be found per field, only growing in the white areas where Au is present. SEM images of wire are shown in Fig. 4.23c) to Fig. 4.23f). Nanowires are in the range of $20 - 50$ nm in diameter and have lengths varying from several nanometers to about 2 μm, of which an example is shown in Fig. 4.23f). The height of structures should be taken about 2 times as high as measured in the SEM image. This is because the sample holder in the SEM is tilted $30°$. However since nanowires are growing under an angle the actual length should be scaled by a factor somewhat smaller than 2. Some nanowires seems to nucleate at the substrate, which can be on the Ge or GaAs substrate and on the SiN_x mask, as shown in Fig. 4.23c). Others are growing along the facet of a SnTe single crystal, as is shown in Fig. 4.23d) and e). The length of the wires varies a lot, as can be seen in Fig. 4.23f) where a long wire of about 2 μm can be seen and wires of about 200 nm.

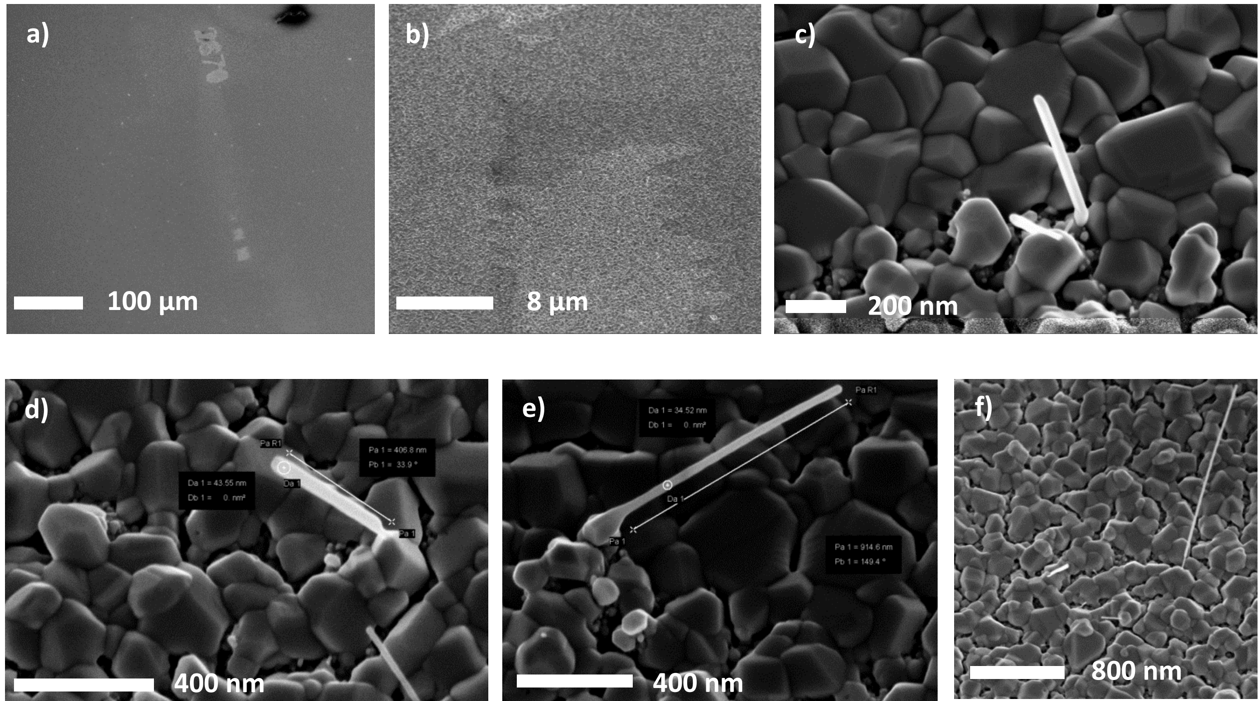

Fig. 4.23: SEM images of the first SnTe nanowires grown in MBE. (a-b) Zoomed-out view of the areas where nanowires grown. (c) Nanowire emerging from the substrate. (d-e) Nanowires emerging from SnTe single crystals. (f) SEM image showing the size non-uniformity. Magnifications are (a) 390 X, (b) 6.51 KX, (c) 178 KX, (d) 190 KX, (e) 170 KX and (f) 56 KX.

Next transmission electron microscopy (TEM) was done to determine the amount of defects and the stochiometry or chemical composition of the nanowires.Therefor some of the wires were transferred to a holey carbon TEM grid, as Fig. 4.24 shows for a wire which has a crystal at its base. In Fig. 4.24b) a zoomed-out TEM image shows that the wire is heavily bended, which happened while putting it on the TEM grid. The bending is indicated by dark interference fringes on the nanowire. In Fig. 4.24c) and d) it can be seen that the holes are present in the wire. Outside of the holes a seemingly defect free single crystal is observed. From Fig. 4.24d) the lattice constant is estimated to be $0.635\ \mathrm{nm}$, which corresponds very well to the value of $0.633\ \mathrm{nm}$ found in literature[17].
To further investigate the vacancies in the nanowire energy-dispersive X-ray spectroscopy (EDX) is performed on the same area. Fig. 4.25a-d) show the EDX maps for Sn, Te, Au and O. EDX has different sensitivities for each element. Therefore the relative contrast between elements in Fig. 4.25 does not give any information. However non-uniformities in the distribution of each element can be observed. First of all it is clear that Au is spread all over the nanowire. Secondly in the vacancy of Fig. 2.4d) it can be seen in Fig. 4.25 a) and c) that in these areas there is a very low density of Sn and Au. Moreover the densities of Te and O seem to be distributed uniformly, they are not lower in the 'vacancies'. This means that the vacancies are probably actually not empty, but filled with Te and O.
Besides that from Fig. 2.24d) it can be seen that there is a rocksalt structure, but that the crystal is rotated $45°$ with respect to the direction out of the paper. From this we can derive that the nanowire is actually growing in the $(1-10)$ direction. The TEM is then taken by looking in the (001) direction and the facets on the left and right would be (110) facets. That is, if the crossection of nanowire is rectangular and if the nanowire actually has clear facets. In SEM the crosssection

could not be checked due to the small cross-section and random orientation of the nanowires.The observation that the nanowire grows in the $\{110\}$ direction is peculiar, since the (001) facet is reported to be the lowest energy surface. Finally, to our knowledge no SnTe nanowires with (partial) $\{110\}$ side facets have been reported. Therefore we would expect that the nanowire would have (001) facets.
From this could also be understood why the vacancies are actually forming. The vacancies seem to form facets within the nanowire under an angle of $45°$ compared to the growth direction. This means that the facets within the vacancy are actually $\{001\}$ facets. The vacancies could thus be formed because they expose facets which minimize energy compared to the $\{110\}$ facets. However the uniform distribution of Te in 4.25b) is puzzling.

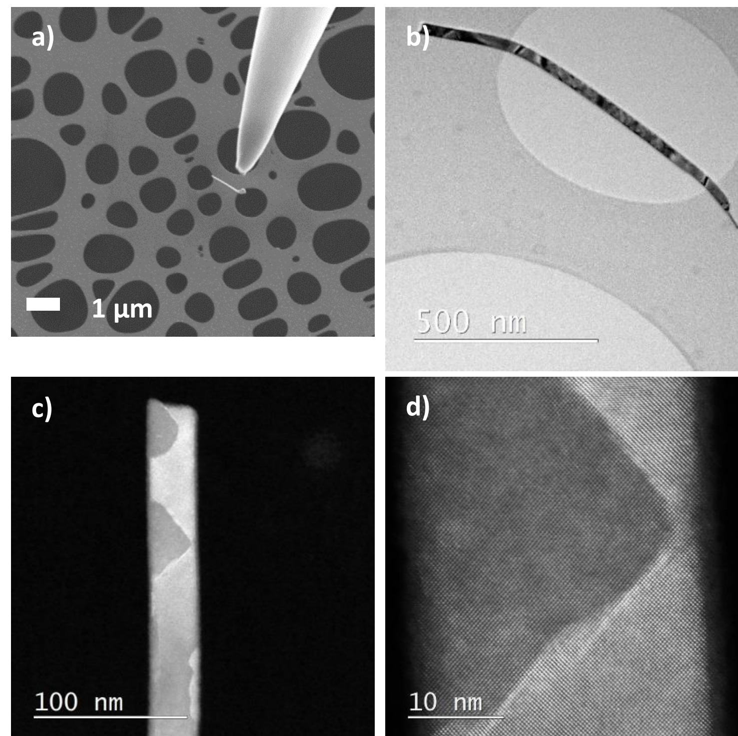

Fig. 4.24: (a) SEM image of a Au catalyzed SnTe nanowire transferred to a holey carbon TEM grid. (b-d) TEM images of some of the SnTe nanowires.

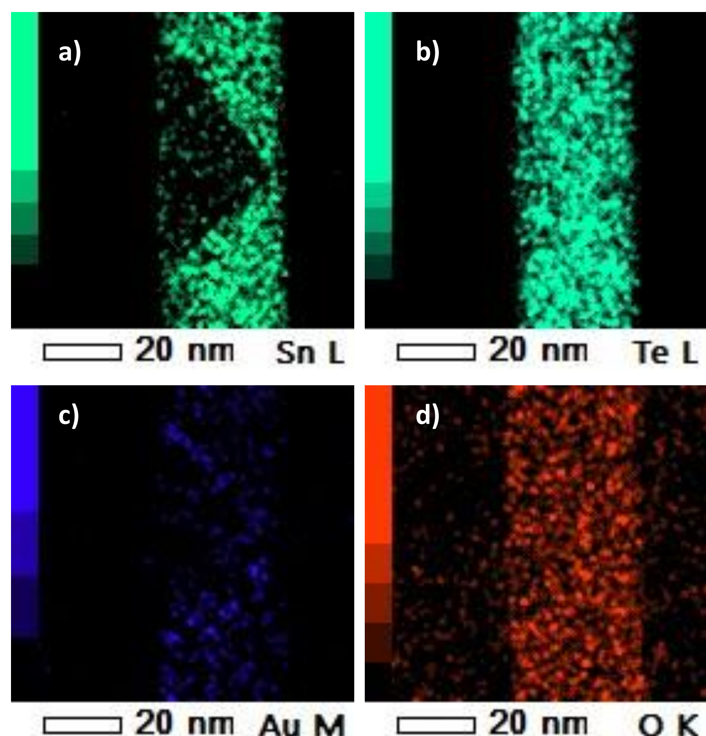

Fig. 4.25: EDX maps in arbitrary unit (AU) of the area of Fig. 4.24d) showing a uniform distribution of Te and O_2 at this section of the wire. But a vacancy in the wire with low concentrations of Sn and Au.

In TEM images of different nanowires from the same sample it can also be seen that Au is spread over the surface of the wire. This gold would completely break the symmetry of lattice, thereby destroying the TCI gapless surface states on the surface facets of the nanowire (if facets can be grown). This is illustrated by Fig. 4.26. In Fig. 4.26a) the nanowire is shown with the growth direction downwards. Fig. 4.26b) show a high constrast in the bottom part of the wire, which is most probably a Au particle. The Au diffuses along the edge of the nanowire indicates by the black rim originating at the Au particle. Besides that on the top of the wire shown in Fig 4.26c) the black contrast at the right side corresponds to gold, as confirmed by the EDX map in Fig. 4.26d). Fig. 4.26e-f) show that the Sn concentration is reduced at the location of the gold, while this effect is less clear for the Te.

The spreading of Au over the surface of the nanowire is probably caused by interaction of the gold particle at the top of the nanowire with the parasitic SnTe growth around the nanowire. For example the parasitic growth could destabilize the gold particle at the top of the growing nanowire, thereby incorporating the gold in its surface.

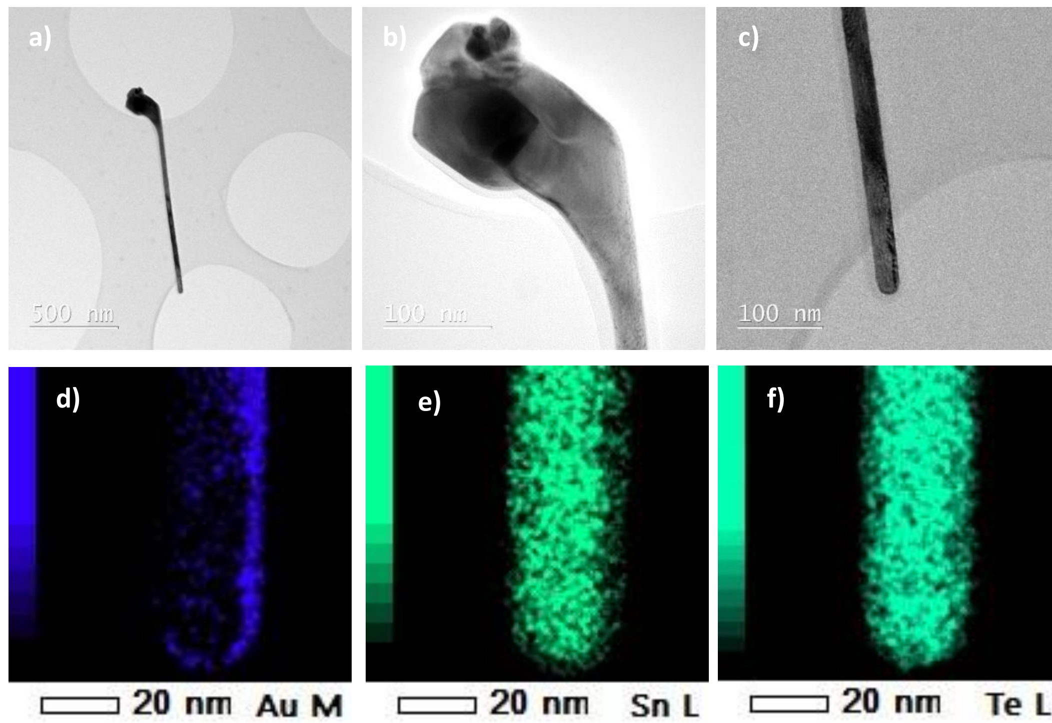

Fig. 4.26: TEM images of a different nanowire of growth 19, showing (b) the bottom of the wire and (c) the top of the wire. The EDX maps of the top of a nanowire for (d) Au, (e) Sn and (f) Te are shown.

4.3.3 Growth time series

In this section the effect of changing the growth time is studied, while keeping the other growth parameters of growth run 19 the same. Besides a growth time of 30 minutes, growth times of 2, 5, 10 and 120 minutes were studied, for which Fig. 4.27 shows SEM image taken from patterned Ge substrates. From Fig 4.27c) for 10 minutes can be seen that for shorter growth times the parasitic growth is still there to an almost equal extent as for 30 minutes growth, as shown in for example Fig. 7.4f). However a big difference is that the numbers of wires is much bigger for 10 minutes of growth. Moreover that the wires are much smaller than for 30 minutes growth, having lengths no longer than about 400 nm. As Fig 4.27b) shows, for 5 minutes growth the nanowire are even smaller and appear again in larger numbers. For 2 minutes growth parasitic growth is observed again, but no nanowires are grown as shown in Fig. 4.27a). The amount of deposited material is minimal, as the Au particles in the EBL dose marker are still clearly visible. Finally for 2 hour growth no nanowires are found. This is probably because the nanowires are completely covered by the parasitic growth, as can be seen in Fig. 4.27d). The substrate is coved with a polycrystalline SnTe layer.

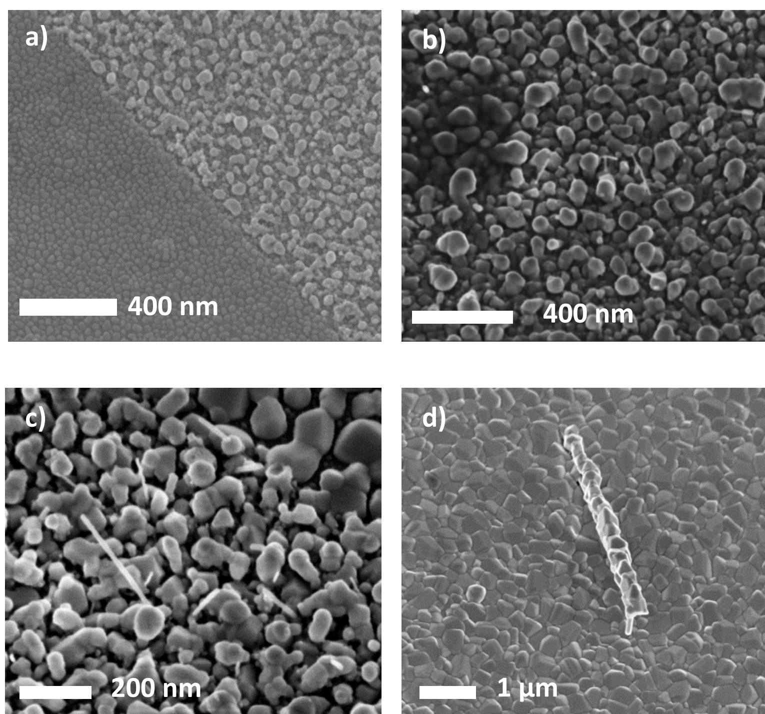

Fig. 4.27: SnTe growth for different growth time (a), 2 (b) 5, (c) 10 and (d) 120 minutes. The substrate temperature is the same as growth run 19 210 °C, *likewise for the fluxes again* $p_{Sn} = 7.7 \cdot 10^{-8}$ Torr *and* $p_{Te} = 5.00 \cdot 10^{-7}$ Torr. *Magnifications are (a) 136 KX, (b) 166 KX, (c) 229 KX and (d) 33 KX.*

4.3.4 Sn and Te flux series

This section discusses the effect of changing the Sn and Te fluxes with respect to the growth parameters of run 19 (discussed in section 7.2). The $210\ ^{\circ}\mathrm{C}$ substrate temperature of growth 19 was pursued, where eventually all substrate temperatures were in the range of $T_B = 193 - 224\ ^{\circ}\mathrm{C}$. For growth 19 $p_{Sn} = 7.7 \cdot 10^{-8}$ Torr and $p_{Te} = 5.00 \cdot 10^{-7}$ Torr $\left(\frac{\mathrm{IV}}{\mathrm{VI}} = 0.15\right)$, however now fluxes were varied in the range of $p_{Sn} = 5.4 \cdot 10^{-9} - 1.3 \cdot 10^{-7}$ Torr and $p_{Te} = 2.2 \cdot 10^{-6} - 5.4 \cdot 10^{-9}$ Torr. Mostly a growth time of 30 min was maintained so that parasitic growth does not dominate over nanowire growth. In Fig. 4.28 results are shown of changing one of the fluxes with respect to growth 19. Increasing the Sn flux and/or decreasing the Te flux does not result in nanowires, as is shown in Fig. 4.28b) and c), however decreasing the Sn flux or increasing the Te flux gives a low density of nanowires, similarly as was observed in growth 19. This suggests that a low IV/VI ratio promotes nanowire growth.

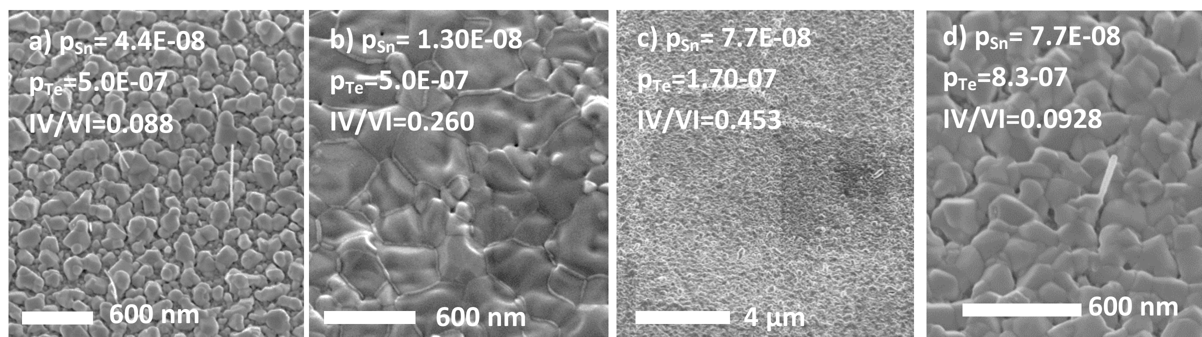

Fig. 4.28: The effect of changing the Sn and Te fluxes with respect to growth run 19. Substrate temperatures are in the range of $193 - 224\ ^{\circ}\mathrm{C}$. *Fluxes and IV/VI ratios are indicated. a) less* Sn *b) more* Sn *c) less* Te *d) more* Te. *Magnifications are (a) 72 KX, (b) 91 KX, (c) 14 KX, (d) 111 KX.*

The growth changed considerably when the IV/VI ratio was lowered even more to a range of IV/VI $= 0.035 - 0.077$. Now the nanowire growth is not only limited to substrate parts where gold is present, like the EBL dose markers and the lithographically patterned arrays, but nanowire growth is present equally everywhere on the substrate. The edges of a $\mathrm{Au/SiN_x}$ lithographic pattern (4.29a)) and edge of a EBL dose marker with gold (4.29b)) show that nanowires occur independently of the availability of gold (growth time is still 30 mi. In Fig. 4.29c) similar results are shown as in 4.29a) but then for a slightly different Te flux.

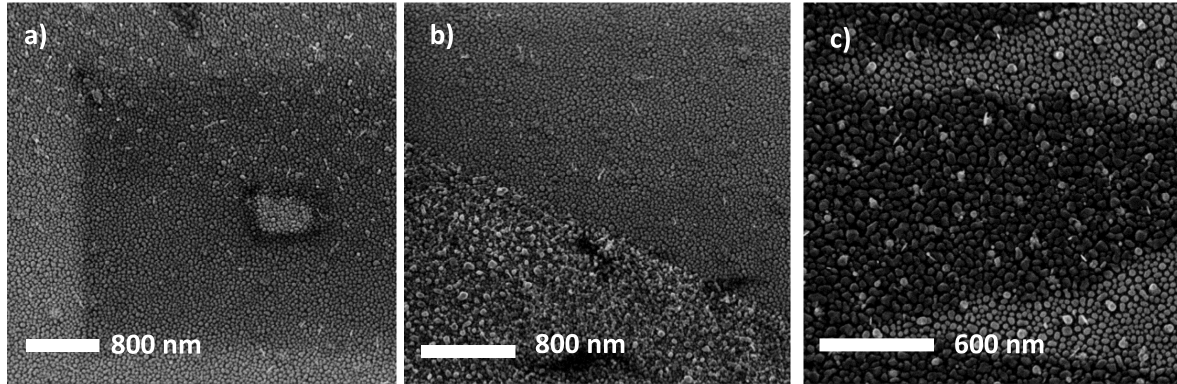

Fig. 4.29: Nanowire growth for low $\mathrm{IV/VI}$ ratios *(a) at the edge of a* $\mathrm{Au/SiN_x}$ *lithographic pattern, (b) at the edge of a EBL dose marker with gold. Fluxes for (a) and (b) are* $p_{Sn} = 1.0 \cdot 10^{-8}$ Torr, $p_{Te} = 2.90 \cdot 10^{-7}$ Torr and $\mathrm{IV/VI} = 0.035$*. For (c)* $p_{Sn} = 1.0 \cdot 10^{-8}$ Torr, $p_{Te} = 1.3 \cdot 10^{-7}$ Torr *and* $\mathrm{IV/VI} = 0.077$. *The growth time is 30 minutes.*

More growth times were investigated, using the same fluxes as Fig. 4.29c. For 30 min (Fig. 4.29c)) and 1 hour (Fig. 4.30a)) the density of nanowires per area is quite small. Lengths of the nanowires for 1 hour growth are typically $300 - 500$ nm and diameters are found to be $10 - 20$ nm. With a longer growth time of 2 hours (Fig. 4.30b) the density is even lower. Parasitic deposits of SnTe bury the wires during growth. Still nanowires were found with a much bigger size (Fig. 4.30d)) than for shorter growth times. These nanowires unfortunately did not grow everywhere, as they grew in areas that seemed to be scratched before growth (Fig. 4.30c)), either during cleaving, substrate processing or mounting. The scratches can be recognized by a different morphology is the parasitic film growth and a higher contrast in SEM. The film in the scratch is polycrystalline instead of monocrystalline islands. For these samples no intentional catalyst was deposited on the Si (111) substrate. Except for BHF cleaning of 30 s no wet chemistry or plasma cleaning was done to minimize the amount of contaminants. However particles may still have been deposited on the substrate during the cleaving process, tweezer handling or during substrate mounting (indium).

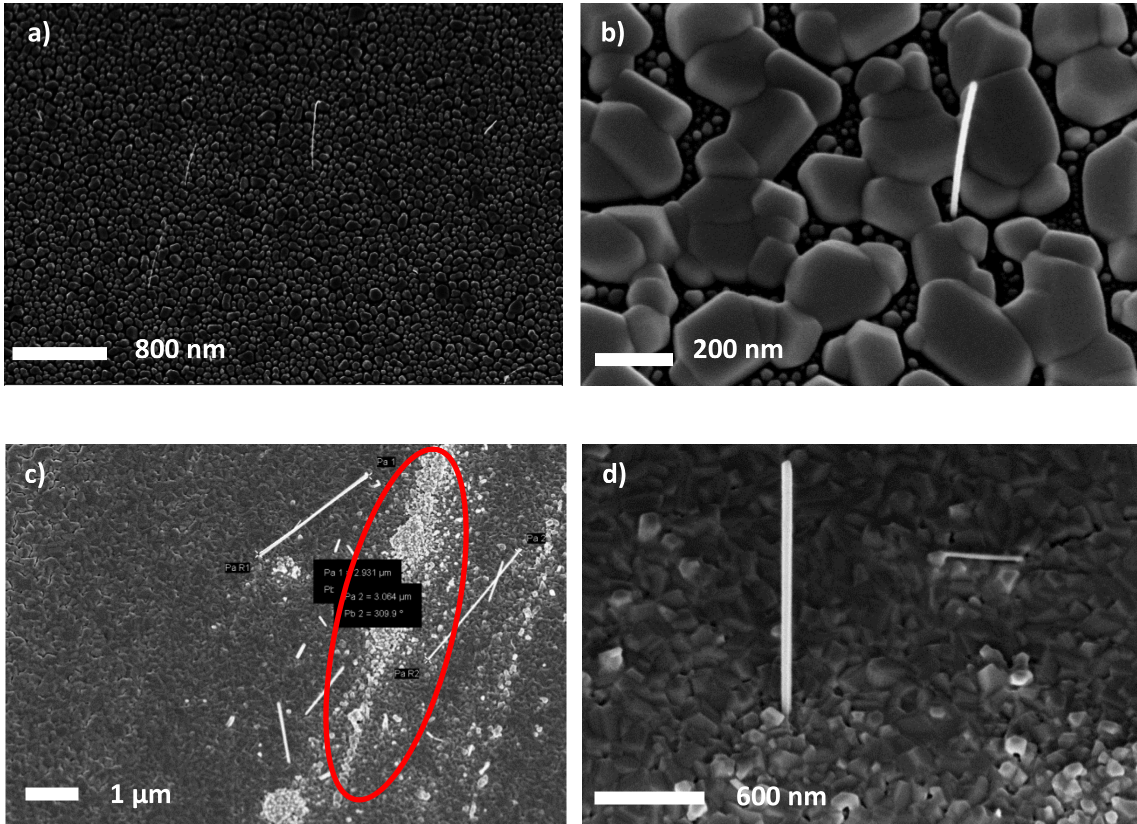

Fig. 4.30: Nanowire growth for growth times of (a) 1 hour and (b-c-d) 2 hours for $p_{Sn} = 1.0 \cdot 10^{-8}$ Torr, $p_{Te} = 1.3 \cdot 10^{-7}$ Torr *and* $\mathrm{IV/VI} = 0.077$. T_B *is in the range* $205 - 216$ °C. *On (a) unprocessed* Si (111) *and (b-c) on* Si (111) *cleaned with BHF for 30 s. (c-d) Wires found at a scratched part of the sample, indicated by a red marker.*

The nanowires, grown with a flux ratio of $\mathrm{IV/VI} = 0.077$ and growth times of 1 and 2 hours, are investigated in TEM and EDX. Multiple images were taken in TEM. In TEM the viewing angle is aligned with a certain crystalline direction called the zone axis. Since the TEM projects the 3D crystal along the viewing line onto one 2D image it is hard to see whether facets are presents or not, however different zone axes can be observed. From Fourier transformation of the TEM images the growth direction of some investigated wires was found to be $\{110\}$, also a growth direction of $\{112\}$ was found. SEMs along different directions were taken such as $\{001\}$, $\{112\}$, $\{1\text{-}11\}$ and $\{0\text{-}2\ 2\}$ zone axes. For example the $\{0\text{-}2\ 2\}$ and $\{1\text{-}11\}$ and zone axes were studied, for which the TEMs images are shown in Fig. 4.31a) and b) respectively. The difference in viewing angle is $35.26°$ with respect to the $\{011\}$ axes. The insets show a 3×3 cube of SnTe which is rotated so the zone axis of the crystal structure is the same as the viewing angle of the TEM. Finally Fig. 4.31c) shows a TEM image of the same nanowire showing areas with different contrast which indicate defected regions.

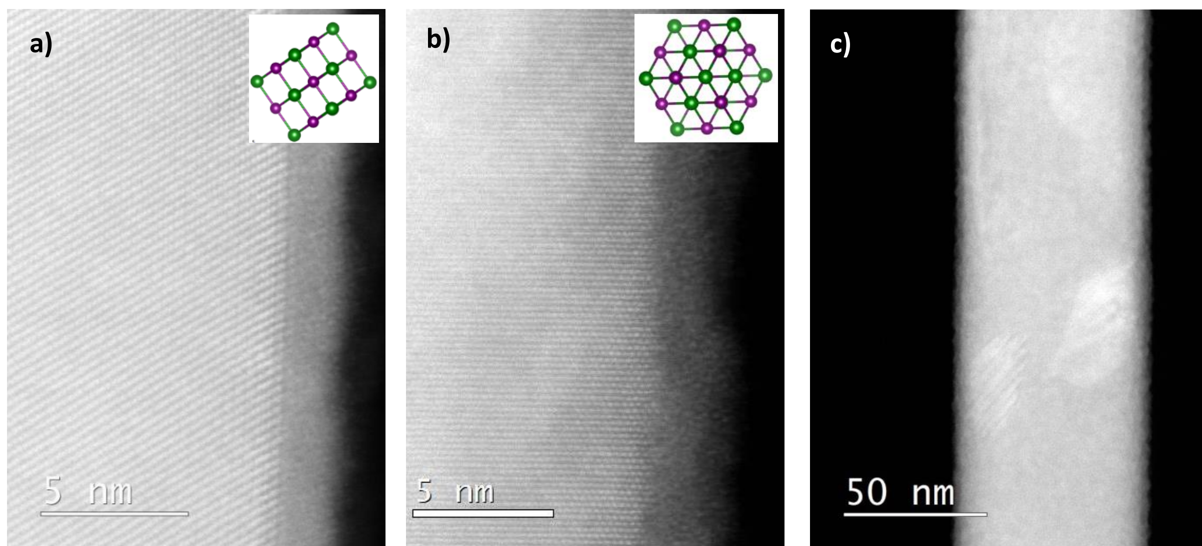

Fig. 4.31: SnTe nanowires grown for 2 hours under low fluxes and low temperature. The growth direction is $\{112\}$ *and the zone axis are (a)* $\{0\text{-}2\ 2\}$ *and (b)* $\{1\text{-}11\}$ *the former can be obtained from the latter by rotating the viewing angle of the TEM* $35.26°$ *with respect to the* $\{011\}$ *axes. (c) Defects present in the same nanowire.*

In EDX it was observed that within an uncertainty of order 1% the composition of the nanowires were $\mathrm{Sn{:}Te} = 50{:}50$. No traces of gold, indium or others metals than Sn were found inside the wires in contrast to the smaller nanowires (see Fig. 4.26d)) . However, after more elaborate investigation of the deposited polycrystalline SnTe film (more specifically the film in the area marker red in Fig. 4.30c)), gold was found in SEM/EDX investigation. The gold could have been deposited unnoticed because cleaving of gold-free substrates and substrates with gold were cleaved with the same tools. In EDX investigation of the small (1 hour grown) nanowires was found that they have a thick SnO_x shell. Moreover the Sn concentration seems to be higher in the shell of the nanowire than in the core, while the Te concentration seems to be uniform. Fig. 4.32 shows an EDX mapping of a small nanowire. From 4.32 we suspect that the Sn actually diffuses out of the core and for an oxide at the shell.

The oxide formation found in EDX certainly destroys the TCI behaviour of the nanowires. First of all the surface is not mirror symmetric anymore which is needed for the TCI surface states. Besides that, if Sn diffuses out of the core, the stochiometry of the bulk is rich of Te and poor of Sn. This means that there are a high amount of defects that disrupt the lattice symmetry and therefore the TCI behavior.

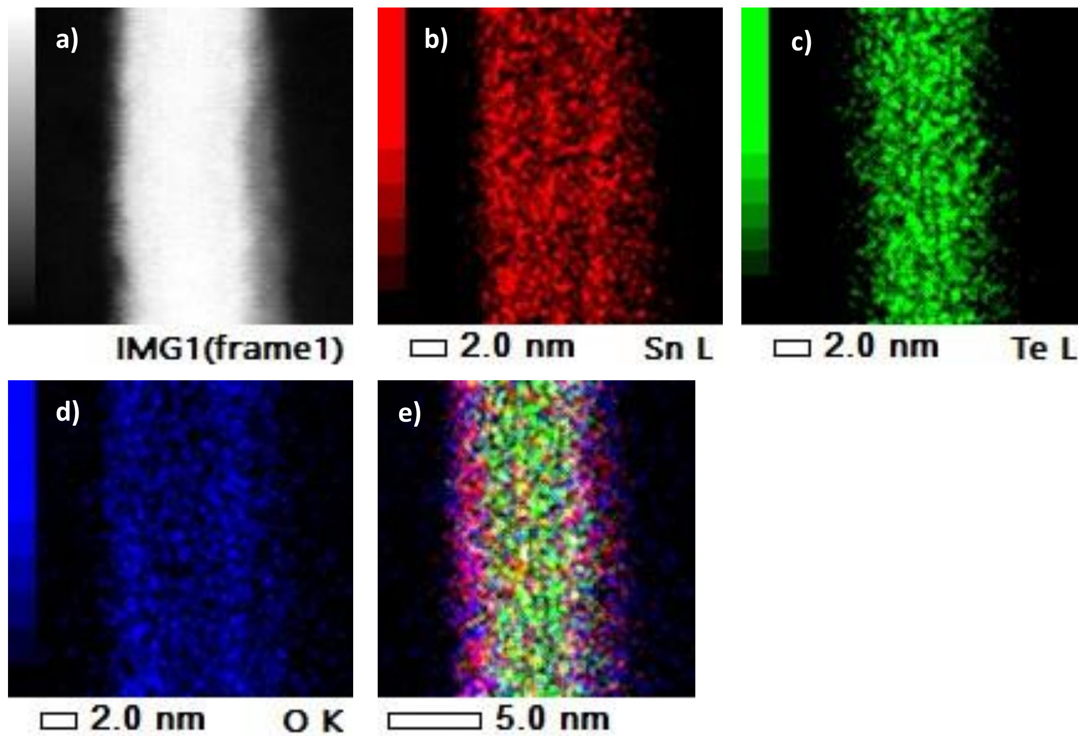

Fig. 4.32: EDX images of a small SnTe nanowire grown for 1 hour from which can be seen that the core is Te rich, while the shell is SnO_x rich.

4.3.5 Thermal annealing and positive T-gradients

Besides growth under constant temperature also different temperature profiles were tried. First off all annealing for 30 min at $T_B = 430$ °C after growth for 30 min at $T_B = 210$ °C was performed. The results was that all SnTe was reevaporated again, some traces of Sn and/or Au remained. Besides that, annealing at $T_B = 513$ °C for 30 min before growth was done with no change in growth results. Additionally high temperature Sn deposition before low temperature (~ 210°C) growth was performed as well as annealing under Te after growth, which both did not improve growth results.
Another approach was to apply a positive temperature gradient during growth. Growth was started at 190°C, while the temperature rises for 30 min ending at temperatures of $T_B = 300 - 370$°C. The idea here is that nucleation can occurs at low temperature, while growth occurs at higher temperatures so that parasitic growth may be suppressed. For low end temperatures the growth results were similar as constant low temperature growth (Fig. 4.33c-d)), while for an end temperature of $T_B = 330$ °C (Fig. 4.33c)) no nanowires were found. For high end temperatures only droplets remain on the substrate (Fig. 4.33a-b)).

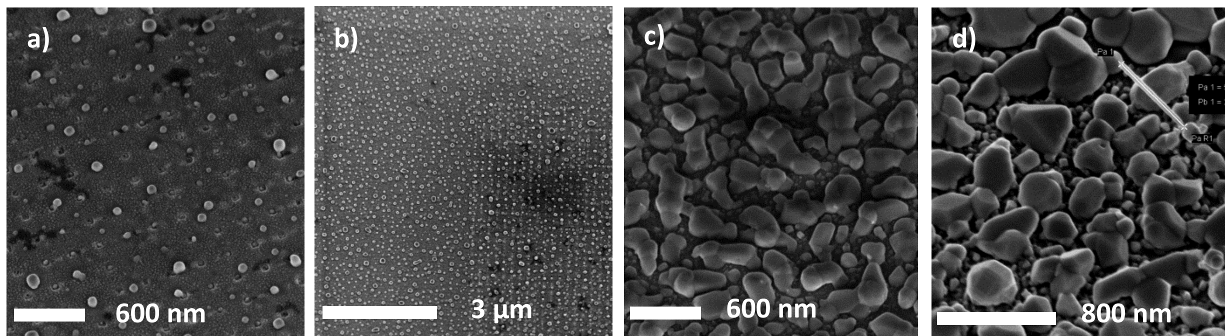

Fig. 4.33: Growth results at Ge/SiN$_x$/Au patterns for growth for 30 min under a positive temperature gradient. For end temperatures of $T_B = 370$ °C, $T_B = 360$ °C, $T_B = 330$ °C and $T_B = 300$ °C. Where for the first 3 the temperature kept rising for 30 min, but for the latter the temperature was already stable after 10 min. Fluxes were the same as growth 19: $p_{Sn} = 7.7 \cdot 10^{-8}$ Torr and $p_{Te} = 5 \cdot 10^{-7}$ Torr. *Magnifications are (a) 72 KX, (b) 20 KX, (c) 79 KX, (d) 100 KX.*

4.3.6 Substrate processing

From all the different substrates that were loaded in the MBE none of them showed particularly better growth than others. Most of the nanowires that were grown in the first attemps (around growth 19) also did not show a preference for growing on bare substrate or on top SiN_x. It can be concluded that, under the growth conditions that were explored, the SnTe growth is not effected by the SiN_x mask. There is no selectivity to grown within the lithographically etched holes. The early nanowire grown at low temperatures and intermediate fluxes (growth 19) did depend though on the presence of gold at the substrate. The growth did only occur at EBL dose markers and lithographical patterns with lift-off problem.

To have growth on the whole substrate attempts were made to recreate these gold-rich regions on the whole substrate. It was found that simply covering the whole substrate with Au did not recreate this, as the number of nanowires found was much lower. Also attempts were made to recreate the rough surface of the EBL dose markers, which is RIE etched and can contain some SiN_x residues. This was done by depositing SiN_x on the substrate, RIE (under-)etching the samples and depositing a layer of Au. Also these attempts did not reproduce the growth behavior found on the defective EBL-Au-pattern.

One approach that did somewhat recreate the growth behavior of the defective EBL-Au-pattern on bigger scales was achieved as follows. On a $\mathrm{Si}\ (100)$ substrate 50 nm $SiN_x$was deposited. By doing a BHF gradient etch (see section 3.3) and RIE etching a rough surface was created with different SiN_x thickness on different parts of the substrate. After depositing $8\ \mathrm{nm}$ of gold, the whole samples of submerged in BHF for 5 s. The result was a rough surface with big flakes of gold on certain areas of the samples with thicker SiN_x. The rough morphology of these areas promoted the growth of all kinds of nanowires in different sizes and shape, as shown in Fig. 4.34. The same growth parameters as growth 19 were used.

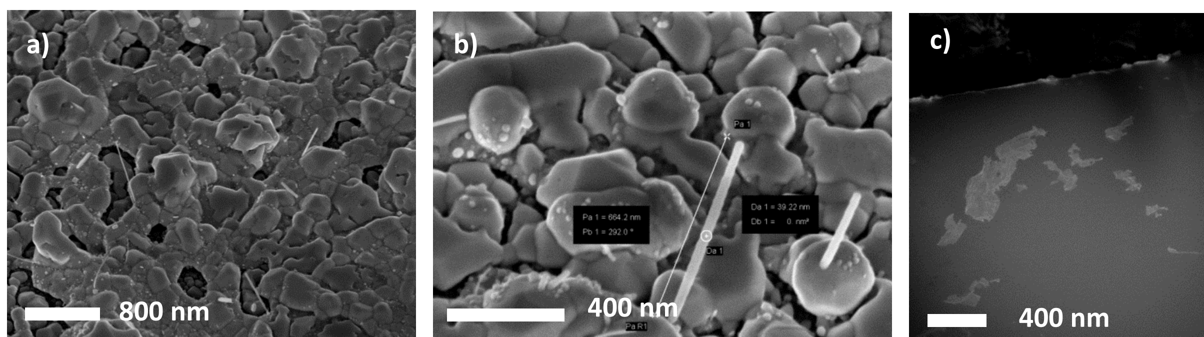

Fig. 4.34: Nanowire growth on a rough surface with gold. Magnifications are (a) 52 KX, (b) 180 KX and (c) 0.1 KX.

References Chapter 4

1. T. Hsieh, H. Lin, J. Liu, W. Duan, A. Bansil, L. Fu, 'Topological crystalline insulators in the SnTe material class', *Nat. Com. 3,* (2012).
2. S. Safaei, P. Kacman, R. Buczko, 'The topological-crystalline insulator (Pb,Sn)Te – surface states and their spin-polarization', *Phys. Rev. B 88,* (2013).
3. J. Liu, L. Fu, 'Electrically tunable quantum spin Hall state in topological crystalline insulator thin films', *Phys. Rev. B* 91, (2015).
4. S. Safaei, M. Galicka, P. Kacman, R. Buczko, 'Quantum spin Hall effect in IV-VI topological crystalline insulators', *New Journal of Physics*, (2015).
5. J. Liu, W. Duan, L. Fu, 'Two types of surface states in topological crystalline insulators', *Phys. Rev. B* 88, (2013).
6. H. Ozawa, A. Yamakage, M. Sato, Y. Tanaka, 'Topological phase transition in a topological crystalline insulator induced by finite-size effects', *Phys. Rev. B* 90, (2014).
7. J. Linder, T. Yokoyama, A. Sudbø, *Phys. Rev.* 80, (2009).
8. J. Liu, L. Fu, 'Electrically tunable quantum spin Hall state in topological crystalline insulator thin films', *Phys. Rev. B* 91, (2015).
9. J. Liu, T. Hsieh, 'Spin-filtered edge states with an electrically tunable gap in a two-dimensional topological crystalline insulator' *Nat. Mat.* 13, 178-183, (2014).
10. https://topocondmat.org/w2_majorana/Peierls.html
11. https://topocondmat.org/w1_topointro/0d.html
12. T. Hsieh, H. Lin, J. Liu, W. Duan, A. Bansil, L. Fu, 'Topological crystalline insulators in the SnTe material class', *Nat. Com. 3,* (2012).
13. P. Sessi, 'Robust spin-polarized midgap states at step edges of topological crystalline insulators', *Science* 354, 6317, pp. 1269-1273, (2016), Supplementary Materials.
14. J. Li, H. Chen, B. A. Bernevig, A. H. MacDonald, 'Topological superconductivity induced by ferromagnetic metal chains', *Phys. Rev. B* 90, 235433, (2014).
15. S. Mi, M. Wimmer, C. Beenakker, 'Proposal for the detection and braiding of Majorana fermions in a quantum spin Hall insulator', *Phys. Rev. B* 87, 241405, (2013).
16. Dedi, Ping-Chung Lee, 'Stress-induced growth of single-crystalline lead telluride nanowires and their thermoelectric transport properties', *Apl. Phys. Let.* 103, 023115 (2013).
17. O. Madelung, U. Rössler, M. Schulz, 'Non-Tetrahedrally Bonded Elements and Binary Compounds I', Subvolume C, Vol 41, 'Semiconductors', Landolt-Börnstein –Group III Condensed Matter, *Springer*, (2001).

5. Conclusion and outlook

In this research the potential of SnTe in the application of the topological qubit was investigated. This was approached from a modelling and a materials science perspective.

The main results from the modelling parts are that tight binding calculations done in literature could be reproduced well in most cases. This includes the modelling of energy dispersions of SnTe bulk surfaces and thin films. Due to confidence gained by these calculations the model was used to calculate nanowire dispersions. The nanowire energy dispersions are not comprehensive and leave room for follow-up studies. However indications of Dirac physics were observed.
Moreover Majorana fermions were found when superconductivity was applied to SnTe thin films, where at each end of a superconducting π-junction 2 and 4 Majorana fermions were found for the $[111]$ and $[001]$ thin films respectively. Here the $[001]$ thin film is the most special, not only because it has the lowest energy of formation in growth, but also since the $[001]$ surface is not a conventional quantum spin Hall insulator.

In the growth part, SnTe nanowires grown in MBE were discussed, which has not been reported in literature yet. We managed to grow SnTe nanowires at low temperatures ($T_B \approx 210$°C) at low material fluxes; $p_{Sn} = 1.0 \cdot 10^{-8} - 7.7 \cdot 10^{-8}$ Torr and $p_{Te} = 2.90 \cdot 10^{-7} - 5 \cdot 10^{-7}$ Torr. The nanowires are monocrystalline and, when grown under low fluxes, no traces of Au are detected in EDX. Different sizes of SnTe nanowires can be grown from about 300 nm up to 5 μm long and from 15 nm up till 100 nm in diameter. Nanowires in $\{110\}$ and $\{112\}$ growth directions were found, which is in contrast to literature were mostly $\{001\}$ wires are found. The surface facets seem to be mostly $\{001\}$ and $\{110\}$, if it is assumed that the nanowires lie on one of their flat facets in TEM. Finally layers of O_x and SnO_x are present on the surfaces of the wires, which could perturb the TCI surface states on its surface.

For further research multiple experiments can be done. First of all the charge carrier density of the nanowires should be investigated, using field effect measurements. The reason is that the SnTe should be grown as intrinsic as possible to be able to utilize the special properties of the TCI. A field effect setup is shown in Fig. 5.1.
Besides that the surface of the nanowire should be protected against oxidation. This could be done by capping the nanowire with an amorphous layer of AlOx.
Moreover the rocksalt II-VI semiconductor CaTe could be used to make SnTe-CaTe heterostructures. In the growth of SnTe thin films it could be used as a lattice matched large bandgap barrier material to keep charge carrier confined to the SnTe layer. However interface charges between the II-VI and the IV-VI materials should then be investigated.
Next to confirm the TCI state of the SnTe nanowires an Aharonov-Bohm experiment[2] could be performed. Namely, if the TCI follows the behavior of a TI, applying a magnetic field through the cross-section of the nanowire should result in a conductance which oscillates while varying the magnetic field. For a TI the period of this oscillation should then be equal to the magnetic flux quantum h/e.

Finally to confirm the existence of Majorana fermions in SnTe nanowires further research of the normal state dispersions have to be done. This could be done in first instance by formulating a effective model so that smaller system can be simulated.

References Chapter 5

1. J.H. Bardarson, P.W. Brouwer, J.E. Moore, ‘Aharonov-Bohm oscillations in disordered topological insulators nanowires’, *Phys. Rev. Lett.* 105, 156803, (2010).

6. Appendix

6.1 Surface density of states method

We calculate the surface density of states through the Green's function of a semi-infinite lead, using Kwant[1-3]. For surface states of 3D samples we use an infinite slab geometry with two translation invariant directions parallel to the surface and semi-infinite boundary condition in the perpendicular direction. Similarly, for edge states of thin films we use one translation invariant direction along the edge, finite boundary condition for the thickness of the film and semi-infinite boundary condition in the third direction. This effectively reduces the problem to solving a semi-infinite one dimensional chain for every surface or edge momentum $k||$. The Hamiltonian consists of on-site terms $H_0\,(k||)$ and hopping terms $V(k||)$.

To get the momentum-dependent surface density of states, we evaluate the Green's function of the end site of the chain $g_0(k||, E)$ as function of the surface momentum and energy. The projections of the bulk bands onto the surface Brillouin zone appear as continuous weights, while the surface bands are sharp peaks. The momentum-dependent surface density of states is experimentally accessible using ARPES measurements.

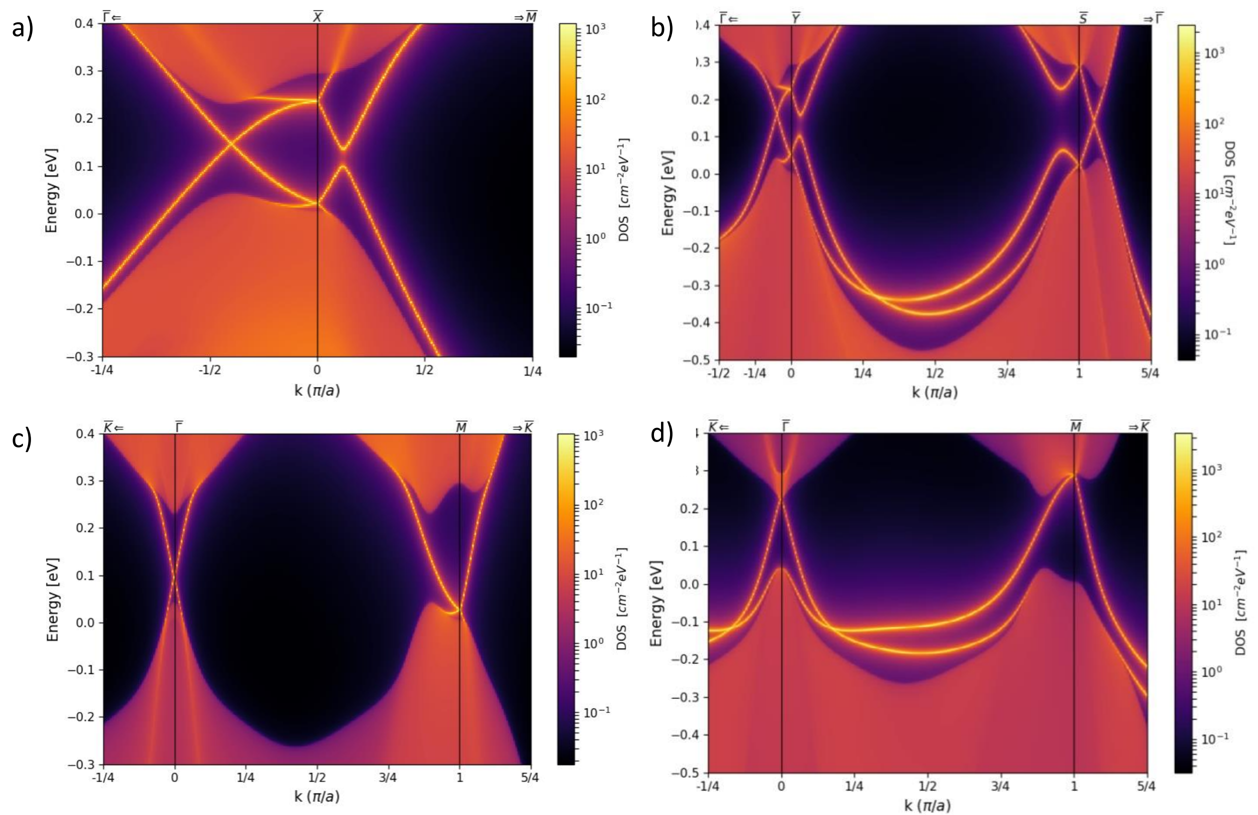

Fig. 6.1: Density of states calculations of the the (a) $[001]$*, (b)* $[110]$*, (c) Sn-terminated* $[111]$ *and (d) Te-terminated* $[111]$ *surface facets.*

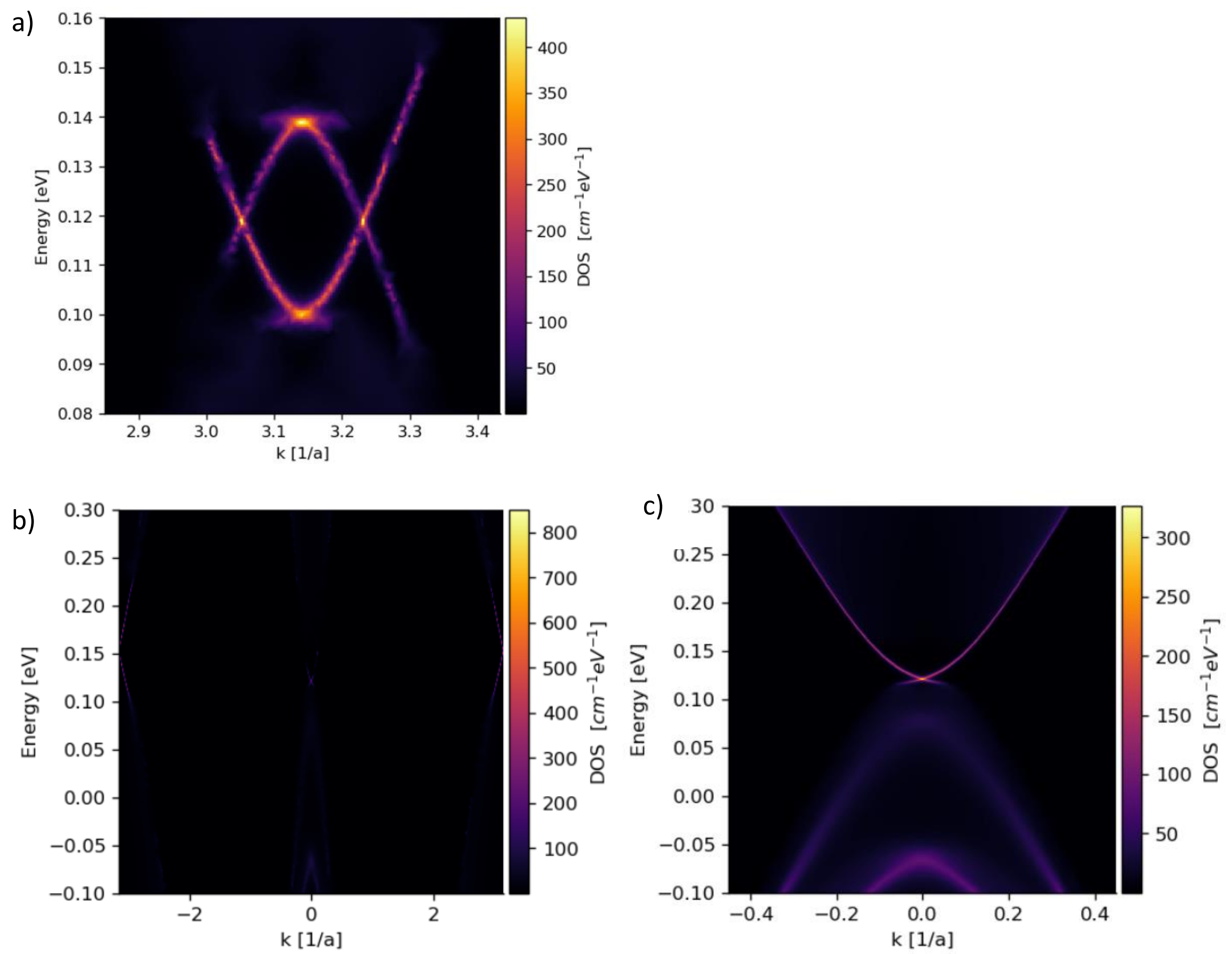

Fig. 6.2: Density of state calculations of (a) $[001]$ *and (b-c)* $[110]$ *thin films.*

6.2 Derivation of Angular momentum matrices

6.2.1 Derivation Angular momentum matrices p-orbitals

The L matrix for the p-orbitals can be derived directly using the orbitals themselves. The diagonal L-matrix is written in the basis of m (or L_z) eigenstates, but it is different from the p_x, p_y, p_z basis. These eigenfunctions look like

$$p_x(r) = Axe^{-|\vec{r}|/\rho}, \tag{6.1}$$

where A and ρ are constants, r is the distance to the origin and x is the x-component of $\vec{r}$. The wavefunction $p_y(r)$ and $p_z(r)$ are similar, only the x is replaced by y and z.

The relevant wave functions in the basis in which the L_z-matrix is diagonal are given by[4]:

$$\begin{aligned} \Psi_{21+1} &= -Are^{-\frac{|\vec{r}|}{\rho}} \sin\theta\, e^{+i\varphi}, \\ \Psi_{210} &= Are^{-|\vec{r}|/\rho} \cos\theta, \\ \Psi_{21-1} &= +Are^{-|\vec{r}|/\rho} \sin\theta\, e^{-i\varphi}. \end{aligned} \tag{6.2}$$

The p_z state is the same as the $m = 0$ state, but the p_x and p_y states are linear combinations of the $m = +1$ and $m = -1$ states so that

$$p_z = \Psi_0 \tag{6.3}$$

$$p_x = \frac{1}{\sqrt{2}}(-\Psi_{211} + \Psi_{21-1}), \tag{6.4}$$

and

$$p_y = \frac{i}{\sqrt{2}}(\Psi_{211} + \Psi_{21-1}). \tag{6.5}$$

In the old basis the p-orbital angular momentum matrix in the z-direction is given by

$$L_{z,p}' = \hbar \begin{pmatrix} 1 & 0 & 0 \\ 0 & 0 & 0 \\ 0 & 0 & -1 \end{pmatrix}. \tag{6.6}$$

The change of basis to the new basis of p_x, p_y and p_z orbitals is achieved by the transformation

$$L_{z,p} = T^{-1} L_{z,p}' T, \tag{6.7}$$

where, by equations 6.3-6.5,

$$T = \begin{pmatrix} -\frac{1}{\sqrt{2}} & \frac{i}{\sqrt{2}} & 0 \\ 0 & 0 & 1 \\ \frac{1}{\sqrt{2}} & \frac{i}{\sqrt{2}} & 0 \end{pmatrix}. \tag{6.8}$$

Therefore in the new basis

$$L_{z,p} = \hbar \begin{pmatrix} 0 & -i & 0 \\ i & 0 & 0 \\ 0 & 0 & 0 \end{pmatrix}. \tag{6.9}$$

Following the same steps (with different matrices for $L_{x,p}'$ and $L_{y,p}'$ obtained by using the ladder operators[5]) the x and y components are acquired:

$$L_{x,p} = \hbar \begin{pmatrix} 0 & 0 & 0 \\ 0 & 0 & -i \\ 0 & i & 0 \end{pmatrix} \text{ and } L_{y,p} = \hbar \begin{pmatrix} 0 & 0 & i \\ 0 & 0 & 0 \\ -i & 0 & 0 \end{pmatrix}. \tag{6.10}$$

6.2.2 Derivation Angular momentum matrices d-orbitals

Also the L matrix for the d-orbitals can be derived directly using the orbitals themselves. The diagonal L-matrix is written in the basis of m (or L_z) eigenstates, but it is different from the basis of d-orbitals. These eigenfunctions look like

$$\begin{aligned} d_{x^2-y^2} &= A(x^2-y^2)e^{-|\vec{r}|/\rho}, \\ d_{3z^2-r^2} &= A(z^2-r^2)e^{-|\vec{r}|/\rho}, \\ d_{xy} &= Axye^{-|\vec{r}|/\rho}, \\ d_{yz} &= Ayze^{-|\vec{r}|/\rho}, \\ d_{zx} &= Azxe^{-|\vec{r}|/\rho}, \end{aligned} \tag{6.11}$$

where A and ρ are constants, r is the distance to the origin and x is the x-component of $\vec{r}$.

The relevant wave functions in the basis in which the L-matrix is diagonal are given by:

$$\begin{aligned} \Psi_{322} &= Ar^2e^{-|\vec{r}|/\rho}\sin^2\theta\, e^{+i2\varphi} \\ \Psi_{321} &= Ar^2e^{-|\vec{r}|/\rho}\sin\theta\cos\theta\, e^{+i\varphi} \\ \Psi_{320} &= Ar^2e^{-|\vec{r}|/\rho}(3\cos^2\theta-1) \\ \Psi_{32-1} &= Ar^2e^{-|\vec{r}|/\rho}\sin\theta\cos\theta\, e^{-i\varphi} \\ \Psi_{32-2} &= Ar^2e^{-|\vec{r}|/\rho}\sin^2\theta\, e^{-i2\varphi} \end{aligned} \tag{6.12}$$

Therefore the d states can be expressed in the new basis using the following relations

$$\begin{aligned} d_{x^2-y^2} &= \frac{1}{\sqrt{2}}(\Psi_{322}+\Psi_{32-2}) \\ d_{3z^2-r^2} &= \Psi_{320} \\ d_{xy} &= \frac{i}{\sqrt{2}}(-\Psi_{322}+\Psi_{32-2}) \\ d_{yz} &= \frac{-i}{\sqrt{2}}(\Psi_{32-1}+\Psi_{321}) \\ d_{zx} &= \frac{1}{\sqrt{2}}(\Psi_{321}-\Psi_{32-1}) \end{aligned} \tag{6.13}$$

In the old basis the angular momentum matrix is given by

$$L_{z,d}{}' = \hbar\begin{pmatrix} 2 & 0 & 0 & 0 & 0 \\ 0 & 1 & 0 & 0 & 0 \\ 0 & 0 & 0 & 0 & 0 \\ 0 & 0 & 0 & -1 & 0 \\ 0 & 0 & 0 & 0 & -2 \end{pmatrix}. \tag{6.14}$$

The change of basis is achieved by the transformation

$$L_{z,d} = T^{-1}L_{z,d}{}'T, \tag{6.15}$$

where, by equation 6.13,

$$T = \begin{pmatrix} \frac{1}{\sqrt{2}} & 0 & \frac{-i}{\sqrt{2}} & 0 & 0 \\ 0 & 0 & 0 & \frac{-i}{\sqrt{2}} & \frac{1}{\sqrt{2}} \\ 0 & 1 & 0 & 0 & 0 \\ 0 & 0 & 0 & \frac{-i}{\sqrt{2}} & \frac{-1}{\sqrt{2}} \\ \frac{1}{\sqrt{2}} & 0 & \frac{i}{\sqrt{2}} & 0 & 0 \end{pmatrix} \tag{6.16}$$

Therefore the angular momentum matrix L_z of the d-orbtibals in the new Lent's basis $d_{x^2-y^2}$, $d_{3z^2-r^2}$, d_{xy}, d_{yz}, d_{zx} is given by

$$L_{d,z} = \begin{pmatrix} 0 & 0 & -2i & 0 & 0 \\ 0 & 0 & 0 & 0 & 0 \\ 2i & 0 & 0 & 0 & 0 \\ 0 & 0 & 0 & 0 & i \\ 0 & 0 & 0 & -i & 0 \end{pmatrix}. \tag{6.17}$$

Now using

$$\langle lm' | L_{\pm} | lm \rangle = \sqrt{l(l+1) - m(m \pm 1)}\hbar\delta_{m\prime(m\pm1)} \tag{6.18}$$

the ladder operators are derived, such that

$$L_{+} = \begin{pmatrix} 0 & 2 & 0 & 0 & 0 \\ 0 & 0 & \sqrt{6} & 0 & 0 \\ 0 & 0 & 0 & \sqrt{6} & 0 \\ 0 & 0 & 0 & 0 & 2 \\ 0 & 0 & 0 & 0 & 0 \end{pmatrix},$$

and

$$L_{-} = \begin{pmatrix} 0 & 0 & 0 & 0 & 0 \\ 2 & 0 & 0 & 0 & 0 \\ 0 & \sqrt{6} & 0 & 0 & 0 \\ 0 & 0 & \sqrt{6} & 0 & 0 \\ 0 & 0 & 0 & 2 & 0 \end{pmatrix}.$$

The L_x and L_y matrices for the d-orbitals in the old basis are obtained as

$$L'_{d,x} = \frac{1}{2}(L_{+} + L_{-}) = \begin{pmatrix} 0 & 1 & 0 & 0 & 0 \\ 1 & 0 & \sqrt{3/2} & 0 & 0 \\ 0 & \sqrt{3/2} & 0 & \sqrt{3/2} & 0 \\ 0 & 0 & \sqrt{3/2} & 0 & 1 \\ 0 & 0 & 0 & 1 & 0 \end{pmatrix} \tag{6.19}$$

and

$$L'_{d,y} = \frac{1}{2i}(L_{+} - L_{-}) = \begin{pmatrix} 0 & -i & 0 & 0 & 0 \\ i & 0 & -i\sqrt{3/2} & 0 & 0 \\ 0 & i\sqrt{3/2} & 0 & -i\sqrt{3/2} & 0 \\ 0 & 0 & i\sqrt{3/2} & 0 & -i \\ 0 & 0 & 0 & i & 0 \end{pmatrix}. \tag{6.20}$$

Therefore using equation 6.15 we also get:

$$L_{d,x} = \begin{pmatrix} 0 & 0 & 0 & -i & 0 \\ 0 & 0 & 0 & -i\sqrt{3} & 0 \\ 0 & 0 & 0 & 0 & i \\ i & i\sqrt{3} & 0 & 0 & 0 \\ 0 & 0 & -i & 0 & 0 \end{pmatrix}, \tag{6.21}$$

$$\text{and} \qquad L_{d,y} = \begin{pmatrix} 0 & 0 & 0 & 0 & -i \\ 0 & 0 & 0 & 0 & i\sqrt{3} \\ 0 & 0 & 0 & -i & 0 \\ 0 & 0 & i & 0 & 0 \\ i & -i\sqrt{3} & 0 & 0 & 0 \end{pmatrix}.$$

6.3 Python code

Multiple Python codes were written for this report. Here an example is given for the calculation of the energy dispersion of a 41×41 or 129×129 Å nanowire with $\{001\}$ side facets. Additionally the code for a calculation of the eigenvalues for a finite 3D $[001]$ thin film is given.

Code 1: $[001]$ Nanowire energy dispersion (normal state) code

```
1.  %%px --local
2.  
3.  %matplotlib notebook
4.  
5.  #import packages locally (also do this on cluster)
6.  import gc
7.  import numpy as np
8.  import kwant
9.  import pickle
10. from __future__ import division
11. import matplotlib.pyplot as plt
12. from matplotlib.colors import LinearSegmentedColormap
13. from scipy.optimize import minimize_scalar
14. import scipy.linalg as la
15. import scipy
16. import sys
17. import scipy.sparse.linalg as sla
18. import itertools as it
19. import functools as ft
20. from pandas import *
21. from combine import combine
22. from sntefunc import sntepar
23. import operator
24. import gc
25. import kwant.linalg.mumps as mumps
26. from scipy.sparse import identity
27. from sntefunc import sntepar
28. from matplotlib.colors import LogNorm
29. 
30. %%capture
31. gc.collect()
32. # kwant stable unit cell choice [100] surface
33. lat = kwant.lattice.general(np.eye(3))
34. translations = kwant.lattice.TranslationalSymmetry([1, 1, 0], [1, -
    1, 0], [1, 0, 1])
35. syst = kwant.Builder(symmetry=translations)
36. 
37. #Specifiy/import onsite and hopping terms of the Hamiltonian
38. SnX=1
39. mu=-0.12
40. def onsitea(site):
41.     return sntepar(SnX,mu,1)[6]
42. def onsitec(site):
43.     return sntepar(SnX,mu,1)[7]
44. def Hoacxp(site1, site2):
45.     return sntepar(SnX,mu,1)[0]
46. def Hoacxm(site1, site2):
47.     return sntepar(SnX,mu,1)[1]
48. def Hoacyp(site1, site2):
49.     return sntepar(SnX,mu,1)[2]
50. def Hoacym(site1, site2):
51.     return sntepar(SnX,mu,1)[3]
52. def Hoaczp(site1, site2):
53.     return sntepar(SnX,mu,1)[4]
```

```
54. def Hoaczm(site1, site2):
55.     return sntepar(SnX,mu,1)[5]
56. # Populate the builder using the cubic lattice sites
57. # Use different on-sites for the two sublattices
58. syst[lat(0, 0, 0)] = onsitea
59. syst[lat(0, 0, 1)] = onsitec
60. # Use different hoppings depending on the type
61. syst[(lat(0,0,0), lat(1, 0, 0))] = Hoacxp
62. syst[(lat(0,0,0), lat(-1, 0, 0))] = Hoacxm
63. syst[(lat(0,0,0), lat(0, 1, 0))] = Hoacyp
64. syst[(lat(0,0,0), lat(0, -1, 0))] = Hoacym
65. syst[(lat(0,0,0), lat(0, 0, 1))] = Hoaczp
66. syst[(lat(0,0,0), lat(0, 0, -1))] = Hoaczm
67.
68. #
69. film = kwant.Builder(kwant.lattice.TranslationalSymmetry([0,0,2]))
70. def shape(site):
71.     return (-20.5 < (np.dot(site.tag, [0,1,0])) < 20.5 and -
    20.5 < (np.dot(site.tag, [1,0,0])) < 20.5)
72. film.fill(syst, shape, start=np.zeros(3));
73. wrapped = kwant.wraparound.wraparound(film)
74. sysf = wrapped.finalized()
75. #
76.
77. def ndlinspace(start, end, N):
78.     start, end = np.array(start), np.array(end)
79.     return np.array([start + (end - start) * x
80.                      for x in np.linspace(0, 1, N)])
81.
82. kd= 40
83. Nk = 250
84. Egap = 0.0
85.
86. #Set k_1,k_2,k_3:
87. k_1, k_2 = [np.pi-1,0, 0], [np.pi+1,0,0]
88. ks = ndlinspace(k_1, k_2, Nk)
89.
90. class LuInv(sla.LinearOperator):
91.     def __init__(self, A):
92.         inst = mumps.MUMPSContext()
93.         inst.analyze(A, ordering='pord')
94.         inst.factor(A)
95.         self.solve = inst.solve
96.         sla.LinearOperator.__init__(self, A.dtype, A.shape)
97.     def _matvec(self, x):
98.         return self.solve(x.astype(self.dtype))
99.
100.def y2(ks):
101.    params={'k_x':ks[0]}
102.    H = scipy.sparse.coo_matrix(sysf.hamiltonian_submatrix(params=params, sparse=Tr
    ue))
103.    opinv = LuInv(H - Egap * identity(H.shape[0]))
104.    E = sla.eigsh(H,k=kd, sigma=Egap, return_eigenvectors=False,OPinv=opinv)
105.#     wfi = []
106.#     for i in range(kd):
107.#         T = W[:,i];
108.#         W2= []
109.#         for j in range(len(T)):
110.#             if int(j/18) % 2==1:
111.#                 W2.append(T[j])
112.#         abswfi = [abs(x)**2 for x in W2]
113.#         wft = sum(abswfi)
114.#         wfi.append(wft)
115.    EW=E #[E,wfi]
116.    gc.collect()
117.    return EW
```

```
118.
119.x=ks
120.y2 = lview.map_async(lambda x : y2(x),x)
121.y2.wait_interactive()
122.y2 = y2.get()
123.
124.#Set k_1,k_2,k_3:
125.y3 = []
126.for x in y2:
127.    y3.append(x)
128.# y4 = []
129.# for x in y2:
130.#     y4.append(x[1])
131.x=np.repeat(np.linspace(np.pi-0.3,np.pi+0.3,len(ks)),kd)
132.y5 = np.ndarray.flatten(np.array(y3))
133.#y6 = np.ndarray.flatten(np.array(y4))
134.fig = plt.figure()
135.fig.set_size_inches(8,5)
136.plt.scatter(x,y5,s=0.2)
137.ax = plt.gca()
138.plt.ylabel('Energy [eV]', fontsize=12)
139.plt.xlabel('k ($1/a$)', fontsize=12)
140.# plt.xticks([0,Nk/2,Nk,3*Nk/2,2*Nk],['-1/4','-1/2','0','1/2','$1/4$'])
141.ax.set_xlim([np.pi-0.3,np.pi+0.3])
142.ax.set_ylim([-0.15,0.15])
143.# plt.axvline(x=Nk,c='k',linewidth=0.8)
144.# ax.annotate('$\overline{\Gamma} \Leftarrow$',xy=(0,0.40))
145.# ax.annotate('$\overline{X}$',xy=(Nk-4,0.40))
146.# ax.annotate('$\Rightarrow \overline{M}$',xy=(2*Nk-22,0.40))
147.# ax.annotate('$\Psi$',xy=(3.1*len(ks)/3,0.05))
148.# cbar=plt.colorbar()
149.# cbar.set_label('                 $|\Psi^2|_{cation/Sn}$', rotation=0)
```

Code 2: Finite [001] Thin film (superconducting) eigenvalue calculation

```
1.  %%px --local
2.
3.  def spin_matrices(s, include_0=False):
4.      """Construct spin-s matrices for any half-integer spin.
5.      If include_0 is True, S[0] is the identity, indices 1, 2, 3
6.      correspond to x, y, z. Otherwise indices 0, 1, 2 are x, y, z.
7.      """
8.      d = np.round(2*s + 1)
9.      assert np.isclose(d, int(d))
10.     d = int(d)
11.     Sz = 1/2 * np.diag(np.arange(d - 1, -d, -2))
12.     # first diagonal for general s from en.wikipedia.org/wiki/Spin_(physics)
13.     diag = [1/2*np.sqrt((s + 1) * 2*i - i * (i + 1)) for i in np.arange(1, d)]
14.     Sx = np.diag(diag, k=1) + np.diag(diag, k=-1)
15.     Sy = -1j*np.diag(diag, k=1) + 1j*np.diag(diag, k=-1)
16.     if include_0:
17.         return np.array([np.eye(d), Sx, Sy, Sz])
18.     else:
19.         return np.array([Sx, Sy, Sz])
20.
21. def L_matrices(d=3):
22.     """Construct rotation generator matrices in d=2 or 3 dimensions.
23.     To generate finite rotations, use 'spin_rotation(n, 1j * L)'.
24.     """
25.     if d == 2:
26.         return np.array([[[0, -1],
27.                           [1, 0]]], dtype=int)
28.     elif d == 3:
```

```
29.         return np.array([[[0, 0, 0],
30.                           [0, 0, -1],
31.                           [0, 1, 0]],
32.                          [[0, 0, 1],
33.                           [0, 0, 0],
34.                           [-1, 0, 0]],
35.                          [[0, -1, 0],
36.                           [1, 0, 0],
37.                           [0, 0, 0]]], dtype=int)
38.     else:
39.         raise ValueError('Only 2 and 3 dimensions are supported.')
40.
41. S = spin_matrices(1/2)
42. L = L_matrices(3)
43. Ld = np.array([np.zeros((5, 5)), np.zeros((5, 5)), la.block_diag(2j*L[1], -
    2*S[1])])
44.
45. # %%px --local
46. mu_B = 5.788381755*10**-5 ##eV/T
47.
48. Mp = mu_B * np.array([np.kron(np.eye(2), L) +  2 * np.kron(s, np.eye(3))
49.                 for L, s in zip(1j*L, spin_matrices(1/2))])
50.
51. Mz = mu_B * 2 * 0.5 * (Mp[0]+Mp[1]+Mp[2]) #np.array([[1,1j,0,0,0,0],[-
    1j,1,0,0,0,0],[0,0,1,0,0,0],[0,0,0,-1,1j,0],[0,0,0,-1j,-1,0],[0,0,0,0,0,-
    1]]) #la.block_diag(Ms[2], Mp[2], Md[2])
52.
53. # Define bulk model
54.
55. # Misc definitions
56. eijk = np.zeros((3, 3, 3))
57. eijk[0, 1, 2] = eijk[1, 2, 0] = eijk[2, 0, 1] = 1
58. eijk[0, 2, 1] = eijk[2, 1, 0] = eijk[1, 0, 2] = -1
59. sigma = np.array([[[1, 0], [0, 1]], [[0, 1], [ 1, 0]], [[0, -
    1j], [1j, 0]], [[1, 0], [0, -1]]])
60. #print(eijk)
61.
62. # Define cubic lattice that contains both sublattices
63. lat = kwant.lattice.general(np.eye(3))
64. # Define Builder with FCC translational symmetries.
65. # Note that the primitive vectors are chosen so the first two are in the xy plane
66. # so they can be used for the slab
67. translations = kwant.lattice.TranslationalSymmetry([1, -1, 0], [1, 0, -
    1], [0, 1, 1])
68. syst = kwant.Builder(symmetry=translations)
69.
70. # Array for hopping types
71. a=1 #0.98
72. b=1 #0.98
73. c=1 #1.035
74. t = 2*np.array([[-a*0.25, b*0.45], [b*0.45, a*0.25]])
75. mu=-0.008119
76. m = np.array([-c*1.65+mu, c*1.65+mu])
77. # Array for onsite SOC
78. lam = np.array([-0.3, -0.3]) #new
79.
80. def onsite(site,B_z,ef):
81.     # which sublattice
82.     a = np.sum(site.tag) % 2
83.     os = m[a] * np.eye(6)
84.     #os = os + 1j * lam[a] * np.sum([np.kron(eijk[:, :, i], sigma[i + 1]) for i in r
    ange(3)], axis=0) #- B_z * Mz
85.     spinorb = [[0, -1j*lam[a], 0, 0, 0, lam[a]], [1j*lam[a], 0, 0, 0, 0, -
    1j*lam[a]], [0, 0, 0, -lam[a], 1j*lam[a], 0], [0, 0, -
    lam[a], 0, 1j*lam[a], 0], [0, 0, -1j*lam[a], -
    1j*lam[a], 0, 0], [lam[a], 1j*lam[a], 0, 0, 0, 0]]
```

```
86.     #os = os + 1j * lam[a] * np.sum([np.kron(eijk[:, :, i], sigma[i + 1]) for i in r
    ange(3)], axis=0) #- B_z * Mz #new
87.     x, y, z = site.pos
88.     os = os + spinorb + np.eye(6)*ef*np.dot(site.tag,[1, 1, 1])#- B_z * Mz#-
     B_z * Mz #new #added B_z Zeeman!]
89.     return os
90.
91. def hopping(site1, site2, B_z):
92.     # which sublattice
93.     a = np.sum(site1.tag) % 2
94.     b = np.sum(site2.tag) % 2
95.     d = np.array(site1.tag - site2.tag)
96.     d = d / np.sqrt(d @ d)
97.     dtd = np.outer(d, d)
98.     #dtd = np.kron(dtd, np.eye(2))
99.     dtd = np.kron(np.eye(2),dtd) #new
100.     hop = t[a, b] * dtd
101.     # print(hop)
102.     return hop
103.
104.# Populate the builder using the cubic lattice sites
105.# Use different on-sites for the two sublattices
106.syst[lat(0, 0, 0)] = onsite
107.syst[lat(0, 0, 1)] = onsite
108.
109.# Use different hoppings depending on the type
110.syst[lat.neighbors(1)] = hopping
111.syst[lat.neighbors(2)] = hopping
112.
113.## Peierls and s-wave superconductivity (BdG) ##Defineer de richtingen juist!
114.
115.def apply_peierls_to_template(template, xyz_offset=(0, 0, 0)):
116.     """Adds p.orbital argument to the hopping functions."""
117.     x0, y0, z0 = xyz_offset
118.     # hack to extract lattice constant
119.     a = 0.63*np.max(list(syst.sites())[0].family.prim_vecs) # lattice constant [nm]

120.
121.     def phase(site1, site2, B_x, B_y, B_z, e, hbar):
122.         x,y,z = site1.pos
123.         direction = site1.tag - site2.tag
124.         A = [B_y * (z - z0) - B_z * (y - y0), 0, B_x * (y - y0)]
125.         A = np.dot(A, direction) * a**2 * 1e-18 * e / hbar
126.         #if -25<x<25:
127.         if (np.dot(site1.tag, [1,-1,0])) < 0.0:
128.             phase = np.exp(-1j * A)
129.         else:
130.             phase =1
131.         return phase
132.
133.     for (site1, site2), hop in template.hopping_value_pairs():
134.         template[site1, site2] = combine(hop, phase, operator.mul, 2)
135.     return template
136.
137.#tr = la.block_diag(np.kron(2 * S[1], np.eye(1)), np.kron(2 * S[1], np.eye(3)), np.
    kron(2 * S[1], np.eye(5)))
138.tr = la.block_diag(np.kron(2 * S[1], np.eye(3)))
139.#tr = la.block_diag(np.kron(np.eye(3),2 * S[1])) #Why not the one above, like in th
    e 18-orb model? => Conseq. for B?
140.
141.def add_sc_to_template(template, tr, pairing=None):
142.     """Adds onsite s-wave superconductivity to template"""
143.     sc_template = kwant.Builder(symmetry=template.symmetry)  # Needed because kwant
    .Builder is mutable
144.     lat = list(template.sites())[0].family
145.
```

```
146.     if pairing is None:
147.         # Use the same diagonal pairing for every orbital by default
148.         pairing = np.eye(6)
149. 
150.     def paired_os(os, delta_f):
151.         pairing_mat = np.kron([[0, 1], [0, 0]], delta_f * pairing)
152.         pairing_mat += pairing_mat.conj().T
153.         os_mat = la.block_diag(os, -tr @ os.conj() @ la.inv(tr))
154.         return os_mat + pairing_mat
155. 
156.     def delta_f(site, delta):
157.         if (np.dot(site.tag, [0,1,0]))<0.0:
158.             return delta
159.#          elif -0 < (np.dot(site.tag, [1,-1,0]))<20:
160.#              return 0
161.         else:
162.             return -delta #delta!
163.     for site, os in template.site_value_pairs():
164. 
165.         sc_template[site] = combine(os, delta_f, paired_os, 1)
166.     for (site1, site2), hop in template.hopping_value_pairs():
167.         sc_template[site1, site2] = combine(hop, lambda site1, site2: 0, paired_os,
     2)
168.     return sc_template
169. 
170.syst_B = apply_peierls_to_template(syst)
171.syst_sc = add_sc_to_template(syst_B, tr)
172. 
173.%%px --local
174.film3 = kwant.Builder() #kwant.lattice.TranslationalSymmetry([0,0,2]))
175.def shape(site):
176.     return (-25.5 < (np.dot(site.tag, [1,0,0])) < 25.5 and -
    1.5 < (np.dot(site.tag, [0, 0, 1])) < 1.5 and -
    25.5 < (np.dot(site.tag, [0,1,0])) < 25.5)
177.film3.fill(syst_sc, shape, start=np.zeros(3));
178.wrapped3 = film3
179.sysf = wrapped3.finalized()
180. 
181.%%px --local
182.# %%px --local
183.##Calculate eigenvalues and eigenvectors
184.B_x = 0.0 #200 #1.0
185.B_y = 0.0 #200 #1.0
186.B_z = 0.0 #200 #1.0
187. 
188.class LuInv(sla.LinearOperator):
189.     def __init__(self, A):
190.         inst = mumps.MUMPSContext()
191.         inst.analyze(A, ordering='pord')
192.         inst.factor(A)
193.         self.solve = inst.solve
194.         sla.LinearOperator.__init__(self, A.dtype, A.shape)
195. 
196.     def _matvec(self, x):
197.         return self.solve(x.astype(self.dtype))
198. 
199.def matrix(k, Bx, By, Bz):
200.     #params = {'k_x': 0, 'B_x': B_x, 'B_y': B_y, 'B_z': B_z, 'p':None, 'hbar': 1.05
    4571800*10**-34, 'e':1.6021766208*10**-19, 'delta': 0.0025}
201.     params = {'ef':0*0.005,'k_x': k, 'B_x': Bx, 'B_y': By, 'B_z': Bz, 'p':None, 'hb
    ar': 1.054571800*10**-34, 'e':1.6021766208*10**-19, 'delta': 0.02}
202.     return sysf.hamiltonian_submatrix(params=params, sparse=True)
203. 
204.def y2(kx, sigma=0, Bx=0, By=0, Bz=0):
205.     #try:
206.     mat = matrix(kx, Bx, By, Bz)
```

```
207.     opinv = LuInv(mat - sigma * identity(mat.shape[0]))
208.     E = sla.eigsh(mat, k=80, sigma=sigma, return_eigenvectors=True, OPinv=opinv)
209.     gc.collect()
210.     #except:
211.#         E = None
212.#         gc.collect()
213.     return E
214.
215.x=[0]
216.y2 = lview.map_async(lambda x : y2(x),x)
217.y2=y2
218.y2.wait_interactive()
219.y2 = y2.get() #580;7 760;43
220.
221.plt.figure()
222.x=np.zeros(len(y2[0][0]))
223.plt.scatter(x,y2[0][0],s=5)
224.plt.show()
```

References Chapter 6

1. C. Groth, M. Wimmer, A. Akhmerov, X. Waintal, 'Kwant: a software package for quantum transport', *New Journal of Physics*, Vol. 16, (2014).
2. M. Wimmer, 'Quantum transport in nanostructures: From computational concepts to spintronics in graphene and magnetic tunnel junction', *Dissertationsreihe der Fakultät Physik der Universität Regensburg* 5, Phd, Universität Regensburg, (2009).
3. S. Datta, 'Electronic Transport in Mesoscopic Systems', *Cam. Un. Press,* (1995).
4. http://www.umich.edu/~chem461/QMChap7.pdf
5. https://quantummechanics.ucsd.edu/ph130a/130_notes/node273.html#derive:L1op